

國立臺灣大學理學院物理學系

博士論文

Department of Physics

College of Science

National Taiwan University


Doctoral Dissertation

半導體奈米結構之研究與應用：

氧化鋅、三族氮化物、以及其奈米複合材料

Studies and Applications of Semiconductor Nanostructures:

ZnO, III-nitrides, and Their Nanocomposites



施函宇

Han-Yu Shih

指導教授：陳永芳 博士

Advisor: Yang-Fang Chen, Ph.D.

中華民國 101 年 7 月

July 2012

國立臺灣大學博士學位論文
口試委員會審定書

半導體奈米結構之研究與應用：
氧化鋅、三族氮化物、以及其奈米複合材料

Studies and Applications of Semiconductor Nanostructures:
ZnO, III-nitrides, and Their Nanocomposites

本論文係施函宇君 (D97222022) 在國立臺灣大學物理學系完成之博士學位論文，於民國 101 年 7 月 10 日承下列考試委員審查通過及口試及格，特此證明

口試委員：

施函宇

(指導教授)

施函宇

梁啟澤

黃鶯聲

林春源

沈志毅

林春源

致謝

在此我要感謝這四年來協助與鼓勵我完成此論文的人，尤其是陳永芳教授、林泰源教授、我的賢妻和所有家人、當然還有我們實驗室可愛的朋友們。

Acknowledgements

Here, I would like to thank the people who have helped and encouraged me to complete this dissertation, especially Prof. Yang-Fang Chen, Prof. Tai-Yuan Lin, my whole family including my dear wife, and all lovely friends in our laboratory.



摘要

本論文主要目的在於探討氧化鋅奈米結構、氮化銦鎵/氮化鎵多重量子井，以及其複合物之新奇物理特性，並發掘這些新奇特性的可能應用。我們所獲得的成果不論是在學術上或是工業上均有極大的應用潛力，今將主要成果摘要如下：

1. 藉由第二束低於能隙的光來調變氧化鋅一維奈米結構的光激螢光和光導電性

氧化鋅奈米柱和奈米絲帶的光激螢光和光導電性是可以藉由另一道低於能隙的光束來調變的。我們將第二道光束照射在氧化鋅奈米柱和奈米絲帶時，本來被第一道紫外線雷射激發的螢光和導電性都減弱了，而且我們藉由實驗來排除熱效應的可能性。當第二道光的波長為 520 nm 時，削弱效應最明顯，這個波長剛好對應到氧化鋅內兩個氧缺陷能階之間的躍遷。藉由不同直徑的奈米柱來重複以上實驗，我們驗證了缺陷存在於表面區域。藉由改變第二道光的強度來重複以上實驗，更支持了我們所提出來的機制。

2. 氮化銦鎵/氮化鎵多層量子碟受到外應力引發的對稱光學特性

我們研究了外力對氮化銦鎵/氮化鎵多層量子碟光學特性的影響。因壓電效應和量子侷限史塔克效應，當一股橫向應力施加在多層量子碟時，光激螢光和拉曼散射光譜都被改變了。有趣的是，光譜改變的行為呈現六角形對稱。這詭譎的現象可被歸因為晶格本身存在著六角形對稱，而且彈性薄膜又沿著某些特定的方向來

拉扯樣品的晶格。此實驗成果可以提供另外一種面向來推廣與應用氮化物半導體所構成的光電元件並使其效能最佳化。

3. 氧化鋅奈米柱和氮化銦鎵/氮化鎵多層量子井構成可調變顏色的發光元件

我們將氧化鋅奈米柱成長在氮化銦鎵/氮化鎵多層量子上，我們建構了一種可發射兩種波長的新穎發光元件。有趣的是，這兩種發射光譜可以藉由偏振的選擇性來調變它們的相對強度。其背後的機制可歸因於這兩種奈米結構的幾何形狀恰好呈現互相垂直的方向。此實驗成果可以拓展到其他具有類似結構的複合材料，並且替可調變式發光元件開闢一個新的研究方向。

4. 藉由酵素修飾氧化鋅奈米柱和氮化銦鎵/氮化鎵多層量子井的光學特性來偵

測葡萄糖

因奈米柱的表面積對體積比例很高，且氮化物壓電材料對電場很敏感，我們採用酵素修飾過的奈米柱與氮化物發光元件構成的複合材料來偵測葡萄糖分子。比起傳統必須監控電流的感測器，我們卻選擇監控發光元件的光譜，使測量和製程更加簡單。氧化鋅奈米柱和氮化銦鎵/氮化鎵多層量子井建構而成的感測元件暴露在葡萄糖溶液後，其光激螢光和拉曼散射光譜即產生顯著的變化。此實驗成果提供了一種新穎且高敏感度的光學式感測元件。

5. 藉由鉑粒子修飾氧化鋅奈米柱和氮化銦鎵/氮化鎵多層量子井的光學特性來

偵測氫氣

延續前一個研究工作，我們採用包含鉑粒子修飾過的奈米柱與氮化物發光元件構成的複合材料來偵測氫氣分子。比起傳統必須監控電流的感測器，我們卻選擇監控發光元件的光譜，使測量和製程更加簡單。氧化鋅奈米柱和氮化銦鎵/氮化鎵多層量子井建構而成的感測元件暴露在葡萄糖溶液後，其光激螢光和拉曼散射光譜即產生顯著的變化。此元件的結構可推廣應用於感測其他種類的化學或生物分子。

關鍵字：半導體、奈米科技、氧化鋅、三族氮化物



Abstract

In this dissertation, we mainly focus on the study of the physical properties of ZnO nanostructures, InGaN/GaN multiple quantum wells, and their composites. Based on the discovered novel properties, we attempt to develop their potential applications. A brief description of our main findings has been summarized as follows. It is believed that our results shown here should be very useful for the general interests both in academics as well as industry

1. Tunable Photoluminescence and Photoconductivity in ZnO One-dimensional Nanostructures with a Second Below-gap Beam

Tunable photoluminescence (PL) and photoconductivity (PC) with a second below-gap beam were demonstrated on ZnO nanorods and nanoribbons. We found that both PL and PC could be quenched as the second beam was applied on the nanostructures, and this behavior was excluded from thermal effect by comparing the phonon replica spectra with that of heating the sample directly. The most quenching effect occurred near the defect transition locating at 520 nm. The underlying mechanism of the quenching behavior was attributed to the defect transition between different states of oxygen vacancies. Size-dependence measurement lets us know the effect occurs near the surface of nanostructures, and the power-dependent measurement further confirms the underlying mechanism we proposed.

2. Symmetrically Tunable Optical Properties of InGaN/GaN Multiple Quantum Disks by an External Stress

The influence of an external stress on the optical properties of InGaN/GaN multiple quantum disks (MQDs) has been investigated. As a transversal force is applied on the MQDs, both photoluminescence and Raman scattering spectra are altered due to the piezoelectric potential accompanied by the quantum confined Stark effect. Quite interestingly, it is found that the optical spectra possess a sixfold symmetry about the *c*-axis. This intriguing phenomenon can be attributed to the inherent nature of hexagonal lattice as well as the good flexibility of the composite consisting of polydimethylsiloxane and MQDs. Our results can provide an alternative route to optimize and extend the application of nitride-based devices.

3. Light-emitting Devices with Tunable Color from ZnO Nanorods Grown on InGaN/GaN Multiple Quantum Wells

Based on the composite consisting of ZnO nanorods (NRs) grown on InGaN/GaN multiple quantum wells (MQWs), we have demonstrated a novel light-emitting device (LED) that has the capability to emit dual beam radiations. Interestingly, the relative intensity between the dual emissions is able to be manipulated by their polarizations. The underlying mechanism can be well understood in terms of the anisotropic optical properties arising from the geometric structures of constituent nanoscale materials.

The results shown here may be extended to many other nanocomposite systems and pave a new pathway to create LEDs with tunable properties.

4. Optical Detection of Glucose Based on the Composite Consisting of Enzymatic ZnO Nanorods and InGaN/GaN Multiple Quantum Wells

Based upon the high surface-to-volume ratio of nanorods and high sensitivity of piezoelectric properties of nitride semiconductors, enzymatic functionalized composite consisting of nanorods and nitride light emitting devices (LEDs) provide an excellent opportunity for the development of glucose detectors using optical methods. To demonstrate our working principle, a sensing device based on InGaN/GaN multiple quantum wells and ZnO nanorods has been constructed and exposed to target glucose solutions. The pronounced changes of emission as well as Raman scattering spectra under different target glucose concentrations clearly illustrate the feasibility of our newly designed composite for the creation of highly sensitive biosensors with optical detection.

5. Optical Detection of Hydrogen Gas Using Pt-catalyzed ZnO Nanorods and InGaN/GaN Multiple Quantum Wells

Based upon the high surface-to-volume ratio of nanorods and high sensitivity of piezoelectric properties of nitride semiconductors, catalyst decorated composite consisting of nanorods and nitride light-emitting devices (LEDs) provide an excellent

opportunity for the development of gas detectors using optical methods. To demonstrate our working principle, a sensing device based on the composite consisting of InGaN/GaN multiple quantum wells (MQWs) and Pt-catalyzed ZnO nanorods has been fabricated and exposed to target hydrogen gas. The pronounced changes of emission as well as Raman scattering spectra of InGaN/GaN MQWs under different target gas concentrations clearly illustrate the feasibility of our newly designed composites for the creation of highly sensitive gas sensors with optical detection.

Keywords: semiconductor, nanotechnology, ZnO, III-nitrides.



Contents

致謝 (Acknowledgements).....	I
摘要.....	III
Abstract.....	VI
Contents.....	X
Figure Captions.....	XII
Publications in Recent Five Years.....	XVII
Chapter 1 Introduction to this Dissertation.....	1
Chapter 2 Background Knowledge.....	7
2.1 Techniques of Measurements.....	7
2.1.1 Spectroscope (Spectrometer).....	7
2.1.2 Photoluminescence.....	14
2.1.3 Raman Scattering.....	20
2.1.4 X-ray Diffraction.....	26
2.1.5 Scanning Electron Microscope.....	28
2.2 Growth Methods.....	35
2.2.1 Metal-organic Chemical Vapor Deposition...	35
2.2.2 Vapor-Liquid-Solid Growth.....	38
2.2.3 Hydrothermal Growth of ZnO Nanorods.....	40
2.2.4 DC Sputtering Deposition.....	40
2.3 Physics of Materials.....	42
2.3.1 Piezoelectricity.....	42
2.3.2 Quantum Confined Stark Effect.....	44
2.3.3 Zinc Oxide.....	45
2.3.4 III-nitride Semiconductors.....	48
2.3.5 Light-emitting Diodes.....	51
Chapter 3 Tunable Photoluminescence and Photoconductivity in ZnO One-dimensional Nanostructures with a Second Below-gap Beam.....	57
3.1 Introduction.....	57
3.2 Experiment.....	58

	3.3 Results and Discussion.....	59
	3.4 Conclusion.....	70
Chapter 4	Symmetrically Tunable Optical Properties of InGaN/GaN Multiple Quantum Disks by an External Stress.....	73
	3.1 Introduction.....	73
	3.2 Experiment.....	74
	3.3 Results and Discussion.....	77
	3.4 Conclusion.....	84
Chapter 5	Light-emitting Devices with Tunable Color from ZnO Nanorods Grown on InGaN/GaN Multiple Quantum Wells	87
	3.1 Introduction.....	87
	3.2 Experiment.....	89
	3.3 Results and Discussion.....	92
	3.4 Conclusion.....	100
Chapter 6	Optical Detection of Glucose Based on the Composite Consisting of Enzymatic ZnO Nanorods and InGaN/GaN Multiple Quantum Wells.....	105
	3.1 Introduction.....	105
	3.2 Experiment.....	107
	3.3 Results and Discussion.....	109
	3.4 Conclusion.....	117
Chapter 7	Optical Detection of Hydrogen Gas Using Pt-catalyzed ZnO Nanorods and InGaN/GaN Multiple Quantum Wells..	121
	3.1 Introduction.....	121
	3.2 Experiment.....	123
	3.3 Results and Discussion.....	126
	3.4 Conclusion.....	133
Chapter 8	Summary of this Dissertation.....	137

Figure Captions

- Fig. 2.1** Diagram of a Czerny-Turner monochromator. **8**
- Fig. 2.2** Schematic of a photomultiplier tube coupled to a scintillator. **11**
- Fig. 2.3** A charge-coupled device from a 2.1 megapixel digital camera **13**
- Fig. 2.4** Energy transitions in (a) direct and (b) indirect gap semiconductors between initial states E_i and final states E_f . For indirect transitions (b) the participation of a phonon (E_{ph}) is required. **16**
- Fig. 2.5** Schematic diagram of radiative transitions between the conduction band (E_C), the valence band (E_V) and exciton (E_X), donor (E_D) and acceptor (E_A) levels in a semiconductor. **17**
- Fig. 2.6** This spectrum showing the photoluminescence peak and the Raman phonon mode of a CdMnTe film on a GaAs substrate (Perkowitz, 1991). **21**
- Fig. 2.7** The diagram shows the conservation rules in the Raman scattering. **22**
- Fig. 2.8** The Raman spectrum of CCl_4 . **22**
- Fig. 2.9** A simplified Raman spectroscopy experiment setup with a charge-coupled device (CCD) as the detector. **24**
- Fig. 2.10** The structural scheme of a typical scanning electron microscope. **30**
- Fig. 2.11** Summary of the range and spatial resolution of backscattered electrons, secondary electrons, X-rays, and Auger electrons for electrons incident on a solid. **33**
- Fig. 2.12** A schematic illustration in metal-organic chemistry vapor deposition. **35**

Fig. 2.13	A schematic illustration of the apparatus of metal-organic chemistry vapor deposition.	36
Fig. 2.14	The illustration of vapor-liquid-solid growth process.	39
Fig. 2.15	A schematic illustration of the apparatus of DC sputtering deposition.	41
Fig. 2.16	An illustration of the piezoelectricity concept.	43
Fig. 2.17	Illustration diagram of the band structure of MQWs (a) without and (b) with external electric field.	44
Fig. 3.1	Scanning electron microscopy images of ZnO nanorods with different diameters of (a) 300~350 nm, (b) 150~250 nm, and (c) 70~100 nm. The image of ZnO nanoribbons is shown in (d). One can notice the scale bars in (a) and (b) to tell the sizes of nanorods.	60
Fig. 3.2	(a) Photoluminescence spectra of thin ZnO nanorods with a 325 nm UV pumping source while the below-gap source with 532 nm keeps on/off at 12K. The inset shows the time evolution of band-edge emission as the second beam (532 nm) was switched on and off. (b) Comparison of the optical quenching and thermal quenching. (c) Spectral distribution of excitation and quenching of band-edge emission from ZnO nanorods at 12K. The inset shows the dependence between the R_w ratio and the diameter of ZnO nanorods.	61
Fig. 3.3	(a) Scheme of the device profile to illustrate the experimental process of the quenching effect in ZnO nanoribbons. (b) Spectral distribution of excitation and quenching of the photocurrent in ZnO nanoribbons at 12K. The dashed line shows the constant current excited by 325 nm laser. The inset shows the	65

time evolution of photocurrent as the second beam (532 nm) was switched on and off.

Fig. 3.4 (a) Illustration to the carrier transitions which can explain the quenching effect of the NBE emission by the below-gap illumination. (b) Quenching ratios as a function of below-gap excitation power density in three different sizes. **68**

Fig. 4.1 (a) Side view of the etched nanorods recorded by the scanning electron microscope (SEM). (b) Illustration of the details of the optical measurements. **76**

Fig. 4.2 (a) Photoluminescence (PL) spectra of the multiple quantum disks with different external force applied by the tunable linear stage (TLS). (b) Peak position of the PL spectra with different external force applied by the TLS. (c) Illustration of the piezoelectric potential and the electronic band structure in the nanorods. (d) The red-shift amount of the photoluminescence spectra as a function of the cutting angle of the sample. **78**

Fig. 4.3 (a) Raman scattering spectra of the multiple quantum disks with different external force applied by the tunable linear stage (TLS). (b) Full width at half maximum of the Raman scattering spectra as a function of the external force applied by the TLS. (c) The low-frequency-shift amount of the Raman scattering spectra as a function of the cutting angle of the sample. **82**

Fig. 5.1 (a) Top view and (b) side view of scanning electron microscope images of InGaN/GaN/ZnO nanocomposite material. (c) X-ray diffraction spectrum and (d) x-ray diffraction spectrum with enlarged scale of 33.6-36.0 degree in (c). **91**

- Fig. 5.2** (a) Illustration of experimental details of electroluminescence measurements for the composited light-emitting device. (b) The current through the light-emitting device as a function of bias voltage. (c) Current dependence of electroluminescence spectra of the composited light-emitting device. (d) Intensities of the 380 nm and 440 nm emissions as functions of the injection current. **93**
- Fig. 5.3** Band structure of the composited light-emitting device under forward bias. **95**
- Fig. 5.4** (a) Electroluminescence (EL) spectra from the composited light-emitting device through a rotatable polarizer with the angle of 0° and 90° . (b) Polarizer-angle-dependent EL intensities with the monochromator fixed at 380 nm and (c) 440 nm, respectively. Malus's-law-fitted lines of 380 nm and 440 nm emissions by equation (2) are also shown in (b) and (c). **97**
- Fig. 5.5** Illustrations of the experimental details and measured spectra under different polarization for (a) InGaN/GaN quantum wells and (b) ZnO nanorods. **99**
- Fig. 6.1** Photoluminescence spectra of InGaN/GaN multiple quantum wells (MQWs) under different excitation power densities. **108**
- Fig. 6.2** (a) Top view and (b) side view of scanning electron microscope images ZnO nanorods grown on the top surface of InGaN/GaN multiple quantum wells. (c) The schematic diagram of the glucose sensing device. Both excitation and emission are taken at the edge side of the device. **110**
- Fig. 6.3** Photoluminescence spectra of InGaN/GaN multiple quantum wells (a) with and (b) without enzymatic ZnO nanorods with increasing target glucose concentration. (c) Illustration diagram of the reduction-oxidation reaction **111**

between glucose oxidase and glucose molecules occurring on the surfaces of nanorods.

- Fig. 6.4** Illustration diagram of the band structure of MQWs (a) without and (b) with external electric field. **113**
- Fig. 6.5** Raman spectra of InGaN/GaN multiple quantum wells (a) with and (b) without enzymatic ZnO nanorods with increasing target glucose concentration. (c) Estimated lattice strain of InGaN/GaN multiple quantum wells as a function of the target glucose concentration via Eq. (6.1). **115**
- Fig. 7.1** (a) Top view and (b) side view of scanning electron microscope images of ZnO nanorods grown on sapphire substrate. **125**
- Fig. 7.2** (a) Photoluminescence spectra of InGaN/GaN multiple quantum wells with Pt-catalyzed ZnO nanorods, (b) uncatalyzed ZnO nanorods, and (c) without ZnO nanorods as under the increasing concentration of target hydrogen gas. (d) Peak positions of the spectra in (a), (b), and (c) as functions of the concentration of target hydrogen gas. **127**
- Fig. 7.3** Illustration diagram of the band structure of MQWs (a) without and (b) with external electric field. **129**
- Fig. 7.4** (a) Raman scattering spectra of InGaN/GaN multiple quantum wells with Pt-catalyzed ZnO nanorods, (b) uncatalyzed ZnO nanorods, and (c) without ZnO nanorods as under the increasing concentration of target hydrogen gas. (d) Estimated lattice strain of InGaN/GaN multiple quantum wells as functions of the concentration of target hydrogen gas. **131**

Publications in Recent Five Years

Journal Papers

1. H. Y. Shih, T. T. Chen, C. H. Wang, K. Y. Chen, and Y. F. Chen, “Optical detection of deoxyribonucleic acid hybridization with InGaN/GaN multiple quantum wells” Appl. Phys. Lett. **92**, 261910 (2008).
2. H. Y. Shih, T. T. Chen, Y. C. Chen, T. H. Lin, L. W. Chang, and Y. F. Chen, “Size-dependent photoelastic effect in ZnO nanorods” Appl. Phys. Lett. **94**, 021908 (2009).
3. Tzung-Hsuan Lin, Chung-Liang Cheng, Han-Yu Shih, and Yang-Fang Chen, “Optical enhancement in nanoparticle-decorated ZnO nanorods” J. Appl. Phys. **105**, 083541 (2009).
4. Yu-Lun Chiang, Chih-Wei Chen, Chun-Hsiung Wang, Chun-Yi Hsieh, Yung-Ting Chen, Han-Yu Shih, and Yang-Fang Chen, “Mechanically tunable surface plasmon resonance based on gold nanoparticles and elastic membrane polydimethylsiloxane composite” Appl. Phys. Lett. **96**, 041904 (2010).
5. Yungting Chen, Hanyu Shih, Chunhsiung Wang, Chunyi Hsieh, Chihwei Chen, Yangfang Chen, and Taiyuan Lin, “Ultraviolet electroluminescence from hybrid inorganic/organic ZnO/GaN/poly(3-hexylthiophene) dual heterojunctions” Optics Express **19**, A319 (2011).
6. H. Y. Shih, Y. T. Chen, N. H. Huang, C. M. Wei, and Y. F. Chen, “Tunable photoluminescence and photoconductivity in ZnO one-dimensional nanostructures with a second below-gap beam” J. Appl. Phys. **109**, 103523 (2011).
7. Han-Yu Shih, Yung-Ting Chen, Chih-Ming Wei, Ming-Hui Chan, Jyong-Kuen Lian, Yang-Fang Chen, and Tai-Yuan Lin, “Optical Detection of Glucose Based

on a Composite Consisting of Enzymatic ZnO Nanorods and InGaN/GaN Multiple Quantum Wells” J. Phys. Chem. C **115**, 14664 (2011).

8. C. M. Wei, H. Y. Shih, Y. F. Chen, and T. Y. Lin, “Optical detection of magnetoelectric effect in the composite consisting of InGaN/GaN multiple quantum wells and FeCo thin film” Appl. Phys. Lett. **98**, 131913 (2011).
9. Han-Yu Shih, Shih-Hao Cheng, Jyong-Kuen Lian, Tai-Yuan Lin, and Yang-Fang Chen, “Light-emitting devices with tunable color from ZnO nanorods grown on InGaN/GaN multiple quantum wells” Optics Express **20**, A270 (2012).
10. H. Y. Shih, Y. F. Chen, and T. Y. Lin, “Symmetrically tunable optical properties of InGaN/GaN multiple quantum disks by an external stress” Appl. Phys. Lett. **100**, 171916 (2012).
11. T. P. Chen, H. Y. Shih, J. T. Lian, J. H. Chen, P. S. Lin, T. Y. Lin, J. R. Gong, and Y. F. Chen, “Electro-colorimetric hydrogen gas sensor based on Pt-functionalized In₂O₃ nanopushpins and InGaN/GaN multiple quantum wells” Optics Express **20**, 17136 (2012).

Conference Papers

1. Han Yu Shih and Yang Fang Chen, “Size-dependent photoelastic effect in ZnO nanorods” Oral presentation, APS March Meeting **55**, 2 (2010).
2. Tzung-Te Chen, Han-Kuei Fu, Chien-Ping Wang, Shih-Chun Yang, An-Tse Lee, Sheng-Bang Huang, Mu-Tao Chu, Han-Yu Shih, and Yang-Fang Chen, “Enhanced Electroluminescence and efficiency droop behavior of direct current aged InGaN-based light-emitting diodes” Poster, APS March Meeting **55**, 2 (2010).

Chapter 1

Introduction to this Dissertation

Let us start with semiconductors. Semiconductors have electrical conductivity intermediate in magnitude between that of a conductor and an insulator. This means a conductivity roughly in the range of 10^{-2} to 10^4 siemens (the unit of electric conductance and electric admittance) per centimeter. Semiconductor materials are the foundation of modern electronic devices, including radio, computers, telephones, and many other devices. Such devices include transistors, solar cells, many kinds of diodes including the light-emitting diode (LED), the silicon controlled rectifier, photo-diode, and digital and analog integrated circuits. Although silicon (Si) is used to create most semiconductors commercially, dozens of other materials are used, including germanium (Ge), silicon carbide (SiC), II-VI compounds, and III-V compounds. A pure semiconductor is often called an “intrinsic” semiconductor. The electronic properties and the conductivity of a semiconductor can be changed in a controlled manner by adding very small quantities of other elements, called “dopants”, to the intrinsic material. In crystalline silicon typically this is achieved by adding impurities of boron or phosphorus to the melt and then allowing it to solidify into the crystal. This process is called "doping" and the semiconductor is "extrinsic".¹

When materials are scaled into a small size, around decades of nanometers, some

quantum effects will reveal and many physical properties will be quite unique compared with those in bulk form. Therefore, the concept of “nanotechnology” is popularized in the 1980’s to talk about the applications of these nanostructures of materials. Nanotechnology (sometimes shortened to "nanotech") is the study of manipulating matter on an atomic and molecular scale. Generally, nanotechnology deals with developing materials, devices, or other structures with at least one dimension sized from 1 to 100 nanometers. By comparison, typical carbon-carbon bond lengths, or the spacing between these atoms in a molecule, are in the range 0.12–0.15 nm, and a DNA double-helix has a diameter around 2 nm. On the other hand, the smallest cellular life-forms, the bacteria of the genus *Mycoplasma*, are around 200 nm in length. Quantum mechanical effects are important at this quantum-realm scale. Nanotechnology is considered a key technology for the future. Nanotechnology is very diverse, ranging from extensions of conventional device physics to completely new approaches based upon molecular self-assembly, from developing new materials with dimensions on the nanoscale to direct control of matter on the atomic scale. Nanotechnology entails the application of fields of science as diverse as surface science, organic chemistry, molecular biology, semiconductor physics, microfabrication, etc.

In its original sense, nanotechnology refers to the projected ability to construct

items from the bottom up, using techniques and tools being developed today to make complete, high performance products. By convention, nanotechnology is taken as the scale ranging from 1 to 100 nm, which follows the definition used by the National Nanotechnology Initiative in the US. The lower limit is set by the size of atoms (hydrogen has the smallest atoms, which are approximately a quarter of a nm diameter) since nanotechnology must build its devices from atoms and molecules. The upper limit is more or less arbitrary but is around the size that phenomena not observed in larger structures start to become apparent and can be made use of in the nano device.² These new phenomena make nanotechnology distinct from devices which are merely miniaturised versions of an equivalent macroscopic device; such devices are on a larger scale and come under the description of microtechnology.³

To put that scale in another context, the comparative size of a nanometer to a meter is the same as that of a marble to the size of the earth. Or another way of putting it: a nanometer is the amount an average man's beard grows in the time it takes him to raise the razor to his face.⁴ Two main approaches are used in nanotechnology. In the "bottom-up" approach, materials and devices are built from molecular components which assemble themselves chemically by principles of molecular recognition. In the "top-down" approach, nano-objects are constructed from larger entities without atomic-level control.⁵ Nanotechnology may be able to create many new materials and

devices with a vast range of applications, such as in medicine, electronics, biomaterials and energy production. On the other hand, nanotechnology raises many of the same issues as any new technology, including concerns about the toxicity and environmental impact of nanomaterials,⁶ and their potential effects on global economics, as well as speculation about various doomsday scenarios. These concerns have led to a debate among advocacy groups and governments on whether special regulation of nanotechnology is warranted.

In this dissertation, we emphasized the investigations on the physical properties and applications of II-VI and III-V compounds, especially ZnO and III-nitrides. These two materials are quite attractive and popular for the people who study in the field of optoelectronics. They are usually fabricated into light-emitting diodes (LEDs), laser diodes (LDs), solar cells, gas sensors, biosensors, and so on. In chapter 2, we introduced the necessary background knowledge for our works, including techniques of measurements, growth methods, and physical concepts of our samples. Then, the next 5 chapters describe the main works of this dissertation. Chapters 3 and 4 are emphasized on the basic optical and electric properties of the nanostructures of ZnO and InGaN/GaN multiple quantum wells (MQWs), respectively. In chapter 5, we presented a novel LED with tunable color consisting of ZnO nanorods (NRs) and InGaN/GaN MQWs. Chapters 6 and 7 show the demonstrations about two interesting

applications for sensing abilities for chemical molecules using the devices consisting of ZnO NRs and InGaN/GaN MQWs. Finally, we summarized the whole portion of this dissertation in chapter 8. We sincerely hope the results of our works are able to provide contributions for the modern technology and bring more advantages for our daily life.

Reference

1. Online resource, <http://goldbook.iupac.org/S05591.html>
2. Fritz Allhoff, Patrick Lin, Daniel Moore, *What is nanotechnology and why does it matter?: from science to ethics*, pp.3–5, John Wiley and Sons, 2010 ISBN 1-4051-7545-1.
3. S.K. Prasad, *Modern Concepts in Nanotechnology*, pp.31–32, Discovery Publishing House, 2008 ISBN 81-8356-296-5.
4. Kahn, Jennifer, "Nanotechnology". *National Geographic* 2006 (June): pp. 98–119.
5. P. Rodgers, "Nanoelectronics: Single file". *Nature Nanotechnology* (2006).
6. Cristina Buzea, Ivan Pacheco, and Kevin Robbie, "Nanomaterials and Nanoparticles: Sources and Toxicity". *Biointerphases* 2: MR17. (2007).



Chapter 2

Background Knowledge

2.1 Techniques of Measurements

2.1.1 Spectrometer (Spectroscope)

A spectrometer (spectroscope) is an instrument used to measure properties of light over a specific portion of the electromagnetic spectrum, typically used in spectroscopic analysis to identify materials.¹ The variable measured is most often the light's intensity but could also, for instance, be the polarization state. The independent variable is usually the wavelength of the light or a unit directly proportional to the photon energy, such as wavenumber or electron volts, which has a reciprocal relationship to wavelength. A spectrometer is used in spectroscopy for producing spectral lines and measuring their wavelengths and intensities. Spectrometer is a term that is applied to instruments that operate over a very wide range of wavelengths, from gamma rays and X-rays into the far infrared. If the instrument is designed to measure the spectrum in absolute units rather than relative units, then it is typically called a spectrophotometer. The majority of spectrophotometers are used in spectral regions near the visible spectrum. Here, we will briefly introduce the two main portions of a spectrometer: monochromator and detector.

- **Monochromator**

A monochromator can use either the phenomenon of optical dispersion in a prism, or that of diffraction using a diffraction grating, to spatially separate the colors of light. It usually has a mechanism for directing the selected color to an exit slit.²

Usually the grating or the prism is used in a reflective mode. A reflective prism is made by making a right triangle prism (typically, half of an equilateral prism) with one side mirrored. The light enters through the hypotenuse face and is reflected back through it, being refracted twice at the same surface. The total refraction, and the total dispersion, is the same as would occur if an equilateral prism were used in transmission mode.

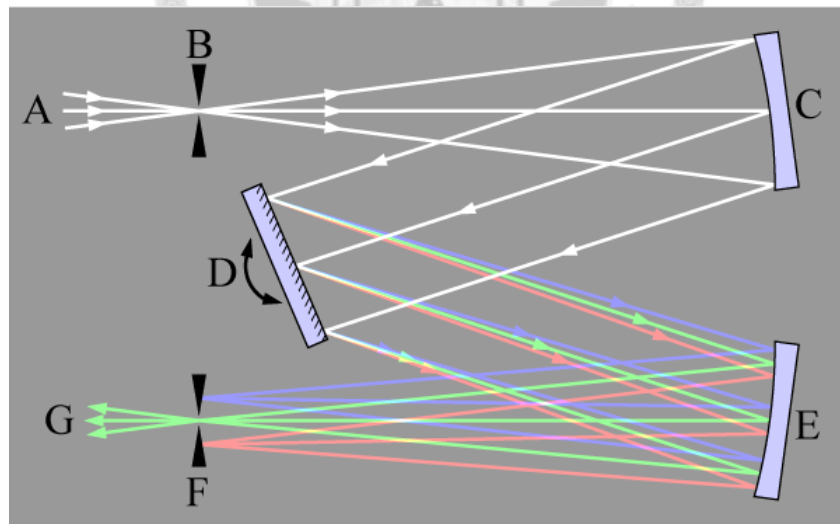


Fig. 2.1 Diagram of a Czerny-Turner monochromator.

In the common Czerny-Turner design, the broad band illumination source (A) is aimed at an entrance slit (B). The amount of light energy available for use depends on

the intensity of the source in the space defined by the slit (width * height) and the acceptance angle of the optical system. The slit is placed at the effective focus of a curved mirror (the collimator, C) so that the light from the slit reflected from the mirror is collimated (focused at infinity). The collimated light is diffracted from the grating (D) and then is collected by another mirror (E) which refocuses the light, now dispersed, on the exit slit (F). In a prism monochromator, a reflective prism takes the place of the diffraction grating, in which case the light is refracted by the prism .

At the exit slit, the colors of the light are spread out (in the visible this shows the colors of the rainbow). Because each color arrives at a separate point in the exit slit plane, there are a series of images of the entrance slit focused on the plane. Because the entrance slit is finite in width, parts of nearby images overlap. The light leaving the exit slit (G) contains the entire image of the entrance slit of the selected color plus parts of the entrance slit images of nearby colors. A rotation of the dispersing element causes the band of colors to move relative to the exit slit, so that the desired entrance slit image is centered on the exit slit. The range of colors leaving the exit slit is a function of the width of the slits. The entrance and exit slit widths are adjusted together.

A monochromator's adjustment range might cover the visible spectrum and some part of both or either of the nearby ultraviolet (UV) and infrared (IR) spectra,

although monochromators are built for a great variety of optical ranges, and to a great many designs. It is common for two monochromators to be connected in series, with their mechanical systems operating in tandem so that they both select the same color. This arrangement is not intended to improve the narrowness of the spectrum, but rather to lower the cutoff level. A double monochromator may have a cutoff about one millionth of the peak value, the product of the two cutoffs of the individual sections. The intensity of the light of other colors in the exit beam is referred to as the stray light level and is the most critical specification of a monochromator for many uses. Achieving low stray light is a large part of the art of making a practical monochromator.

When a diffraction grating is used, care must be taken in the design of broadband monochromators because the diffraction pattern has overlapping orders. Sometimes extra, broadband filters are inserted in the optical path to limit the width of the diffraction orders so they do not overlap. Sometimes this is done by using a prism as one of the monochromators of a dual monochromator design. Prisms have higher dispersion in the UV region. Prism monochromators are favored in some instruments that are principally designed to work in the far UV region. Most monochromators use gratings, however. Some monochromators have several gratings that can be selected for use in different spectral regions. A double monochromator made by placing a

prism and a grating monochromator in series typically does not need additional bandpass filters to isolate a single grating order.

- **Detector (PMT or CCD)**

Photomultiplier tubes (PMTs) are constructed from a glass envelope with a high vacuum inside, which houses a photocathode, several dynodes, and an anode.³

Incident photons strike the photocathode material, which is present as a thin deposit on the entry window of the device, with electrons being produced as a consequence of the photoelectric effect. These electrons are directed by the focusing electrode toward the electron multiplier, where electrons are multiplied by the process of secondary emission.

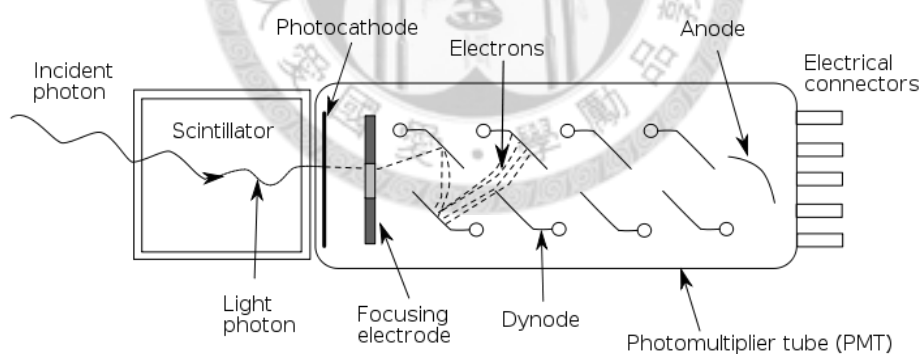


Fig. 2.2 Schematic of a photomultiplier tube coupled to a scintillator.

The electron multiplier consists of a number of electrodes called dynodes. Each dynode is held at a more positive voltage than the previous one. The electrons leave the photocathode, having the energy of the incoming photon (minus the work function

of the photocathode). As the electrons move toward the first dynode, they are accelerated by the electric field and arrive with much greater energy. Upon striking the first dynode, more low energy electrons are emitted, and these electrons in turn are accelerated toward the second dynode. The geometry of the dynode chain is such that a cascade occurs with an ever-increasing number of electrons being produced at each stage. Finally, the electrons reach the anode, where the accumulation of charge results in a sharp current pulse indicating the arrival of a photon at the photocathode.

There are two common photomultiplier orientations, the head-on or end-on (transmission mode) design, as shown in Fig. 2.2, where light enters the flat, circular top of the tube and passes the photocathode, and the side-on design (reflection mode), where light enters at a particular spot on the side of the tube, and impacts on an opaque photocathode. Besides the different photocathode materials, performance is also affected by the transmission of the window material that the light passes through, and by the arrangement of the dynodes. A large number of photomultiplier models are available having various combinations of these, and other, design variables. Either of the manuals mentioned will provide the information needed to choose an appropriate design for a particular application.

A charge-coupled device (CCD) is a device for the movement of electrical charge, usually from within the device to an area where the charge can be

manipulated, for example conversion into a digital value.⁴ This is achieved by "shifting" the signals between stages within the device one at a time. CCDs move charge between capacitive bins in the device, with the shift allowing for the transfer of charge between bins. In a CCD for capturing optical signals, there is a photoactive region (an epitaxial layer of silicon), and a transmission region made out of a shift register (the CCD, properly speaking).

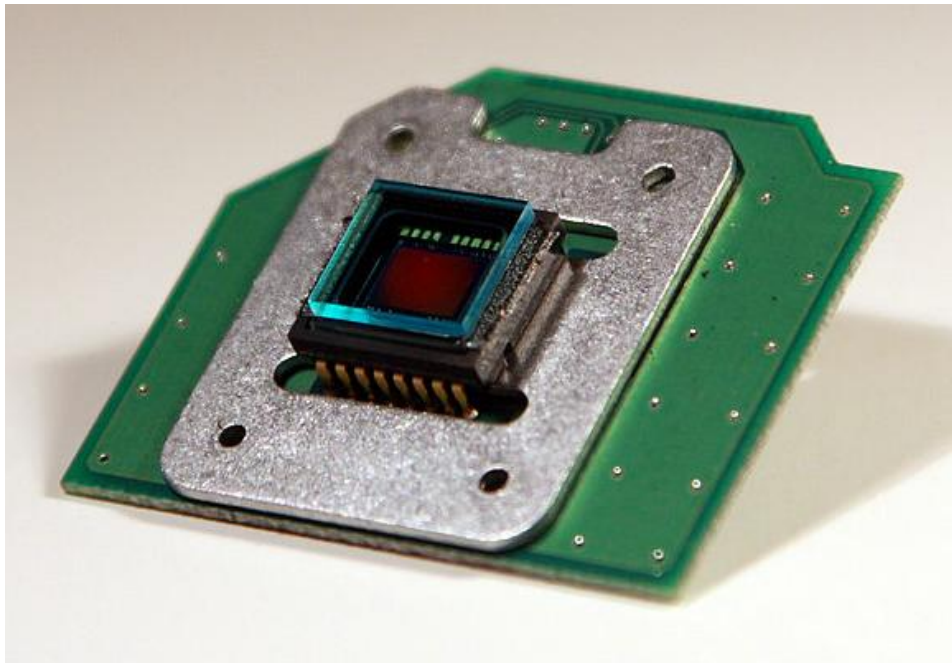


Fig. 2.3 A charge-coupled device from a 2.1 megapixel digital camera

An image is projected through a lens onto the capacitor array (the photoactive region), causing each capacitor to accumulate an electric charge proportional to the light intensity at that location. A one-dimensional array, used in line-scan cameras, captures a single slice of the image, while a two-dimensional array, used in video and

still cameras, captures a two-dimensional picture corresponding to the scene projected onto the focal plane of the sensor. Once the array has been exposed to the image, a control circuit causes each capacitor to transfer its contents to its neighbor (operating as a shift register). The last capacitor in the array dumps its charge into a charge amplifier, which converts the charge into a voltage. By repeating this process, the controlling circuit converts the entire contents of the array in the semiconductor to a sequence of voltages. In a digital device, these voltages are then sampled, digitized, and usually stored in memory; in an analog device (such as an analog video camera), they are processed into a continuous analog signal (e.g. by feeding the output of the charge amplifier into a low-pass filter) which is then processed and fed out to other circuits for transmission, recording, or other processing.

2.1.2 Photoluminescence

A light source with photon energy higher than the band gap of the semiconductor crystal will excite the carriers to their excited states. As soon as the excitation occurs, all excited electrons and holes will relax to the bottom of the conduction band and the top of valence band, respectively, and then the recombination occurs. Energy and momentum must be conserved during the electronic transitions. As shown in Fig. 2.4, when the maximum of the valence band and the conduction band occur at the same value of the wave vector \mathbf{k} , transitions are direct and the material is a direct-gap

semiconductor (for example, ZnSe, InP, and GaAs). In materials with a direct gap, the most likely transitions are across the minimum energy gap, between the most probably filled states at the minimum of the conduction band, and the states most likely to be unoccupied at the maximum of the valence band. If the band extreme do not occur at the same wave vector \mathbf{k} , transitions are indirect. To conserve momentum in such an indirect-gap material (for example, Si, and Ge), phonon participation is required. Thus, the recombination of electron-hole pairs must accompanied by the simultaneous emission of a photon and a phonon. The probability of such a process is significantly lower as compared with direct transitions. The radiative recombination that is difference to the incandescence coming from hot source is called photoluminescence (PL). If there is a multiplicity of excited states, only transitions from the lowest excited state can generally be observed at low temperature because of rapid thermalization.⁵

Photoluminescence is one of the most useful optical methods for the semiconductor industry,^{5,6} with its powerful and sensitive ability to find impurities and defect levels, which affect material's quality and device performance. A given impurity produces a set of characteristic spectral features. This fingerprint identifies the impurity type, and often several different impurities can be seen in a single PL spectrum. In some cases PL goes beyond bare identification, to measure impurity

concentrations. In another use, the half widths of PL peaks are an indication of sample quality and crystallinity, although such analysis has not yet become highly quantitative. Finally, PL is sensitive to stress, and can measure its magnitude and direction. Photoluminescence can also determine semiconductor band gaps. This is important for mixed crystals whose gap varies with the compositional parameter x , yet must accurately known for applications. When the relation between gap energy and x is known, the PL measurement of gap can be inverted to determine x .

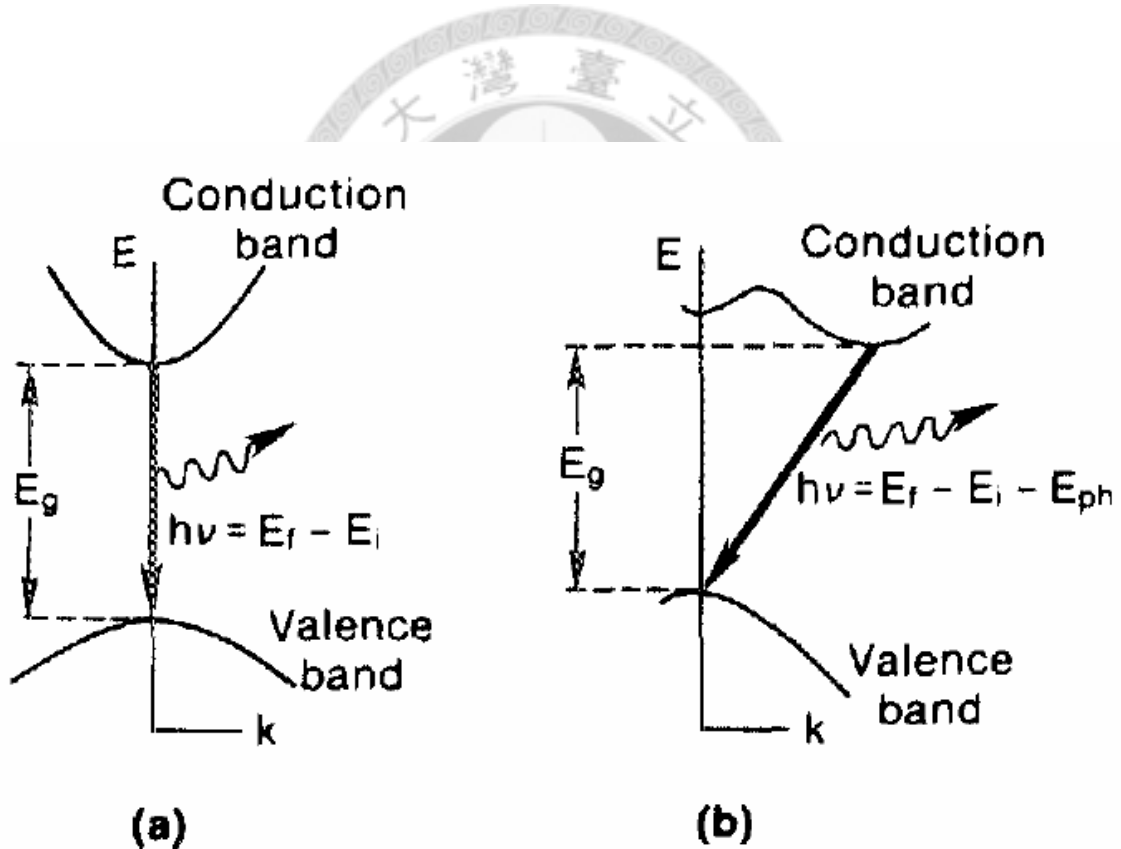


Fig. 2.4 Energy transitions in (a) direct and (b) indirect gap semiconductors between initial states E_i and final states E_f . For indirect transitions (b) the participation of a phonon (E_{ph}) is required.

A simplified set of radiative transitions that lead to emission in semiconductors is giving in Fig. 2.5.

Process 1 is an intraband transition: an electron is excited by a photon well above the conduction band edge dribbles down and reaches thermal equilibrium with the lattice. This thermalization process may lead to phonon-assisted photon emission or, more likely, phonon emission only.

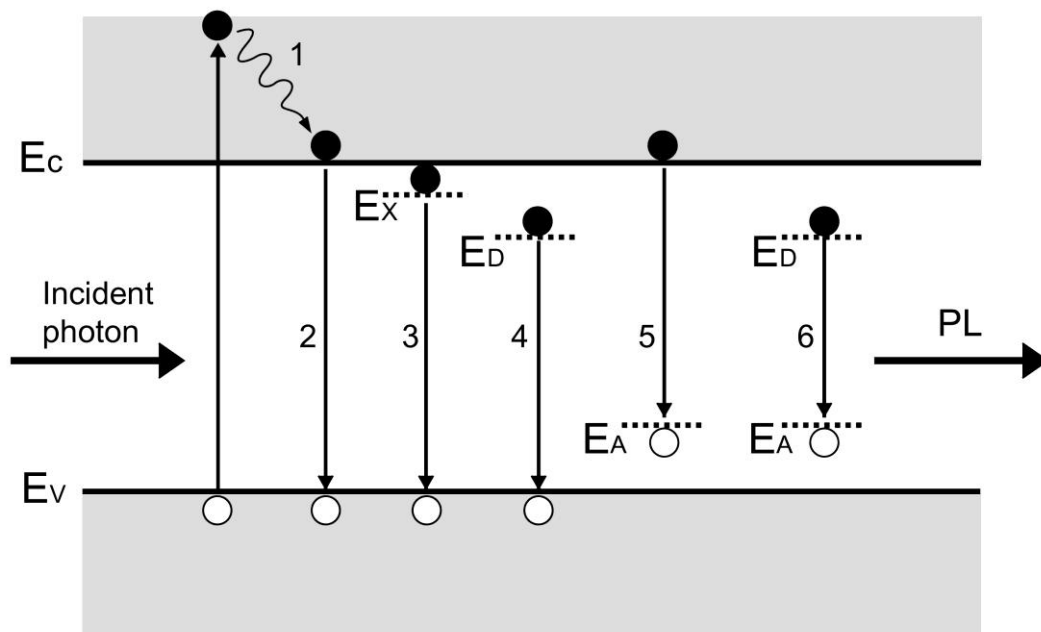


Fig. 2.5 Schematic diagram of radiative transitions between the conduction band (E_C), the valence band (E_V) and exciton (E_X), donor (E_D) and acceptor (E_A) levels in a semiconductor.

Process 2 is an interband transition: this produce intrinsic luminescence. In this case, direct recombination between an electron in the conduction band and a hole in

the valence band results in the emission of a photon of energy $h\nu=E_g$. Although this recombination occurs from states close to the corresponding band edges, the thermal distribution of carriers in these states will lead, in general, to a broad emission spectrum.

Process 3 is the exciton decay observable at low temperature. An exciton is a quasi-particle consisting of a Coulomb-correlated electron-hole pair. The Coulombic interaction between this pair, modified by the dielectric constant of the semiconductor, brings their energy levels closer together than the width of the energy gap. The exciton can wander through the crystal (the electron and the hole are only relatively free because they are associated as a mobile pair). Because of this mobility, the excitation is not a set of spatially localized states.⁷ Excitonic levels are observable at low temperature at which kT is smaller than the excitonic binding energy, which can be anything from an eV to tenths of an meV depending on the material. The recombination of an exciton will give rise to sharp-line luminescence, with energy of the band gap minus the binding energy of the exciton.

Process 4, 5, and 6 arise from transitions that start and/or finish on localized states of impurities (e.g. donors and acceptors) in the gap: these produce extrinsic luminescence. Process 4 represents the donor-to-free-hole transition as well as process 5 represents the free-electron-to-acceptor transition. Process 6 is the donor-acceptor

pair (DAP) recombination. Donor is substitutional atom with a higher number of valence electrons compared with the host atom, whereas acceptor is a substitutional atom with lower of valence electrons. Donor contributes excess electrons to the crystal, while acceptor tends to capture electrons or equivalently donate holes. Donor or acceptor may be electrically charged or neutral.⁸ As the neutral donor and the neutral acceptor are brought closer together, the donor's electron become increasingly shared by the acceptor. In other words, the donor and the acceptor become increasingly more ionized and form a pair.⁷ The energy of the DAP recombination emission in relatively pure crystals can be expressed by:

$$h\nu(r) = E_g - (E_A - E_D) + e^2/\epsilon r \quad (2.1)$$

where E_A and E_D are the binding energies of the acceptor and donor, respectively, ϵ is the dielectric constant, e is the electron charge, and r is the distance between the donor and acceptor impurities which participate in the recombination. The last term arises from the coulombic interaction of the carriers and depends on the separation r .

the radiative transition probability in this case is

$$P(r) = P(0)\exp(-2r/a) \quad (2.2)$$

where a is the Bohr radius of the less tightly bound center, and $P(0)$, the limiting transition probability as $r \rightarrow 0$, is a constant.

It should also be noted that not all recombination between electrons and holes

results in light emission, since there may also be efficient nonradiative recombination paths. Examples of nonradiative processes are (1) multi-phonon emission (i.e., direct conversion of the energy of an electron to heat); (2) the Auger effect, in which the energy of an electron transition is absorbed by another electron, which is raised to a higher-energy state in the conduction band, with subsequent emission of the phonons (thermalization); this process is especially important for high concentrations of excess charge carriers; and (3) recombination due to surface states and defects. These processes are more difficult to analyze.

2.1.3 Raman Scattering

Raman effect was discovered by the Indian physicist C. V. Raman in 1928. When a beam of light strikes a medium, most photons are elastically scattered, this is so-called Rayleigh scattering. In Rayleigh scattering, the emitted photon has the same wavelength as the absorbing photon. In Raman scattering, the energies of the incident and scattered photons are different. Raman spectroscopy is based on the Raman effect, which is the inelastic scattering of photons.⁹ The Raman effect comprises a very small fraction, about 1 in 10^6 , of the incident photons. Comparing with the PL signal, the Raman signal is relatively much weaker as shown in Fig. 2.6.

According to quantum theory, we can represent the oscillations of a crystal by phonons, which can be assumed to have discrete energy levels. Therefore, we can

picture light incident on a crystal and interacting with the crystal oscillations as an interaction between a photon and a phonon.

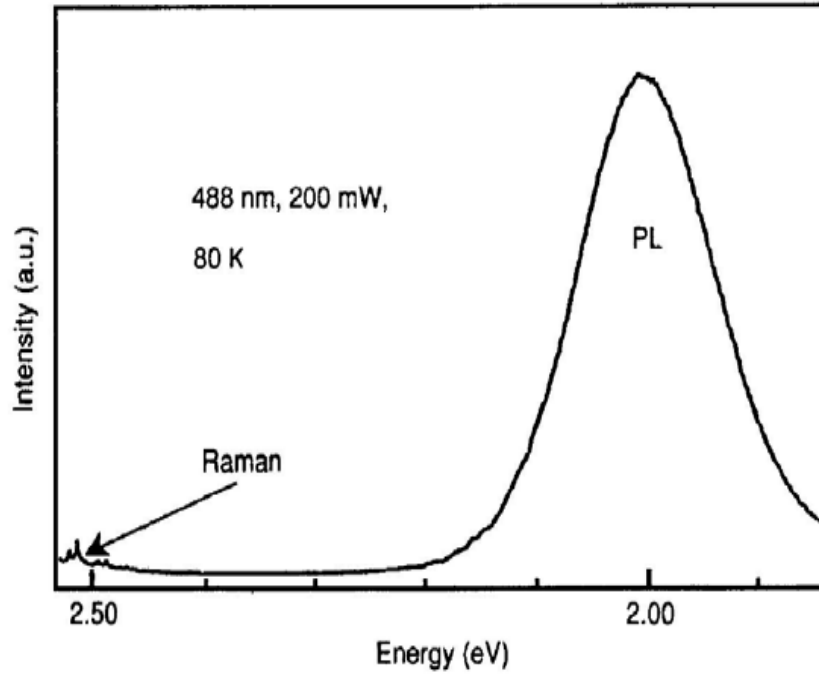


Fig. 2.6 This spectrum showing the photoluminescence peak and the Raman phonon mode of a CdMnTe film on a GaAs substrate (Perkowitz, 1991).

When a photon gains energy by absorbing a phonon, we say it anti-Stokes shifted.

When the photon loses energy by emission a phonon, we say it is Stokes shifted.⁹ Both of the processes must obey the energy and momentum conservation rules. The conservation conditions can be written as:

$$h\nu_i = h\nu_s \pm h\Omega \quad (2.3)$$

$$k_i = k_s \pm K \quad (2.4)$$

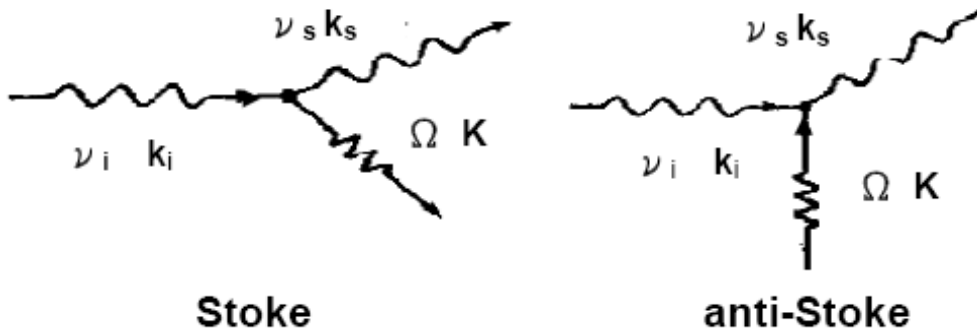


Fig. 2.7 The diagram shows the conservation rules in the Raman scattering.

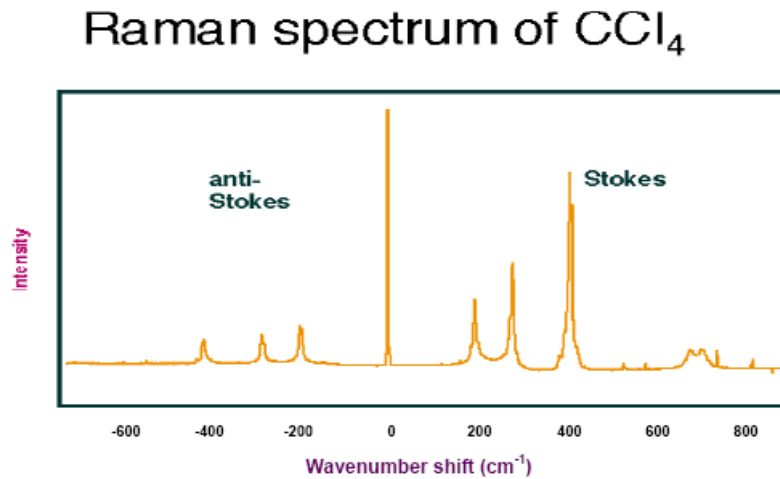


Fig. 2.8 The Raman spectrum of CCl₄.

where ν_i and ν_s are the incoming and scattered photon frequencies respectively, \mathbf{k}_i and \mathbf{k}_s are the incoming and scattered photon wave vectors respectively, while Ω and \mathbf{K} are the phonon frequency and wave vector respectively [Fig. 2.7]. The values of frequency shift resulting from Raman scattering range from ten to a few thousand cm^{-1} . Normally speaking, the intensity of the Stokes component is much stronger than that of the anti-Stokes line because usually there are few phonons to be absorbed

compared to the number of phonon that can be emitted. Figure 2.8 is a typical Raman spectrum of CCl_4 shows the anti-Stokes shifted and the Stokes shifted. The line at the middle of the figure, denoted by zero, shows the spectral position of the incident monochromatic laser. It also denotes the Rayleigh scattering.

Through the theoretical calculation, the lattice vibrations can be distinguished to longitudinal acoustic and optical (LA and LO) and transverse acoustic and optical (TA and TO) modes. In a Raman spectrum, the Rayleigh scattering is not shifted, the magnitude of a shift is determined by a optical phonon energy, which is in the range of a approximately 5 meV to 250 meV, and the energy shift is in the range of 6×10^{-3} meV to 0.1 meV for acoustic phonons. Because the phonon frequencies are so small, the high resolution techniques are needed to detect them. Raman scattering is inherently a weak process, but lasers provide enough power so that the spectra can be routinely measured. Figure 2.9 shows a simplified Raman spectroscopy experiment setup with a charge-coupled device (CCD) as the detector. One thing needs to be emphasized is that those Raman shifts measured are precisely the frequencies of crystal oscillations regardless of the frequency of incident light.

Not every mode can be observed in a Raman spectrum. The Raman scattering must satisfy the selection rules, such as conservation of momentum and energy as well as the point-group selection rules. These originate from the fact that the crystal

unit cell is invariant under only a certain set of symmetry operations, and in fact, it is this set of symmetry operations which defines the crystal point group. Similarly, the phonon behavior also has transformation properties. If these transformation properties do not satisfy certain requirements, which depend on the crystal point group, then light will not be scattered. Crystal point-group selection rules are a simple yet powerful way to determine and distinguish between phonon modes of different symmetries.

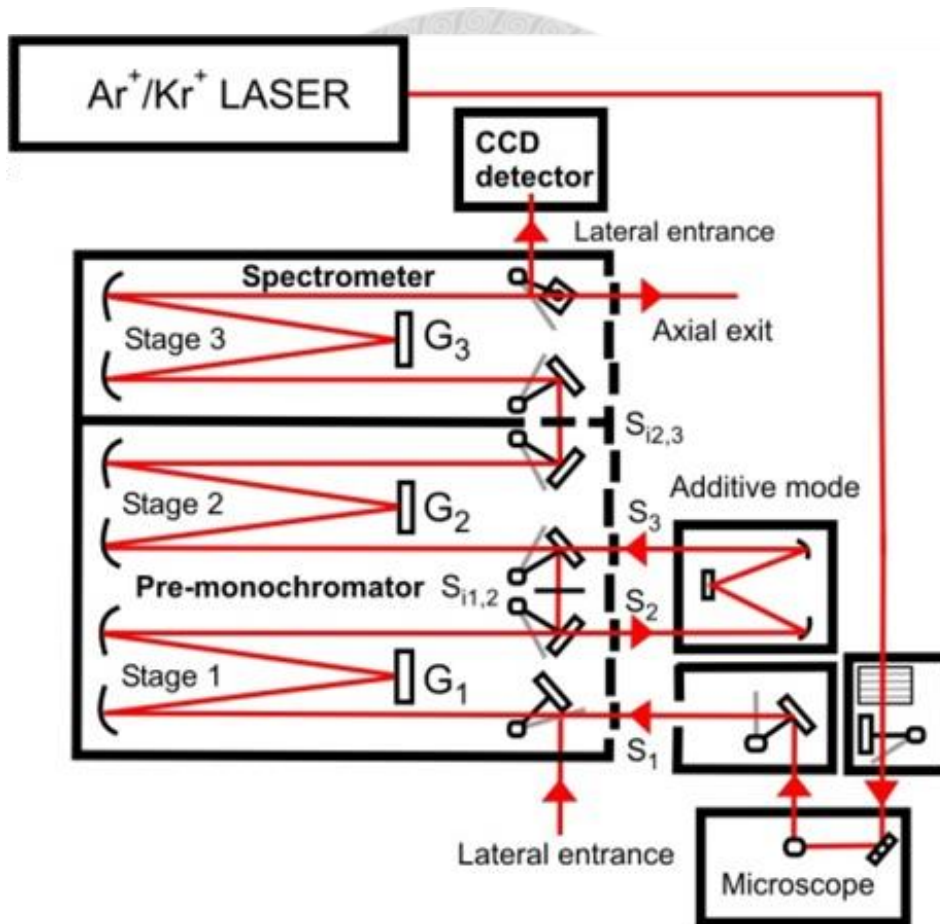


Fig. 2.9 A simplified Raman spectroscopy experiment setup with a charge-coupled device (CCD) as the detector.

All the main Raman parameters like band frequencies and intensities, line shape and linewidth, polarization behavior can be used to characterize the lattice, impurities, and free carriers in a semiconductor. The intensity gives information about crystallinity since it may be reduced in crystals damaged by ion bombardment or other means. The linewidth increases when a material is damaged or disordered because these conditions increase phonon damping or change the rules for momentum conservation in the Raman process. The strengths and frequencies of the Raman phonon bands can determine the degree of alloying in a mixed material. All these capabilities can be used for layered microstructures as well as bulk materials, subject only to the limitation that the penetration depth of the exciting radiation ranges from a few hundred nanometers to a micrometer. However, a change in the wavelength of the exciting radiation changes the penetration, giving flexibility in the probe depth. The small wavelength of excitation radiation, combined with Raman microprobe technique, also provides good spatial resolution.

Owing to the close relation between Raman scattering and the oscillations of atoms and molecules inside the materials, we can gain the information about the oscillations of atoms and molecules inside the materials from Raman scattering spectrum. These oscillations are mainly controlled by interatomic or intermolecular interactions. Raman-scattering researches can therefore provide a way for people to

understand these interaction forces.

2.1.4 X-ray Diffraction

Crystals are regular arrays of atoms, and X-rays can be considered waves of electromagnetic radiation. Atoms scatter X-ray waves, primarily through the atoms' electrons. Just as an ocean wave striking a lighthouse produces secondary circular waves emanating from the lighthouse, so an X-ray striking an electron produces secondary spherical waves emanating from the electron. This phenomenon is known as elastic scattering, and the electron (or lighthouse) is known as the scatterer. A regular array of scatterers produces a regular array of spherical waves. Although these waves cancel one another out in most directions through destructive interference, they add constructively in a few specific directions, determined by Bragg's law:

$$2d \sin \theta = n\lambda, \quad (2.5)$$

where d is the spacing between diffracting planes, θ is the incident angle, n is any integer, and λ is the wavelength of the beam. These specific directions appear as spots on the diffraction pattern called reflections. Thus, X-ray diffraction results from an electromagnetic wave (the X-ray) impinging on a regular array of scatterers (the repeating arrangement of atoms within the crystal).

X-rays are used to produce the diffraction pattern because their wavelength λ is typically the same order of magnitude (1–100 angstroms) as the spacing d between

planes in the crystal. In principle, any wave impinging on a regular array of scatterers produces diffraction, as predicted first by Francesco Maria Grimaldi in 1665. To produce significant diffraction, the spacing between the scatterers and the wavelength of the impinging wave should be similar in size. For illustration, the diffraction of sunlight through a bird's feather was first reported by James Gregory in the later 17th century. The first artificial diffraction gratings for visible light were constructed by David Rittenhouse in 1787, and Joseph von Fraunhofer in 1821. However, visible light has too long a wavelength (typically, 5500 angstroms) to observe diffraction from crystals. Prior to the first X-ray diffraction experiments, the spacings between lattice planes in a crystal were not known with certainty.

The idea that crystals could be used as a diffraction grating for X-rays arose in 1912 in a conversation between Paul Peter Ewald and Max von Laue in the English Garden in Munich. Ewald had proposed a resonator model of crystals for his thesis, but this model could not be validated using visible light, since the wavelength was much larger than the spacing between the resonators. Von Laue realized that electromagnetic radiation of a shorter wavelength was needed to observe such small spacings, and suggested that X-rays might have a wavelength comparable to the unit-cell spacing in crystals. Von Laue worked with two technicians, Walter Friedrich and his assistant Paul Knipping, to shine a beam of X-rays through a copper sulfate

crystal and record its diffraction on a photographic plate. After being developed, the plate showed a large number of well-defined spots arranged in a pattern of intersecting circles around the spot produced by the central beam.^{10,11} Von Laue developed a law that connects the scattering angles and the size and orientation of the unit-cell spacings in the crystal, for which he was awarded the Nobel Prize in Physics in 1914.¹²

As described in the mathematical derivation below, the X-ray scattering is determined by the density of electrons within the crystal. Since the energy of an X-ray is much greater than that of a valence electron, the scattering may be modeled as Thomson scattering, the interaction of an electromagnetic ray with a free electron. This model is generally adopted to describe the polarization of the scattered radiation. The intensity of Thomson scattering declines as $1/m^2$ with the mass m of the charged particle that is scattering the radiation; hence, the atomic nuclei, which are thousands of times heavier than an electron, contribute negligibly to the scattered X-rays.

2.1.5 Scanning Electron Microscope

The types of signals produced by a scanning electron microscope (SEM) include secondary electrons, back-scattered electrons (BSE), characteristic X-rays, light (cathodoluminescence), specimen current and transmitted electrons.¹³ Secondary electron detectors are common in all SEMs, but it is rare that a single machine would

have detectors for all possible signals. The signals result from interactions of the electron beam with atoms at or near the surface of the sample. In the most common or standard detection mode, secondary electron imaging or SEI, the SEM can produce very high-resolution images of a sample surface, revealing details less than 1 nm in size. Due to the very narrow electron beam, SEM micrographs have a large depth of field yielding a characteristic three-dimensional appearance useful for understanding the surface structure of a sample. This is exemplified by the micrograph of pollen shown above. A wide range of magnifications is possible, from about 10 times (about equivalent to that of a powerful hand-lens) to more than 500,000 times, about 250 times the magnification limit of the best light microscopes. Back-scattered electrons (BSE) are beam electrons that are reflected from the sample by elastic scattering. BSE are often used in analytical SEM along with the spectra made from the characteristic X-rays. Because the intensity of the BSE signal is strongly related to the atomic number (Z) of the specimen, BSE images can provide information about the distribution of different elements in the sample. For the same reason, BSE imaging can image colloidal gold immuno-labels of 5 or 10 nm diameter, which would otherwise be difficult or impossible to detect in secondary electron images in biological specimens. Characteristic X-rays are emitted when the electron beam removes an inner shell electron from the sample, causing a higher-energy electron to

fill the shell and release energy. These characteristic X-rays are used to identify the composition and measure the abundance of elements in the sample.

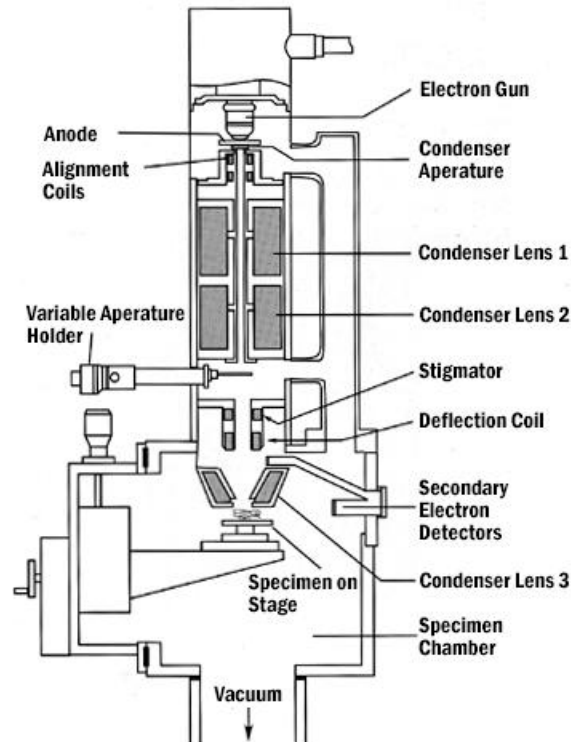


Fig. 2.10 The structural scheme of a typical scanning electron microscope.

In a typical SEM as shown in Fig. 2.10, an electron beam is thermionically emitted from an electron gun fitted with a tungsten filament cathode. Tungsten is normally used in thermionic electron guns because it has the highest melting point and lowest vapour pressure of all metals, thereby allowing it to be heated for electron emission, and because of its low cost. Other types of electron emitters include lanthanum hexaboride (LaB₆) cathodes, which can be used in a standard tungsten filament SEM if the vacuum system is upgraded and field emission guns (FEG),

which may be of the cold-cathode type using tungsten single crystal emitters or the thermally assisted Schottky type, using emitters of zirconium oxide.

The electron beam, which typically has an energy ranging from 0.2 keV to 40 keV, is focused by one or two condenser lenses to a spot about 0.4 nm to 5 nm in diameter. The beam passes through pairs of scanning coils or pairs of deflector plates in the electron column, typically in the final lens, which deflect the beam in the x and y axes so that it scans in a raster fashion over a rectangular area of the sample surface.

When the primary electron beam interacts with the sample, the electrons lose energy by repeated random scattering and absorption within a teardrop-shaped volume of the specimen known as the interaction volume, which extends from less than 100 nm to around 5 μm into the surface. The size of the interaction volume depends on the electron's landing energy, the atomic number of the specimen and the specimen's density. The energy exchange between the electron beam and the sample results in the reflection of high-energy electrons by elastic scattering, emission of secondary electrons by inelastic scattering and the emission of electromagnetic radiation, each of which can be detected by specialized detectors. The beam current absorbed by the specimen can also be detected and used to create images of the distribution of specimen current. Electronic amplifiers of various types are used to amplify the signals, which are displayed as variations in brightness on a computer

monitor (or, for vintage models, on a cathode ray tube). Each pixel of computer videomemory is synchronised with the position of the beam on the specimen in the microscope, and the resulting image is therefore a distribution map of the intensity of the signal being emitted from the scanned area of the specimen. In older microscopes image may be captured by photography from a high-resolution cathode ray tube, but in modern machines image is saved to computer data storage.

For conventional imaging in the SEM, specimens must be electrically conductive, at least at the surface, and electrically grounded to prevent the accumulation of electrostatic charge at the surface. Metal objects require little special preparation for SEM except for cleaning and mounting on a specimen stub. Nonconductive specimens tend to charge when scanned by the electron beam, and especially in secondary electron imaging mode, this causes scanning faults and other image artifacts. They are therefore usually coated with an ultrathin coating of electrically conducting material, deposited on the sample either by low-vacuum sputter coating or by high-vacuum evaporation. Conductive materials in current use for specimen coating include gold, gold/palladium alloy, platinum, osmium, iridium, tungsten, chromium, and graphite. Additionally, coating may increase signal/noise ratio for samples of low atomic number (Z). The improvement arises because secondary electron emission for high- Z materials is enhanced.

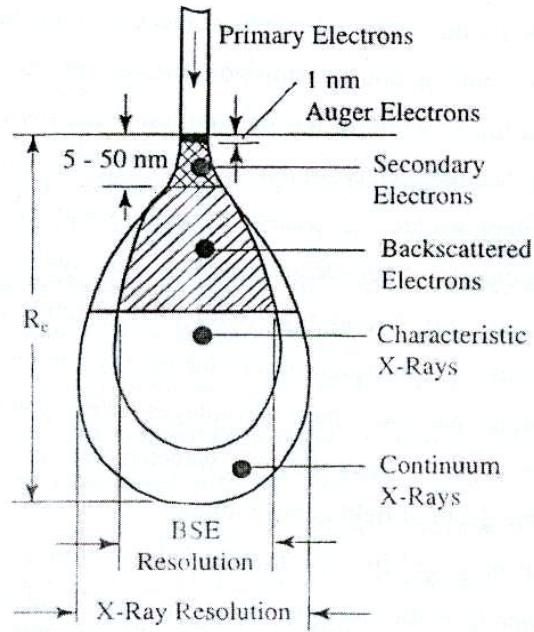


Fig. 2.11 Summary of the range and spatial resolution of backscattered electrons, secondary electrons, X-rays, and Auger electrons for electrons incident on a solid.

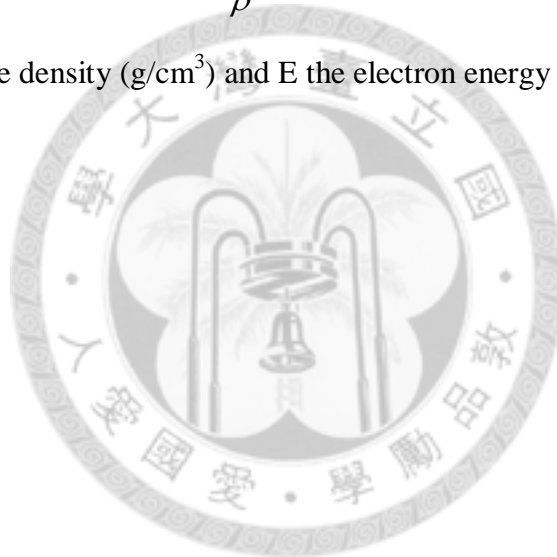
The generation volume is a function of the e-beam energy and the atomic number Z of the sample. Secondary electrons, backscattered electrons, characteristic and continuum X-rays, Auger electrons, photons, and electron-hole pairs are produced. For low- Z samples most electrons penetrate deeply into the sample and are absorbed. For high- Z samples there is considerable scattering near the surface and a large fraction of the incident electrons is backscattered. The shape of the electron distribution is “teardrop”-shaped, as shown in Fig. 2.11. As Z increase ($15 < Z < 40$) the shape becomes more spherical and for $Z > 40$ it becomes hemispherical. “Teardrop” shapes have been observed by exposing polymethylmethacrylate to an electron beam

and etching the exposed portion of the material. Electron trajectories, calculated with Monte Carlo techniques, also agree with these shapes.

The depth of electron penetration is the electron range R_e , defined as the average total distance from the sample surface that an electron travels in the sample along a trajectory. A number of empirical expressions have been derived for R_e . One such expression is

$$R_e = \frac{4.28 \times 10^{-6} E^{1.75}}{\rho} \text{ (cm)} , \quad (2.6)$$

where ρ is the sample density (g/cm^3) and E the electron energy (keV).



2.2 Growth Methods

2.2.1 Metal-organic Chemical Vapor Deposition

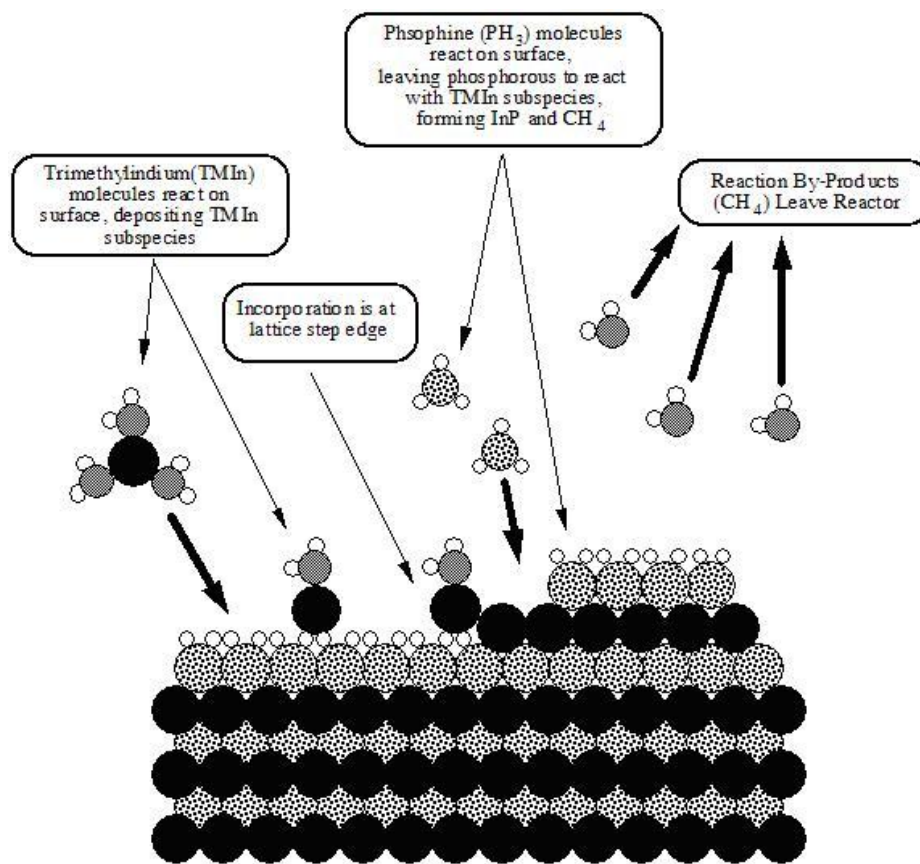


Fig. 2.12 A schematic illustration in metal-organic chemistry vapor deposition.

Metal-organic chemistry vapor deposition (MOCVD) is a chemical vapor deposition method of epitaxial growth of materials, especially compound semiconductors from the surface reaction of organic compounds or metal-organics and metal hydrides containing the required chemical elements. For example, indium phosphide could be grown in a reactor on a substrate by introducing trimethylindium

$((\text{CH}_3)_3\text{In})$ and phosphine (PH_3).¹⁴ Formation of the epitaxial layer occurs by final pyrolysis of the constituent chemicals at the substrate surface as shown in Fig 2.12. In contrast to molecular beam epitaxy (MBE) the growth of crystals is by chemical reaction and not physical deposition. This takes place not in a vacuum, but from the gas phase at moderate pressures (2 to 100 kPa). As such this technique is preferred for the formation of devices incorporating thermodynamically metastable alloys. It has become the dominant process for the manufacture of laser diodes, solar cells, and LEDs.

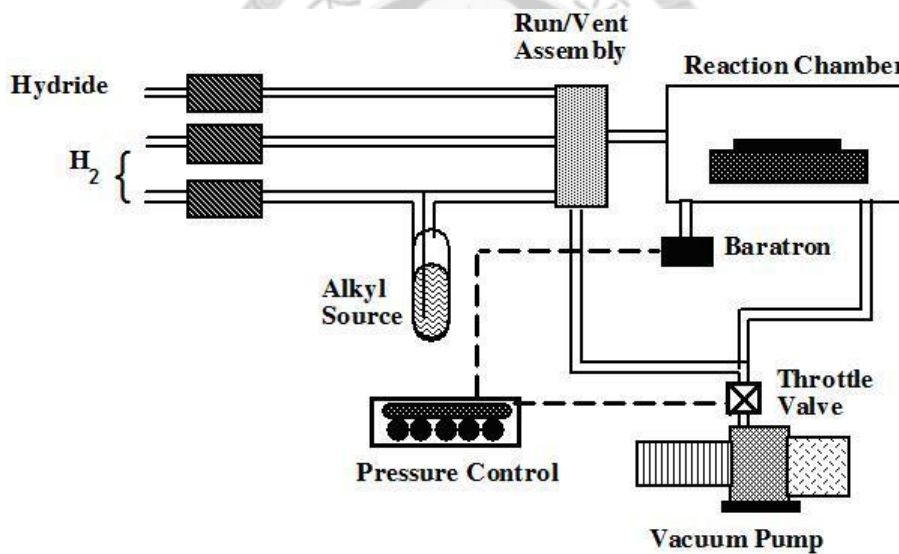


Fig. 2.13 A schematic illustration of the apparatus of metal-organic chemistry vapor deposition.

Figure 2.13 shows the apparatus of MOCVD, and we describe four major parts in it as follows:

- **Reactor:** A reactor is a chamber made of a material that does not react with the

chemicals being used. It must also withstand high temperatures. This chamber is composed by reactor walls, liner, a susceptor, gas injection units, and temperature control units. Usually, the reactor walls are made from stainless steel or quartz. To prevent over heating, cooling water must be flowing through the channels within the reactor walls. Special glasses, such as quartz or ceramic, are often used as the liner in the reactor chamber between the reactor wall and the susceptor. A substrate sits on a susceptor which is at a controlled temperature. The susceptor is made from a material resistant to the metal-organic compounds used; graphite is sometimes used. For growing nitrides and related materials, a special coating on the graphite susceptor is necessary to prevent corrosion by ammonia (NH_3) gas.

● **Gas inlet and switching system:** Gas is introduced via devices known as “bubblers”. In a bubbler a carrier gas (usually nitrogen or hydrogen) is bubbled through the metal-organic liquid, which picks up some metal-organic vapor and transports it to the reactor. The amount of metal-organic vapor transported depends on the rate of carrier gas flow and the bubbler temperature. Allowance must be made for saturated vapors.

● **Pressure maintenance system:** Since the deposition process has to occur in constantly vacuum environment, the pump should work to exhaust nearly all gas to maintain at the necessary pressure.

- **Gas Exhaust and cleaning System:** Toxic waste products must be converted to liquid or solid wastes for recycling (preferably) or disposal. Ideally processes will be designed to minimize the production of waste products.

2.2.2 Vapor-liquid-solid Growth

Vapor-liquid-solid (VLS) growth, as an effective route to fabricate semiconductor nanowires (NWs) and nanorods (NRs), has been extensively used since it was proposed by Wagner and Ellis in 1964.¹⁵ The main features of VLS growth are that semiconductor NWs have metal or alloy droplets on their tips and these droplets (as catalysts) define their diameters and direct their growth orientation. To date, many studies have focused on controlled diameter of semiconductor NWs using the VLS mechanism, as well as thermodynamic and kinetic size limit of NWs' growth. However, few studies of semiconductor NWs growth kinetics are performed, especially theoretical studies. The purpose of this work is to present the effects of semiconductor NWs' size on its growth kinetics by the VLS mechanism and to give the dependences of growth rate and activation energy of crystallization on size quantitatively.

The typical VLS growth process is shown schematically in Fig 2.14. Generally, VLS growth can be divided by three main steps:

- **Metal Catalyst:** A thin metal film is deposited on the substrate and annealed to

form nanoclusters.

- **Vapor-Liquid Process:** During growth, the gas precursor carrying source atoms is catalyzed by the liquid metal-semiconductor nanoclusters (the tips of nanowires), and the source atoms are melted into the nanoclusters.

- **Liquid-Solid Process:** Once the liquid is supersaturated with source atoms, the precipitation happens at the bottom of liquid (the liquid-solid interface), thus pushing the wire growth and also keeping the catalyst on the top of wires.

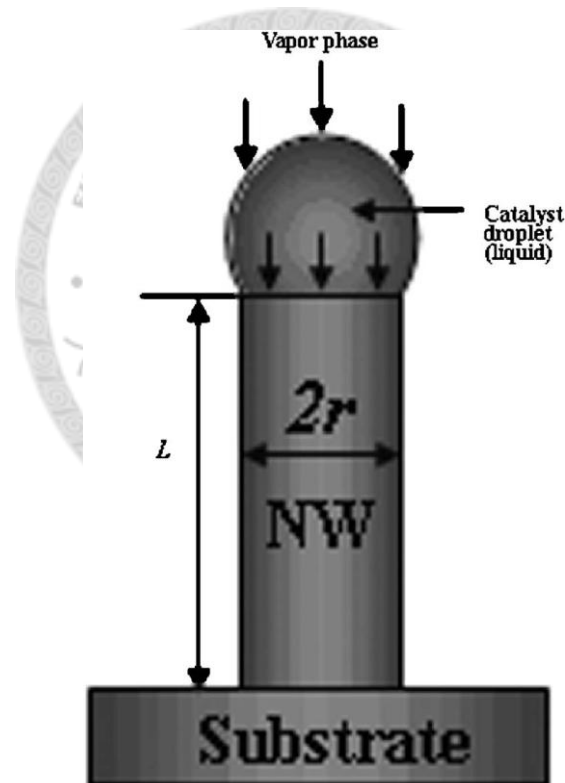


Fig. 2.14 The illustration of vapor-liquid-solid growth process.

For a steady VLS growth process, NW growth species in the liquid droplet should remain in balance, i.e., the number of atoms transferred from the vapor phase

to the droplet per unit time is equal to that transformed from liquid to the crystal phase. The nanowires have several sidewall facets and the number of sidewalls decreases with increasing growth temperature. Growth can happen at both the tip and sidewall, which might widen the nanowires; however, the sidewall growth is not catalyzed, thus the rate is much slower than the tip.

2.2.3 Hydrothermal Growth of ZnO Nanorods

ZnO nanorod were synthesized from zinc nitrate in a neutral aqueous solution under hydrothermal conditions.¹⁶ The procedure consists of two steps: (1) modification of substrates with a thin layer of densely and uniformly dispersed ZnO nanoparticles by sputtering, and (2) hydrothermal growth of ZnO nanorods in aqueous solution. In detail, zinc nanoparticles should be sputtered onto the substrate and oxidized spontaneously in air. The subsequent hydrothermal growth was carried out at 95°C in a sealed kettle by immersing the modified substrates in the aqueous solution (80 mL) containing Zn(NO₃)₂ (0.1 mol/L) and methenamine (0.1 mol/L). Finally, the samples were washed with deionized water and allowed to dry in air before characterization.

2.2.4 DC Sputtering Deposition

A sputtering system (JFC-1600, JEOL) is used in this work. As shown in Fig. 2.15, during sputtering, the substrate is placed in a vacuum chamber with a target of

the material to be deposited. The plasma is generated in a passive source gas (i.e. Argon or air) in the chamber and the ion bombardment is directed towards the target, causing material to be sputtered off the target and condense on the chamber walls and the substrate. A strong magnetic field (magnetron) can be used to concentrate the plasma near the target to increase the deposition rate.¹⁷

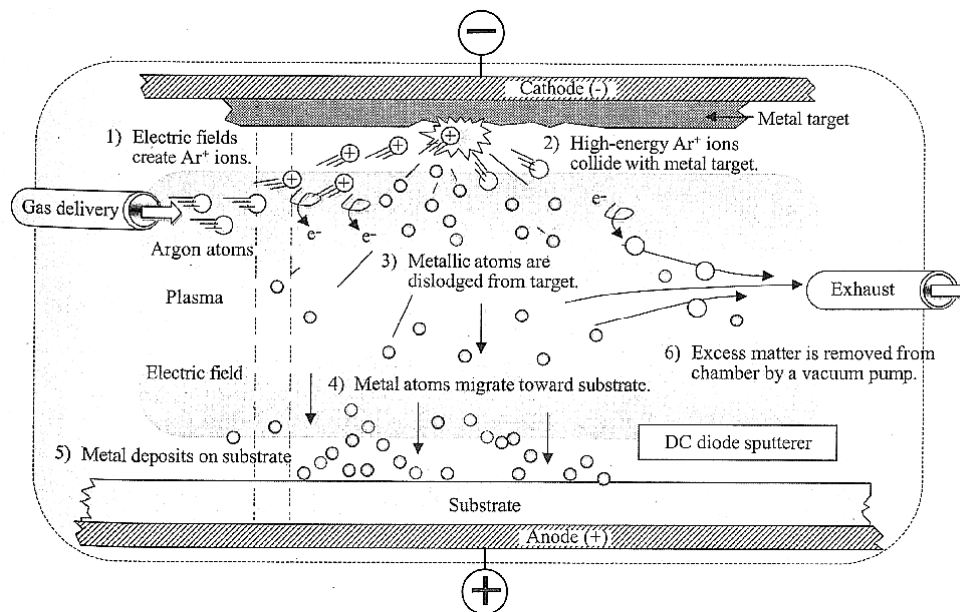


Fig.2.15 A schematic illustration of the apparatus of DC sputtering deposition.

Early days, the method of sputter deposition was used to deposit the thin film, or applying the metal in the fabric. When the vacuum technology matures, the sputtering is largely replaced by the evaporation, due to the rate of latter is faster than the former. However, many materials are unable to evaporate by heating the resistance, so this method is still extensively used to produce the composite.

2.3 Physics of Materials

2.3.1 Piezoelectricity

In piezoelectric crystals, the application of a compressive or expansive force results in a change corresponding to the distribution of dipole moments. This causes a change in the surface charge, which is proportional to the applied force as shown in Fig. 2.16. This phenomenon is called piezoelectricity.

The nature of the piezoelectric effect is closely related to the occurrence of electric dipole moments in solids. The latter may either be induced for ions on crystal lattice sites with asymmetric charge surroundings (such as in BaTiO_3 , PZTs, and wurtzite structure semiconductors) or may directly be carried by molecular groups (as in cane sugar). The dipole density or polarization (dimensionality $[\text{Cm/m}^3]$) may easily be calculated for crystals by summing up the dipole moments per volume of the crystallographic unit cell.¹⁸ As every dipole is a vector, the dipole density \mathbf{P} is also a vector or a directed quantity. Dipoles near each other tend to be aligned in regions called Weiss domains. The domains are usually randomly oriented, but can be aligned using the process of poling (not the same as magnetic poling), a process by which a strong electric field is applied across the material, usually at elevated temperatures. Not all piezoelectric materials can be poled.¹⁹

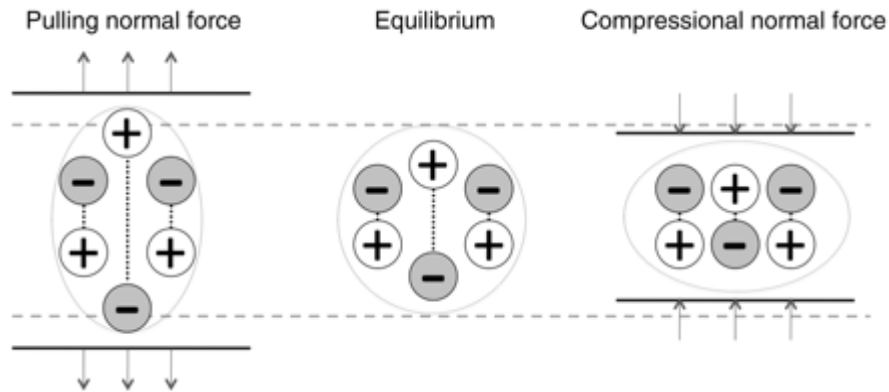


Fig. 2.16 An illustration of the piezoelectricity concept.

Of decisive importance for the piezoelectric effect is the change of polarization \mathbf{P} when applying a mechanical stress. This might either be caused by a re-configuration of the dipole-inducing surrounding or by re-orientation of molecular dipole moments under the influence of the external stress. Piezoelectricity may then manifest in a variation of the polarization strength, its direction or both, with the details depending on (1) the orientation of \mathbf{P} within the crystal, (2) crystal symmetry and (3) the applied mechanical stress. The change in \mathbf{P} appears as a variation of surface charge density upon the crystal faces, i.e. as a variation of the electrical field extending between the faces, since the units of surface charge density and polarization are the same, $[\text{C}/\text{m}^2] = [\text{Cm}/\text{m}^3]$. However, piezoelectricity is not caused by a change in charge density on the surface, but by dipole density in the bulk. For example, a 1 cm^3 cube of quartz with 2 kN (500 lbf) of correctly applied force can produce a voltage of 12500 V.²⁰

Piezoelectric materials also show the opposite effect, called converse piezoelectric effect, where the application of an electrical field creates mechanical deformation in the crystal.

2.3.2 Quantum Confined Stark Effect

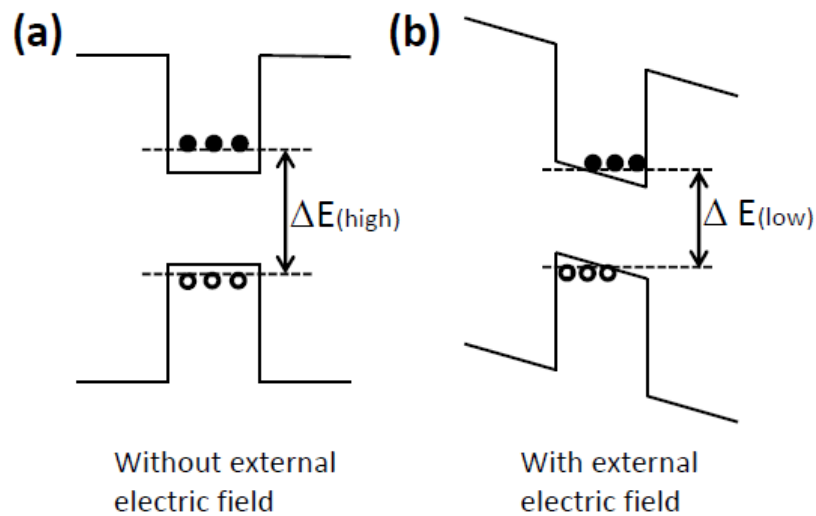


Fig. 2.17 Illustration diagram of the band structure of MQWs (a) without and (b) with external electric field.

The quantum-confined Stark effect (QCSE) describes the effect of an external electric field upon the light absorption spectrum or emission spectrum of quantum wells (QWs).²¹ In the absence of an external electric field, electrons and holes within the quantum well may only occupy states within a discrete set of energy subbands. Consequently, only a discrete set of frequencies of light may be absorbed or emitted by the system. When an external electric field is applied, the electron states shift to

lower energies, while the hole states shift to higher energies as shown in Fig. 2.17. This reduces the permitted light absorption or emission frequencies. Additionally, the external electric field shifts electrons and holes to opposite sides of the well, decreasing the overlap integral, which in turn reduces the recombination efficiency (ie. fluorescence quantum yield) of the system. The spatial separation between the electrons and holes is limited by the presence of the potential barriers around the quantum well, meaning that excitons are able to exist in the system even under the influence of an electric field. The quantum-confined Stark effect is used in QCSE optical modulators, which allow optical communications signals to be switched on and off rapidly.

2.3.3 Zinc Oxide

Zinc oxide (ZnO) crystallizes in two main forms, hexagonal wurtzite and cubic zincblende.²² The wurtzite structure is most stable at ambient conditions and thus most common. The zinc-blende form can be stabilized by growing ZnO on substrates with cubic lattice structure. In both cases, the zinc and oxide centers are tetrahedral, the most characteristic geometry for Zn(II). Hexagonal and zincblende polymorphs have no inversion symmetry (reflection of a crystal relative to any given point does not transform it into itself). This and other lattice symmetry properties result in piezoelectricity of the hexagonal and zincblende ZnO, and pyroelectricity of

hexagonal ZnO. Most ZnO has n-type character, even in the absence of intentional doping. Nonstoichiometry is typically the origin of n-type character, but the subject remains controversial. An alternative explanation has been proposed, based on theoretical calculations, that unintentional substitutional hydrogen impurities are responsible. Controllable n-type doping is easily achieved by substituting Zn with group-III elements such as Al, Ga, In or by substituting oxygen with group-VII elements chlorine or iodine.

Reliable p-type doping of ZnO remains difficult. This problem originates from low solubility of p-type dopants and their compensation by abundant n-type impurities. This problem is observed with GaN and ZnSe. Measurement of p-type in "intrinsically" n-type material is complicated by the inhomogeneity of samples. Current limitations to p-doping does not limit electronic and optoelectronic applications of ZnO, which usually require junctions of n-type and p-type material. Known p-type dopants include group-I elements Li, Na, K; group-V elements N, P and As, as well as copper and silver. However, many of these form deep acceptors and do not produce significant p-type conduction at room temperature.

ZnO has wide direct band gap (3.37 eV or 375 nm at room temperature). Therefore, its most common potential applications are in laser diodes and light emitting diodes (LEDs). Some optoelectronic applications of ZnO overlap with that of

GaN, which has a similar bandgap (~3.4 eV at room temperature). Compared to GaN, ZnO has a larger exciton binding energy (~60 meV, 2.4 times of the room-temperature thermal energy), which results in bright room-temperature emission from ZnO. ZnO can be combined with GaN for LED-applications. For instance as TCO layer and ZnO nanostructures provide better light outcoupling. Other properties of ZnO favorable for electronic applications include its stability to high-energy radiation and to wet chemical etching. Radiation resistance makes ZnO a suitable candidate for space applications. ZnO is the most promising candidate in the field of random lasers to produce an electronically pumped UV laser source. The pointed tips of ZnO nanorods result in a strong enhancement of an electric field. Therefore, they can be used as field emitters. Aluminium-doped ZnO layers are used as a transparent electrodes. The constituents Zn and Al are much cheaper and less poisonous compared to the generally used indium tin oxide (ITO). One application which has begun to be commercially available is the use of ZnO as the front contact for solar cells or of liquid crystal displays. Transparent thin-film transistors (TTFT) can be produced with ZnO. As field-effect transistors, they even may not need a p–n junction, thus avoiding the p-type doping problem of ZnO. Some of the field-effect transistors even use ZnO nanorods as conducting channels.

ZnO nanorod sensors are devices detecting changes in electrical current passing

through ZnO nanowires due to adsorption of gas molecules. Selectivity to hydrogen gas was achieved by sputtering Pd clusters on the nanorod surface. The addition of Pd appears to be effective in the catalytic dissociation of hydrogen molecules into atomic hydrogen, increasing the sensitivity of the sensor device. The sensor detects hydrogen concentrations down to 10 parts per million at room temperature, whereas there is no response to oxygen. ZnO has also been considered for spintronics applications: if doped with 1–10% of magnetic ions (Mn, Fe, Co, V, etc.), ZnO could become ferromagnetic, even at room temperature. Such room temperature ferromagnetism in ZnO:Mn has been observed, but it is not clear yet whether it originates from the matrix itself or from secondary oxide phases.

2.3.4 III-nitride Semiconductors

Recently, III-nitride semiconductors have become a subject of intense research. The unique features of these materials (GaN, AlN, InN, and their alloys) i.e., a wide direct bandgap, strong chemical bonds, and a high melting temperature make them well suited for designing and fabricating optoelectronic and high temperature/power devices. The III-nitrides have been viewed as a promising system for semiconductor device applications in the blue and UV wavelengths. The wurtzite polytypes of GaN, AlN and InN form a continuous alloy system whose direct band gaps range from 1.9 eV for InN, to 3.4 eV for GaN, to 6.2 eV for AlN.

InGaN alloys recently emerge as a new solar cell materials system due to their tunable energy band gaps (varying from 0.7 eV for InN to 3.4 eV for GaN, covering almost the whole solar spectrum) and superior photovoltaic characteristics (direct energy band gap in the entire alloy range and high carrier mobility, drift velocity, radiation resistance, and optical absorption of $\sim 10^5 \text{ cm}^{-1}$ near the band edge).²³ III-nitride multijunction solar cells with near ideal band gaps for maximum solar energy conversion efficiency must incorporate InGaN layers with higher In contents or lower energy band gaps.

Several techniques have been used for the epitaxial growth of III-V nitride semiconductors. Among these techniques, molecular-beam epitaxy and MOCVD have been the most popular, mainly due to their wide use in the fabrication of most III-V compound semiconductors. However, MOCVD may be more suitable for high-volume production for this material system for two reasons: higher throughput (lower cost) and demonstrated superior material quality.²⁴

For blue and green LEDs, InGaN films with high indium content are required. Nakamura and coworkers describe the growth of high-quality InGaN films by adjusting the growth rate and growth temperatures to optimize material quality and emission wavelength. With all the building blocks available, high-efficiency commercial blue and green nitride-based LEDs are currently available from more than

one source. The brightest devices use either a single or multiple quantum well structure (Figure 2). A typical complete device structure consists of a low-temperature deposited GaN or AlN buffer layer on c-plane sapphire, a 3-4 μm silicon-doped GaN layer, a SQW or multiple quantum well (MQW), a 1,000 \AA magnesium-doped AlGaIn layer, and a 3,000 \AA magnesium-doped GaN layer.

With the commercialization of InGaIn quantum-well LEDs in the blue through green spectral regions, there now exists solid-state light sources spanning the entire visible spectral region. High-brightness LEDs in the yellow-green through red-orange spectral region are commercially produced with the AlInGaP material system and in the red spectral region with the transparent-substrate AlGaAs material system. It is readily apparent that solid-state LEDs are rapidly encroaching upon the performance levels of traditional light sources and, in most cases, significantly exceed filtered filament-based light of a specific color.

Several major markets are being addressed with these newly developed solid-state light sources. Automobile exterior lighting has been moving rapidly to incorporate transparent-substrate AlInGaP technology into high-mount stop lights and into the full amber and red-orange taillight assembly. Full-color, outdoor, changeable message signs and full-motion video displays have been adopting (AlIn)GaIn and AlInGaP technologies and will continue to proliferate as costs are reduced.

Traffic-signal applications have begun to incorporate red AlInGaP and AlGaAs LEDs for stop lights and are moving toward incorporating amber and blue-green LEDs to produce a completely LED-based signal head. All of these markets are rapidly expanding and will provide enormous growth opportunities in the future.

2.3.5 Light-emitting Diodes

A light-emitting diode (LED) consists of a chip of semiconducting material doped with impurities to create a p-n junction.²⁵ As in other diodes, current flows easily from the p-side, or anode, to the n-side, or cathode, but not in the reverse direction. Charge-carriers—electrons and holes—flow into the junction from electrodes with different voltages. When an electron meets a hole, it falls into a lower energy level, and releases energy in the form of a photon. The wavelength of the light emitted, and thus its color depends on the band gap energy of the materials forming the p-n junction. In silicon or germanium diodes, the electrons and holes recombine by a non-radiative transition, which produces no optical emission, because these are indirect band gap materials. The materials used for the LED have a direct band gap with energies corresponding to near-infrared, visible, or near-ultraviolet light. LED development began with infrared and red devices made with gallium arsenide. Advances in materials science have enabled making devices with ever-shorter wavelengths, emitting light in a variety of colors. LEDs are usually built on an n-type

substrate, with an electrode attached to the p-type layer deposited on its surface. P-type substrates, while less common, occur as well. Many commercial LEDs, especially GaN/InGaN, also use sapphire substrate. Most materials used for LED production have very high refractive indices. This means that much light will be reflected back into the material at the material/air surface interface. Thus, light extraction in LEDs is an important aspect of LED production, subject to much research and development.

Current bright blue LEDs are based on the wide band gap semiconductors GaN and InGaN. They can be added to existing red and green LEDs to produce the impression of white light, though white LEDs today rarely use this principle. The first blue LEDs using gallium nitride were made in 1971 by Jacques Pankove at RCA Laboratories. These devices had too little light output to be of practical use and research into gallium nitride devices slowed. In August 1989, Cree Inc. introduced the first commercially available blue LED based on the indirect bandgap semiconductor, silicon carbide. SiC LEDs had very low efficiency, no more than about 0.03%, but did emit in the blue portion of the visible light spectrum. In the late 1980s, key breakthroughs in GaN epitaxial growth and p-type doping ushered in the modern era of GaN-based optoelectronic devices. Building upon this foundation, in 1993 high-brightness blue LEDs were demonstrated. Efficiency (light energy produced vs.

electrical energy used) reached 10%. High-brightness blue LEDs invented by Shuji Nakamura of Nichia Corporation using gallium nitride revolutionized LED lighting, making high-power light sources practical. By the late 1990s, blue LEDs had become widely available. They have an active region consisting of one or more InGaN multiple quantum wells (MQWs) sandwiched between thicker layers of GaN, called cladding layers. By varying the relative InN-GaN fraction in the InGaN MQWs, the light emission can be varied from violet to amber. AlGaN aluminium gallium nitride of varying AlN fraction can be used to manufacture the cladding and MQWs layers for ultraviolet LEDs, but these devices have not yet reached the level of efficiency and technological maturity of the InGaN-GaN blue/green devices. If the active MQWs layers are GaN, instead of alloyed InGaN or AlGaN, the device will emit near-ultraviolet light with wavelengths around 350–370 nm. Green LEDs manufactured from the InGaN-GaN system are far more efficient and brighter than green LEDs produced with non-nitride material systems. With nitrides containing aluminium, most often AlGaN and AlGaInN, even shorter wavelengths are achievable. Ultraviolet LEDs in a range of wavelengths are becoming available on the market. Near-UV emitters at wavelengths around 375–395 nm are already cheap and often encountered, for example, as black light lamp replacements for inspection of anti-counterfeiting UV watermarks in some documents and paper currencies.

Shorter-wavelength diodes, while substantially more expensive, are commercially available for wavelengths down to 247 nm. As the photosensitivity of microorganisms approximately matches the absorption spectrum of DNA, with a peak at about 254 nm, UV LED emitting at 250–270 nm are to be expected in prospective disinfection and sterilization devices. Recent research has shown that commercially available UVA LEDs (365 nm) are already effective disinfection and sterilization devices. Deep-UV wavelengths were obtained using aluminium nitride (210 nm), boron nitride (215 nm) and diamond (235 nm).

Reference

1. Online resource, <http://en.wikipedia.org/wiki/Spectrometer>.
2. Online resource, <http://en.wikipedia.org/wiki/Monochromator>.
3. Online resource, <http://en.wikipedia.org/wiki/Photomultiplier>.
4. Online resource, http://en.wikipedia.org/wiki/Charge-coupled_device.
5. R. A. Stradling and P. C. Klipstein, *Growth and Characterisation of Semiconductors*, published by Hilger (1990).
6. S. Perkowitz, *Optical Characterization of Semiconductors: Infrared, Raman, and Photoluminescence Spectroscopy*, published by Academic Press (1993).
7. J. I. Pankove, *Optical Processes in Semiconductors*, Prentice-Hall, Inc. (1971).
8. G. D. Gilliland, *Mater. Sci. Eng.* **R18**, 99 (1997).

9. P. Y. Yu and M. Cardona, *Fundamentals of Semiconductors*, published by Springer (2001).
10. Friedrich W, Knipping P, von Laue M, *Interferenz-Erscheinungen bei Röntgenstrahlen* (1912).
11. von Laue M. "Concerning the detection of x-ray interferences" *Nobel Lectures, Physics 1901–1921* (1914).
12. Dana ES, Ford WE, *A Textbook of Mineralogy*, fourth edition. New York: John Wiley & Sons. pp. 28 (1932).
13. Online resource, http://en.wikipedia.org/wiki/Scanning_electron_microscope.
14. Gerald B. Stringfellow, *Organometallic Vapor-Phase Epitaxy: Theory and Practice* (2nd ed.), Academic Press (1999) (ISBN 0-12-673842-4).
15. R.S. Wagner and W.C. Ellis, *Applied Physics Letters* **4**, 89 (1964).
16. Guo, M.; Diao, P.; Cai, S.; *J. Sol. Sta. Chem.* **2005**, *178*, 1864.
17. M. Quirk and J. Serda, *Semiconductor Manufacturing Technology*, Prentice Hall (2000).
18. M. Birkholz "Crystal-field induced dipoles in heteropolar crystals – II. physical significance". *Z. Phys. B* 96 (3): 333–340 (1995).
19. S. Trolier-McKinstry "Chapter3: Crystal Chemistry of Piezoelectric Materials".
In A. Safari, E.K. Akdoğan. *Piezoelectric and Acoustic Materials for Transducer*

Applications. New York: Springer. (2008).

20. Sensor Sense: Piezoelectric Force Sensors. Machinedesign.com (2008-02-07).

21. Online resource, http://en.wikipedia.org/wiki/Quantum-confined_Stark_effect.

22. Online resource, http://en.wikipedia.org/wiki/Zinc_oxide.

23. R. Dahal, B. Pantha, J. Li, J. Y. Lin, and H. X. Jiang, *Appl. Phys. Lett.* **94**, 063505 (2009).

24. Online resource,

<http://www.tms.org/pubs/journals/jom/9709/steigerwald-9709.html>

25. Online resource, http://en.wikipedia.org/wiki/Light-emitting_diode.



Chapter 3

Tunable Photoluminescence and Photoconductivity in ZnO One-dimensional Nanostructures with a Second Below-gap Beam

3.1 Introduction

These decades, ZnO has been extensively studied due to its unique optical properties in the ultraviolet (UV) region as well as a large exciton binding energy of 60 meV, which holds the promise for producing efficient room-temperature exciton emitters and very low-threshold lasers.¹ Additionally, due to a large surface-to-volume ratio of the inherent nature, low-dimensional ZnO nanostructures have been found to exhibit several intriguing phenomena, which can be developed into many important applications, such as photodetectors,² gas sensors,³ biosensors,⁴ and even cosmetics.⁵ The emission spectra of ZnO crystals usually show two luminescence bands: the sharp UV emission near 380 nm, which is embedded of near band edge (NBE) recombination as well as phonon replicas, and the defect related emission, which is usually in the region of 450 – 600 nm.⁶ Due to lack of suitable experimental techniques, the study of defect related transition is rather limited, especially for nanomaterials. It has been demonstrated previously that dual beams induced optical quenching provides an excellent opportunity to probe the nature of defect transitions in semiconductors.^{7,8} In this work, we would show that dual beams optical quenching does occur in ZnO nanomaterials, which can serve as a convenient method

to reveal the defect characteristics. Based on both of the dual beams quenching of photoluminescence as well as photoconductivity, it is found that the defect transition responsible for the quenching effect arises from oxygen vacancies. In addition, from the size-dependent measurement, we further point out that the defects in charge of the optical quenching are dominated by oxygen vacancies located on surface. Finally, we studied the power-dependence of the PL quenching effect, which does confirm our interpretation.

3.2 Experiment

ZnO nanorods were grown on *a*-plane sapphire substrates via the vapour-liquid-solid (VLS) growth process,⁶ and ZnO nanoribbons were grown on a glass substrate via vapour-solid (VS) method as our previous report.⁹ To manipulate the diameter of ZnO nanorods, we coated Au film with different thicknesses onto different areas of a piece of sapphire substrate. After VLS growth process, ZnO nanorods with a larger diameter will be grown on the area with a thick Au film. Scanning electron microscope (SEM) images were recorded using a JEOL JSM 6500 system. Wavelength-dependence and time-dependence photoluminescence (PL) measurements were both performed at 12K using a Jobin Yvon SPEC-1403 spectral system working in the double-grating mode. The wavelength-dependence and time-dependence photoconductivity (PC) measurements were performed at 12K using

a Keithley 236 unit. The optical source of the first beam comes from a He-Cd laser with the wavelength of 325 nm. The second beam comes from a solid state laser with the wavelength of 532 nm or the varying wavelength dispersed from a xenon lamp by a Spectra-Pro 300i spectral system.

3.3 Results and Discussion

As shown in Fig. 3.1, three different sizes of ZnO nanorods have been grown. The ZnO nanorods form a well-organized hexagonal shape with diameters of (a) 300-350 nm, (b) 150-250 nm, and (c) 70-100 nm, and in Fig. 3.1 (d), nanoribbons were well grown on a glass substrate. First, we performed the PL measurement on the thin nanorods in Fig. 3.1 (c) and tested the effect of dual beams excitation in ZnO nanorods at 12K. The blue line in Fig. 3.2 (a) presents the PL spectrum of ZnO nanorods under a pumping source of 325 nm He-Cd laser with an estimated power density of 20 W/cm². It is well known that *as*-grown ZnO usually has unintentional n-type conductivity, and the donor energy level could locate up to 100 meV lower than the free exciton level (3.37 eV). Therefore, The UV emission locating near 380 nm (3.27 eV) can be reasonably attributed to donor-to-valence-band transition embedded LO phonon replicas, while the broad visible emission is due to the defect transitions.^{1,10,11} As presented with the red line in Fig. 3.2 (a), upon the excitation of the second beam from a 532 nm solid state laser with a power density of 250 W/cm²,

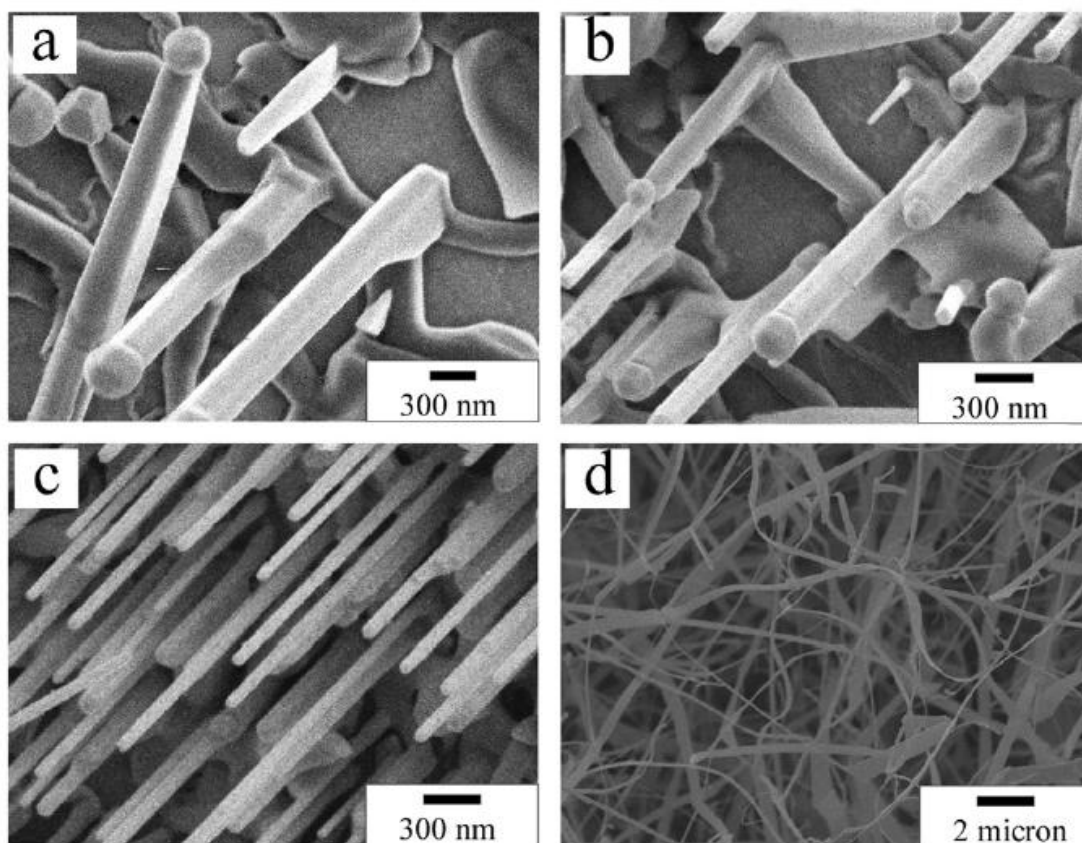


Fig. 3.1 Scanning electron microscopy images of ZnO nanorods with different diameters of (a) 300~350 nm, (b) 150~250 nm, and (c) 70~100 nm. The image of ZnO nanoribbons is shown in (d). One can notice the scale bars in (a) and (b) to tell the sizes of nanorods.

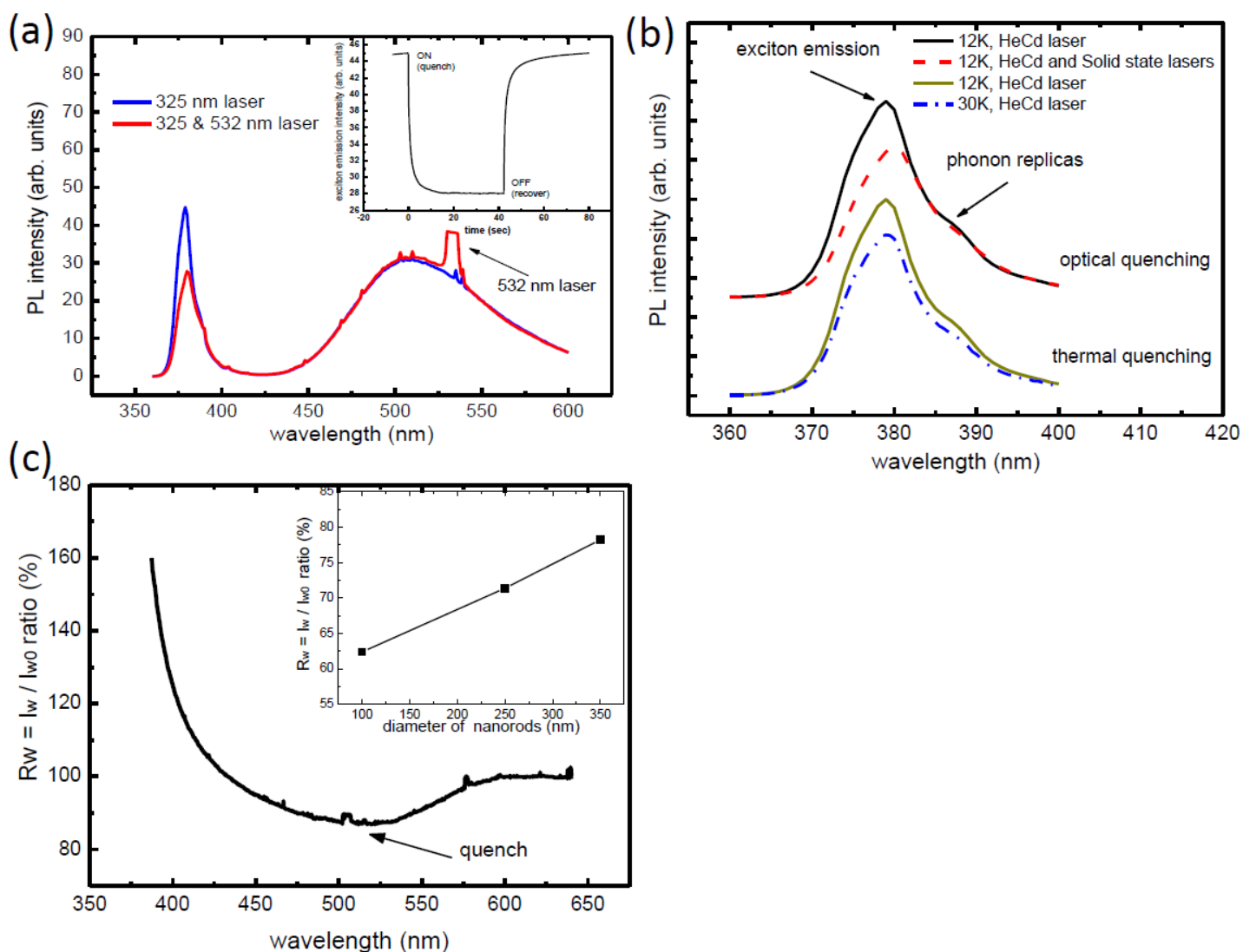


Fig. 3.2 (a) Photoluminescence spectra of thin ZnO nanorods with a 325 nm UV pumping source while the below-gap source with 532 nm keeps on/off at 12K. The inset shows the time evolution of band-edge emission as the second beam (532 nm) was switched on and off. (b) Comparison of the optical quenching and thermal quenching. (c) Spectral distribution of excitation and quenching of band-edge emission from ZnO nanorods at 12K. The inset shows the dependence between the R_w ratio and the diameter of ZnO nanorods.

we found that the NBE emission quenches while the defect emission almost remains the same intensity. We should note that in order to observe the PL quenching by the second beam, the intensity of first beam needs to be controlled to a weak level (20 W/cm^2) and the second beam should be relatively strong (250 W/cm^2) so that the influence of the second beam can be more apparent. The inset of Fig. 3.2 (a) shows the time-dependence variation of the NBE emission as switched on/off the 532 nm laser while the 325 nm laser keeps pumping continuously. Note that the intensity of the NBE emission can be quenched by up to 40 %. This intriguing phenomenon reveals that as we apply an additional optical energy onto the emitting sample, the intensity of emission is quenched, instead of enhancement. It is possible that the optical quenching may be caused by the thermal effect due to laser heating. As shown in Fig. 3.2 (b), we compared the quenching effects caused by the second beam of 532 nm laser and by a temperature controller. We can clearly see that if the sample is heated from 12K to 30K by the temperature controller, the NBE emission and the phonon replicas quench simultaneously.^{1,10,11} However, as the second beam applied on the sample while the temperature is kept at 12K, the NBE emission is quenched, but the intensity of phonon replicas remains unchanged. Since the phonon replica emission is due to the phonon releasing during NBE recombination process, the fact that the phonon replica band at higher temperature (30K) is weaker than that at lower

temperature (12K) could be expected. It is because at higher temperature, there already exist a large number of phonons in the lattice such that the phonon releasing rate should be restricted. On the other hand, as we apply the below-gap second beam without raising temperature, the result reveals that the rate of phonon releasing from NBE emission does not change, such that the phonon replica band remains the same due to the unchanged number of phonons in the lattice. This different behavior leads us to exclude the possibility that the observed optical quenching is caused by laser heating.

To further probe the characteristics of the quenching effect, we have performed dual beams photoluminescence excitation (PLE) measurement, which is a little bit different from the traditional PLE experiment. With the continuous pumping of 325 nm laser at 12K, the wavelength of the second beam was varied, and the wavelength of the emission for the detection was fixed at the NBE transition of 380 nm. The dual beams PLE technique shown here is very useful to probe the dominant defect transition responsible for the PL quenching. As shown in Fig. 3.2 (c), it describes the change of the NBE emission under the second light beam applied on the same spot with varying wavelength, where R_w is defined as $R_w = I_w / I_{w0}$, the ratio of the quenched PL intensity to the unquenched intensity. We can clearly see that the strongest quenching occurs as the second light beam is at 520 nm, which matches well with the

green-band defect emission as shown in Fig. 3.2 (a). This behavior provides an additional evidence showing that the quenching effect does arise from defect states, instead of laser heating. It is because the light beam used in this experiment comes from a xenon lamp dispersed by a monochromator which has the intensity much smaller than a laser beam. It is well known that deep-level defect centers are presumed to be the preferable channels of charge carrier recombination, which can inhibit NBE emission. In addition, the recombination activity of the defect centers strongly depends on their charged states.^{7,12,13} Due to the inherent nature of surface, there exist abundant defects, which may be responsible for our observation of the large optical quenching effect. If this is true, we will expect the strength of the effect should exhibit a strong dependence on the size of ZnO nanorods, since the surface-to-volume ratio varies with the size of nanostructures. We therefore have performed the dual-beams PL in three different sizes of ZnO nanorods. The inset of Fig. 3.2 (c) shows the quenching ratio as a function of the diameters of ZnO nanorods. It indicates that the thinner nanorods have a stronger quenching factor. This result implies that the defects responsible for the quenching effect may locate on the ZnO nanorod surface. Because the thinner nanorods have a larger surface-to-volume ratio, there exists more concentration of surface defect states,¹⁴ which can contribute to the optical quenching effect.

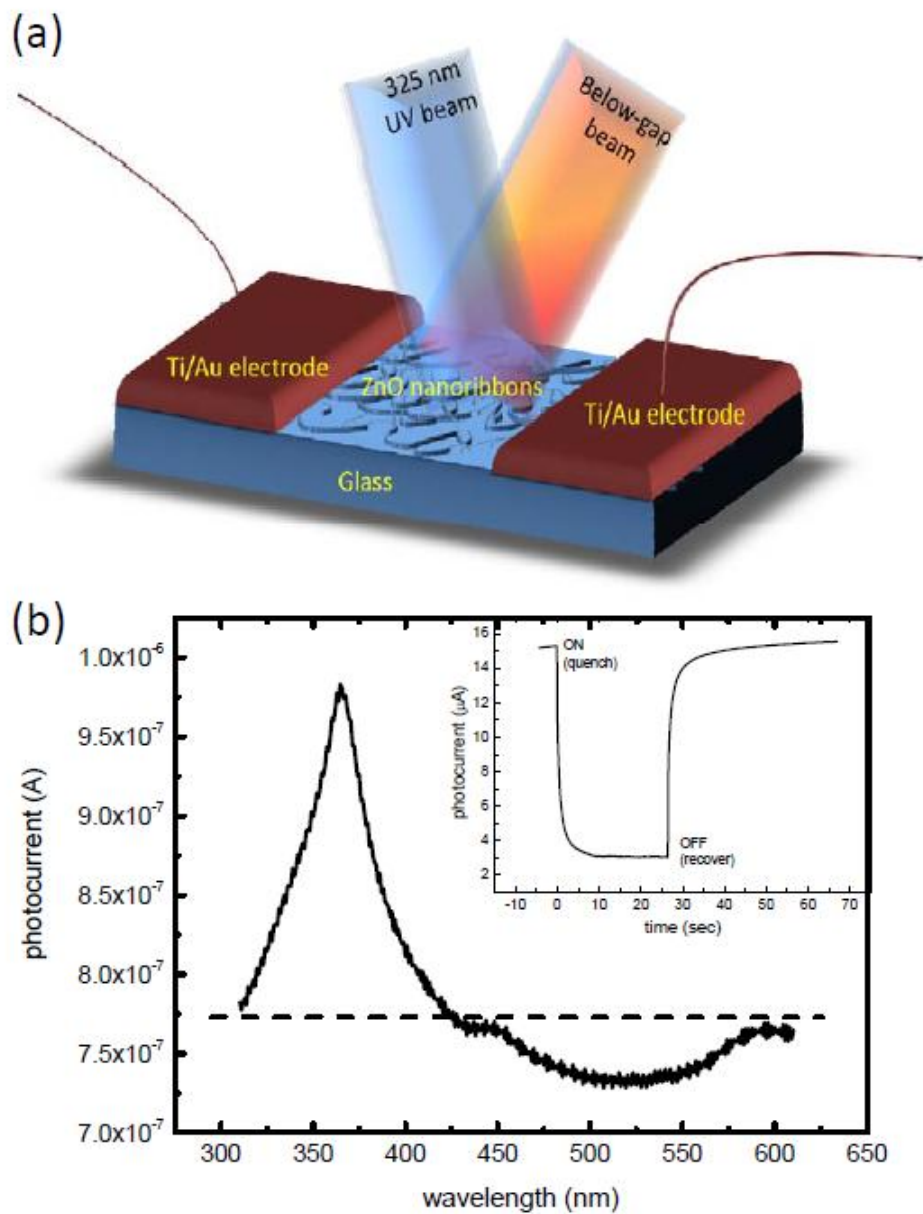


Fig. 3.3 (a) Scheme of the device profile to illustrate the experimental process of the quenching effect in ZnO nanoribbons. (b) Spectral distribution of excitation and quenching of the photocurrent in ZnO nanoribbons at 12K. The dashed line shows the constant current excited by 325 nm laser. The inset shows the time evolution of photocurrent as the second beam (532 nm) was switched on and off.

Since the below-gap beam provides a nonradiative path for the recombination of free carriers, it is expected that the photoconductivity of ZnO nanostructures would also be affected by the below-gap light.¹⁵ To prove this conjecture, we have performed the dual-beams photoconductivity measurement. As shown in Fig. 3.3 (a), two electrodes of Ti/Au (1:10) were sputtered onto the sample of ZnO nanoribbons, and a bias of 5V was applied to the electrodes. Unlike for the case of vertical aligned nanorods, ZnO nanoribbons used in this experiment can ensure the conduction path through ZnO nanomaterials for the photoexcited carriers. The inset of Fig. 3.3 (b) shows the time-dependence variation of the current through ZnO nanoribbons as switched on/off the 532 nm laser while the 325 nm laser keeps pumping continuously. The PC quenching effect was observed as 532 nm laser switched on, and the PC recovered as the 532 nm laser switched off. We have also performed the experiment with 325 nm laser kept pumping continuously, and recorded the PC while varying the wavelength of the second light beam as shown in Fig. 3.3 (b). Similar to the result of PL measurement, a quenching effect is observed for the PC under the excitation of the second light beam, and the quenching peak also occurs at 520 nm near the defect emission.

Based on the above results, we now attempt to explain the quenching effect. Since both PL and PC in nanostructures are quenched under the illumination of the

second light beam, it is readily figured out that the below-gap beam creates an additional recombination path and decreases the population of the charge carriers in the conduction band edge. According to our measurement, the highest quenching efficiency is located near the green band of defect emission, which has been attributed to oxygen vacancies related transition.^{12,13,16,17} We therefore suggest that the defect of oxygen vacancies may play an important role in the quenching mechanism. In ZnO there exist three types of oxygen vacancies: the neutral state relative to the lattice state V_O^0 , which captures two electrons, the singly ionized V_O^+ state with one electron, and the doubly positively charged V_O^{++} state that does not trap any electron. As shown in the previous reports, electron paramagnetic resonance (EPR) study is very useful to understand the properties of oxygen vacancies.^{12,13,16,18} It is found that the EPR signal of V_O^+ is very photosensitive to visible light, because by absorbing photogenerated electrons V_O^{++} centers can be converted to the paramagnetic V_O^+ state. As shown in Fig. 3.4 (a), we propose a model which is self-consistent with our result, and it can clearly illustrate the quenching effect quite well. The below gap illumination is to excite electrons from deep level defects to the conduction band. The excited electron is captured by V_O^{++} at once and convert V_O^{++} to V_O^+ , which can be expressed as the formula,



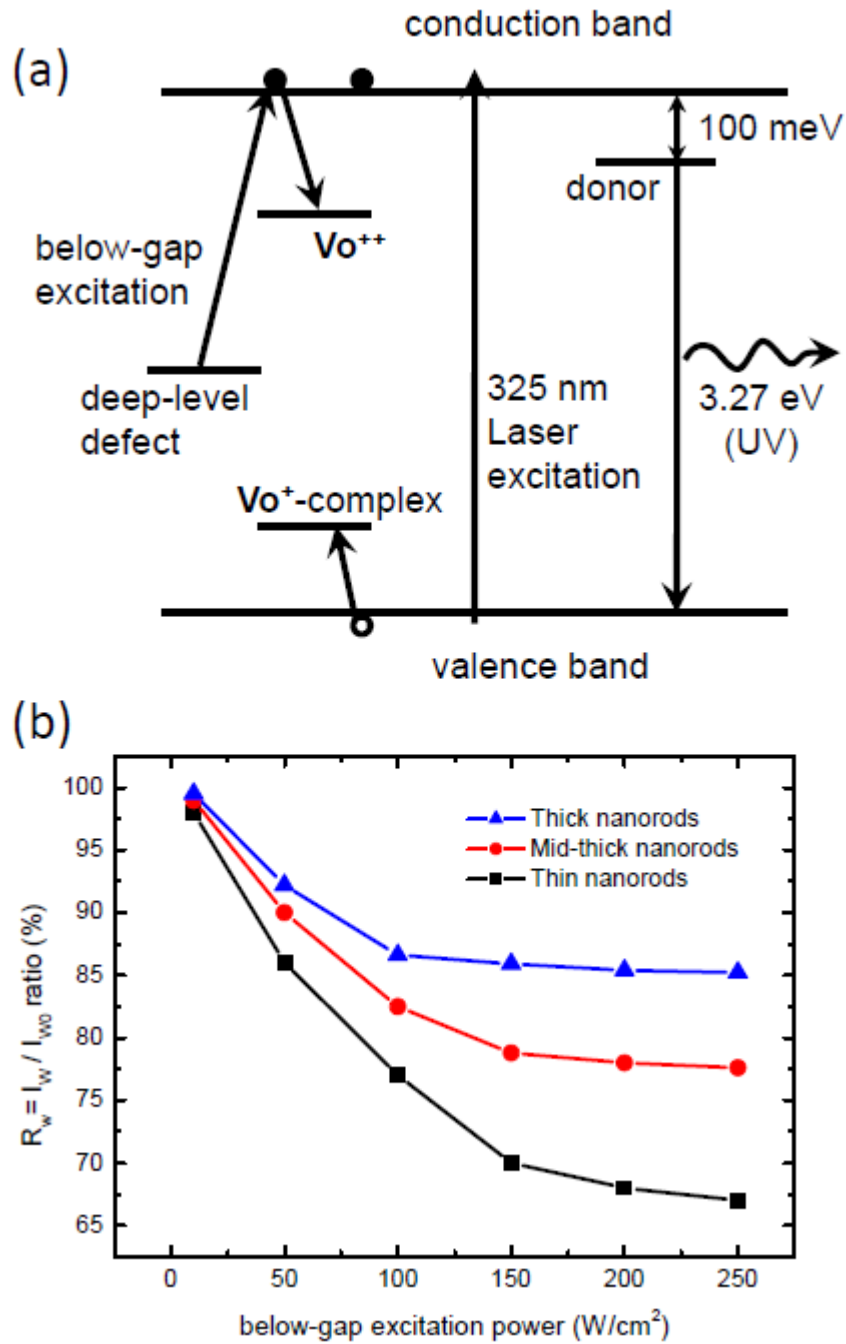


Fig. 3.4 (a) Illustration to the carrier transitions which can explain the quenching effect of the NBE emission by the below-gap illumination. (b) Quenching ratios as a function of below-gap excitation power density in three different sizes.

Based on the previous report, Vo^+ is capable of absorbing a hole.¹⁶ Therefore, the photogenerated holes by UV illumination may be captured by Vo^+ and convert Vo^+ to Vo^{++} , which will reduce the recombination rate of the transition from donor impurity to the valence band. In addition, the below-gap-quenching of UV emission in our samples does not lead to an enhancement of the green emission. Such behavior could be referred to the fact that the below-gap excitation induces nonradiative states. There exists another type of singly ionized oxygen vacancy, Vo^+ -complex state, which unlike the isolated Vo^+ is not a green luminescence center and may act as a nonradiative center. We suggest that most of Vo^+ centers converted from Vo^{++} centers form into complex states, which do not take part in the green emission but merely absorb holes from the valence band. Since the Fermi level passes below the $\text{Vo}^+/\text{Vo}^{++}$ energy level and all oxygen vacancies located in the surface depletion region are in the diamagnetic Vo^{++} state,¹³ the optical quenching effect can then be very pronounced in thinner nanorods. On the other hand, in addition to oxygen vacancies, other surface traps may be also possible responsible for the optical quenching phenomenon, such as adsorption of oxygen molecules. In previous investigation,¹⁷ oxygen molecules adsorbed on the surface of ZnO nanostructures in O^{2-} states could trap holes from valence band to become O^- states and then trap electrons from conduction band, or vice versa. The trapped electrons and holes recombine at the

surface through non-radiative process may be seen as an additional path responsible for the optical quenching. However, we do not take this behavior into consideration because the dual beams experiments were performed under low temperature (12K) and in vacuum condition, such that the oxygen adsorption could be neglected.

Finally, we have performed the power-dependent optical quenching in three different sizes of ZnO nanorods. Figure 3.4 (b) shows the value of R_w as a function of the below-gap excitation power density. With the increasing power of below-gap excitation, R_w decreases and gets saturated gradually. It is worth noting that R_w saturates at a higher below-gap excitation power in thinner nanorods. This is due to the fact that a higher surface-to-volume ratio in thinner nanorods have a larger number of oxygen vacancies and the saturation of the defect effect needs a higher pumping intensity. This result again supports our interpretation that the optical quenching arises from surface-related defect states.

3.4 Conclusion

In conclusion, dual beams excitation of PL and PC have been used to investigate the influence of defects on the optical properties of ZnO nanostructures. It is found that the second below-gap excitation can significantly quench the NBE emission and photocurrent. By varying the photon energy of below-gap excitation, the important information for the understanding of defect characteristics can be revealed, which is

difficult to achieve for most available techniques. In view of the usefulness obtained by dual beams excitation of PL and PC in nanomaterials as shown here, we point out that these methods can be applied to many other material systems for the further advance of nanoscale research.

References

1. Ü. Özgür, Ya. I. Alivov, C. Liu, A. Teke, M. A. Reshchikov, S. Doğan, V. Avrutin, S.-J. Cho, and H. Morkoç, *J. Appl. Phys.* **98**, 041301 (2005).
2. C. Soci, A. Zhang, B. Xiang, S. A. Dayeh, D. P. R. Aplin, J. Park, X. Y. Bao, Y. H. Lo, and D. Wang, *Nano Lett.* **7**, 1003 (2007).
3. Q. Wan, Q. H. Li, Y. J. Chen, T. H. Wang, X. L. He, J. P. Li, and C. L. Lin, *Appl. Phys. Lett.* **84**, 3654 (2004).
4. F. Zhanga, X. Wanga, S. Aia, Z. Suna, Q. Wana, Z. Zhub, Y. Xiana, L. Jin, and K. Yamamoto, *Analytica Chimica Acta* **519**, 155 (2004).
5. A. S. Dussert, E. Gooris, and J. Hemmerle, *Int. J. Cosmetic Sci.* **19**, 119 (1997).
6. H. Y. Shih, T. T. Chen, Y. C. Chen, T. H. Lin, L. W. Chang, and Y. F. Chen, *Appl. Phys. Lett.* **94**, 021908 (2009).
7. S. Kurbanov, G. Panin, T. W. Kang, and T. W. Kim, *Jpn. J. Appl. Phys.* **47**, 3760 (2008).
8. I. J. Chen, T. T. Chen, and Y. F. Chen, *Appl. Phys. Lett.* **89**, 142113 (1996).

9. H. K. Fu, C. L. Cheng, C. H. Wang, T. Y. Lin, and Y. F. Chen, *Adv. Funct. Mater.* **19**, 3471 (2009).
10. W. Shan, W. Walukiewicz, J. W. Ager III, K. M. Yu, H. B. Yuan, H. P. Xin, G. Cantwell, and J. J. Song, *Appl. Phys. Lett.* **86**, 191911 (2005).
11. T. Voss, C. Bekeny, L. Wischmeier, H. Gafsi, S. Börner, W. Schade, A. C. Mofor, A. Bakin, and A. Waag, *Appl. Phys. Lett.* **89**, 182107 (2006).
12. K. Vanheusden, C. H. Seager, W. L. Warren, D. R. Tallant, and J. A. Voigt, *Appl. Phys. Lett.* **68**, 403 (1996).
13. K. Vanheusden, W. L. Warren, C. H. Seager, D. R. Tallant, J. A. Voigt, and B. E. Gnade, *J. Appl. Phys.* **79**, 7983 (1996).
14. I. Shalish, H. Temkin, and V. Narayanamurti, *Phys. Rev. B* **69**, 245401 (2004)
15. T. Y. Lin, H. C. Yang, and Y. F. Chen, *J. Appl. Phys.* **87**, 3404 (2000).
16. K. Vanheusden, C. H. Seager, W. L. Warren, D. R. Tallant, J. Caruso, M. J. Hampden-Smith, and T. T. Kostas, *J. Lumin.* **75**, 11 (1997).
17. A van Dijken, E. A. Meulenkaamp, D. Vanmaekelbergh, and A. Meijerink, *J. Lumin.* **87-89**, 454 (2000).
18. L. S. Vlasenko, *Physica B* **404**, 4774 (2009).

Chapter 4

Symmetrically Tunable Optical Properties of InGaN/GaN Multiple Quantum Disks by an External Stress

4.1 Introduction

III-nitride semiconductors have been recognized as an important material class for many optoelectronic devices, such as light-emitting devices (LEDs) and laser diodes (LDs).¹ Especially by changing the relative composition of the constituent elements, such as In and Ga, the wavelengths of emission could cover from ultraviolet to infrared radiation. According to the previous studies,^{2,3} it has been shown that many physical properties of the materials with wurtzite structure may depend on the crystal orientation. Investigations upon the dependence of physical properties involving crystal orientation can not only establish the fundamental understanding of nitride-based materials, but also provide an alternative solution to improve the properties of the associated devices. For example, it will be a great advantage if one can choose a particular orientation which has a small effective mass and high optical gain as predicted theoretically in the previous reports.³ However, rare experimental works have been devoted to the influence of crystal orientation on the physical properties of nitride-based materials.^{4,5} In this work, we have investigated the orientational dependence of the effect of an external stress on the optical properties in the composite consisting of polydimethylsiloxane (PDMS) and InGaN/GaN multiple

quantum disks (MQDs). Because the MQDs were vertically aligned, it would be an advantage for us to apply an external stress on them in various orientation. It is found that both photoluminescence (PL) and Raman scattering spectra can be manipulated after an external stress is applied. Especially, the shift amount of PL and Raman scattering spectra reveals a dependence on the crystal orientation with a sixfold symmetry. Our results shown here are quite useful for understanding the optical properties of nitride semiconductors and provide an alternative route to improve the performance of nitride-based devices, which can be used to extend the applications of the devices based on nitride semiconductors, such as stress detectors and optical modulators.^{6,7}

4.2 Experiment

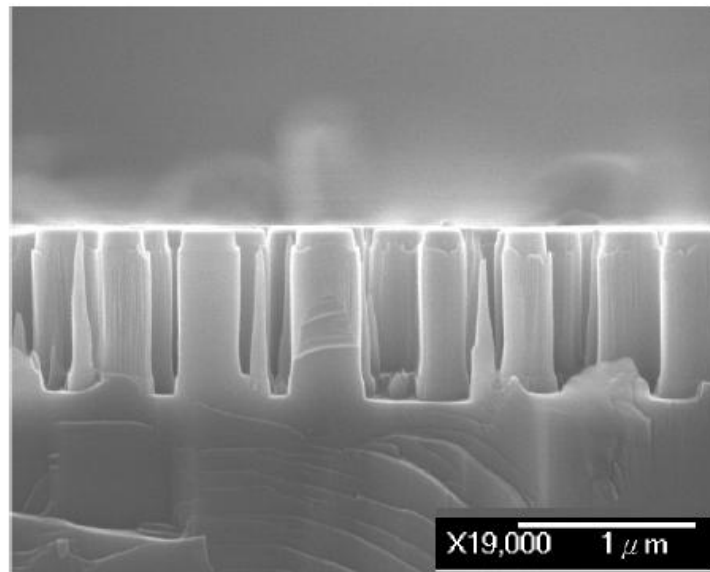
The sample studied in this work was prepared by metal-organic chemical vapor deposition (MOCVD). A series of multiple quantum wells (MQWs) containing 10 periods of 2 nm $\text{In}_{0.22}\text{Ga}_{0.78}\text{N}$ wells and 9 nm GaN barriers were grown on a (0001) sapphire substrate. The MQWs were sandwiched between a 2 μm n -GaN layer on the sapphire and a 0.5 μm p -GaN capping layer, which is the typical structure for LEDs. The sample was then vertically etched into nanorods (NRs) by the method of inductively coupled plasma reactive-ion etching (ICP-RIE). After the etching process, the InGaN/GaN MQWs will turn into MQDs embedded in the middle of the NRs. The

top and side views of the sample were recorded by scanning electron microscope (SEM) as shown in Fig. 4.1 (a). The NRs were estimated to have an average diameter of 300 nm and an average length of 1.0 μm , respectively. Figure 4.1 (b) illustrates the details of the optical measurements. In order to investigate the influence on the optical properties of the MQDs under an external stress, the sample was fixed on a flat stage and covered with one end of a rectangular PDMS elastic film. The other end of the elastic film was fixed on a tunable linear stage (TLS), such that we can transversally stretch the top of the NRs through the elastic film by tuning the TLS. The stretching force of the PDMS film can be estimated by the formula:

$$F = \frac{EA_0\Delta L}{L_0}, \quad (4.1)$$

where E , A_0 , ΔL , and L_0 are Young's modulus, original cross-sectional area, amount of the length changes, and original length of the PDMS film, respectively.⁸ In this work, the SEM images were recorded by a JEOL JSM 6500 system. Micro-photoluminescence ($\mu\text{-PL}$) measurements were taken by a Jobin Yvon TRIAX-320 spectral system with an OLYMPUS microscope, and the optical source was provided by a solid state laser working at 374 nm. Micro-Raman ($\mu\text{-Raman}$) scattering spectra were performed by a Jobin Yvon SPEC-T64000 spectral system with an OLYMPUS microscope, and the optical source is provided by an Ar^+ laser working at 514 nm. It is worth noting that the internal strain in MQWs due to lattice

(a)



(b)

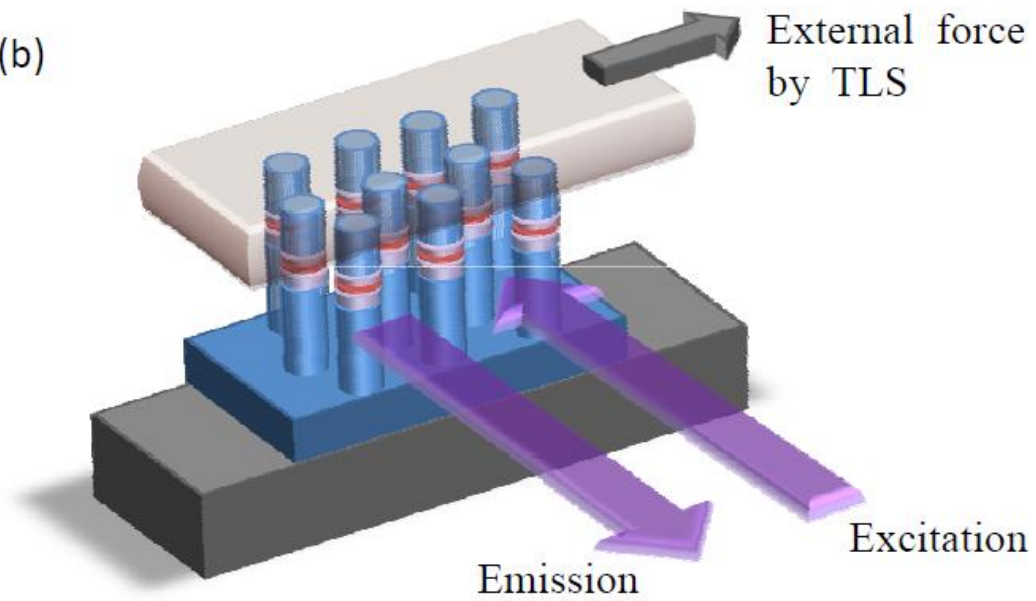


Fig. 4.1 (a) Side view of the etched nanorods recorded by the scanning electron microscope (SEM). (b) Illustration of the details of the optical measurements.

mismatch has been relaxed after the etching process. If there exists a built-in strain initially in the InGaN/GaN MQWs, a high excitation power could cause a blue-shift in the PL spectra of InGaN/GaN MQWs due to the screening effect by photoexcited electron-hole pairs as described in our previous report.⁹ However, we did not see any visible change in the peak position of the PL spectra from MQDs when we change the excitation power density (not shown here).¹⁰ Thus, the influence of the excitation power density on the PL peak position could be excluded in this work.

4.3 Results and Discussion

Figure 4.2 (a) shows the PL spectra of the side emission from MQDs under different external forces toward the a -axis. We can clearly see that when we increase the external stress, the PL intensity decreases, and the peak position reveals a red-shift. Furthermore, as shown in Fig. 4.2 (b), when we stretch the elastic film toward opposite directions, the amount of red-shift is symmetric about the zero point, and the obtained data are reproducible. This intriguing red-shift of the emission spectra in bent nanowires has been investigated in other materials with wurtzite structure, such as ZnO,^{11,12} which can be understood as follows. When we transversally stretch the top of the MQD-NRs through the elastic film by tuning the TLS, the NRs are bent due to the external force. The lattice on the convex side of the bent NRs is extended, and that on the concave side is compressed. According to the previous reports,^{13,14} it is

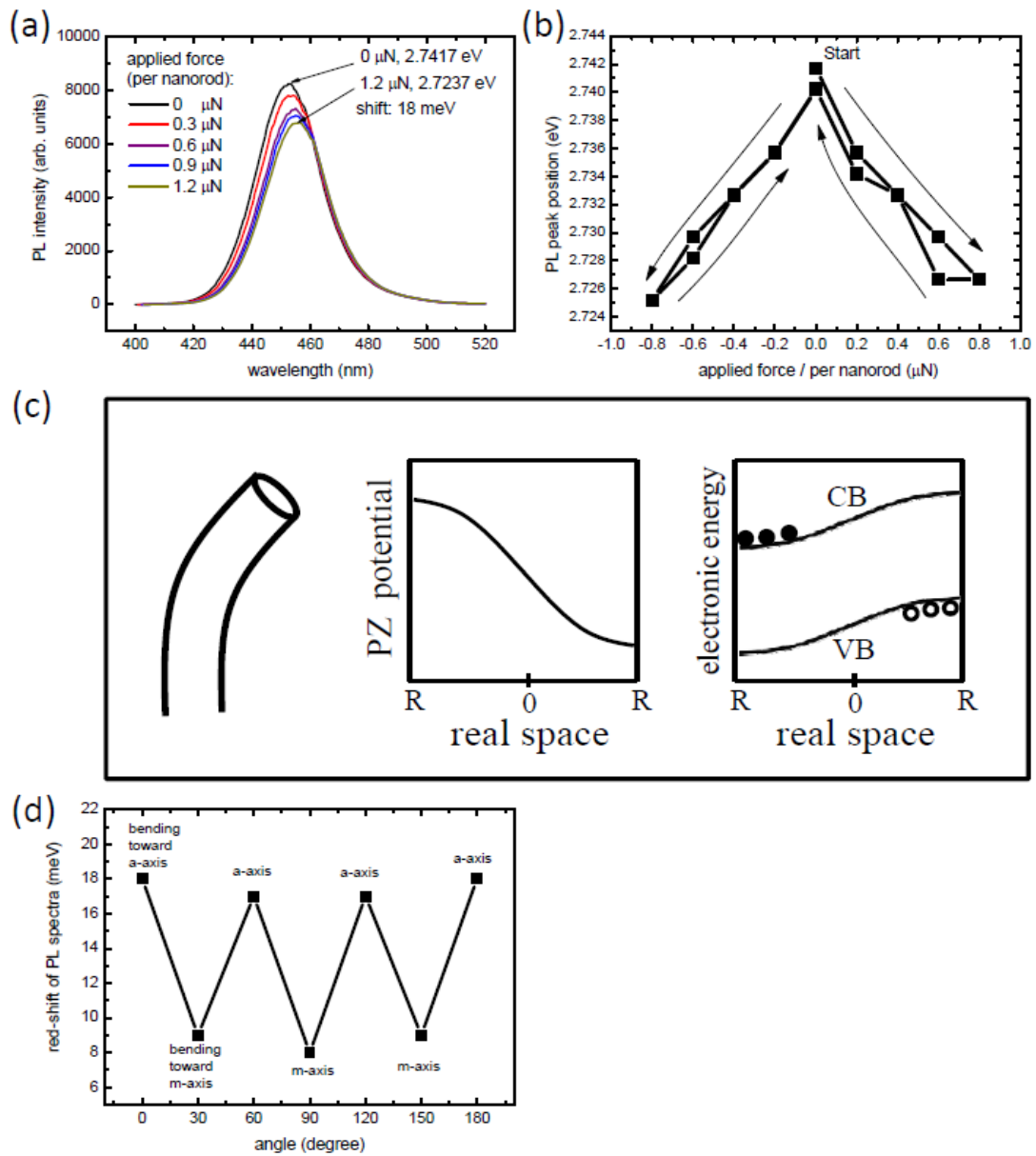


Fig. 4.2 (a) Photoluminescence (PL) spectra of the multiple quantum disks with different external force applied by the tunable linear stage (TLS). (b) Peak position of the PL spectra with different external force applied by the TLS. (c) Illustration of the piezoelectric potential and the electronic band structure in the nanorods. (d) The red-shift amount of the photoluminescence spectra as a function of the cutting angle of the sample.

known that there exists a strong piezoelectricity in the wurtzite structure of nitride semiconductors. More precisely, as the NRs are bent, the piezoelectric field will increase the potential at the extended side and lower the potential at the compressed side as shown in Fig. 4.2 (c).^{13,14} As a result, the photoexcited electrons and holes would be spatially separated to the opposite sides of the NRs. Once the energy bands are tilted, the recombination energy of the electron-hole pairs in NRs would be reduced due to the quantum confined Stark effect (QCSE).⁹ In addition, the recombination rate of electron-hole pairs would be reduced due to the lower factor of wave function overlapping caused by the spatial separation. Thus, the red-shift of peak position and the quenching of emission intensity in the PL spectra shown in Figs. 4.2 (a) and (b) could be reasonably explained.

Since many physical properties may depend on the crystal orientation,²⁻⁵ we further expect that the amount of stress-induced shift in emission spectra may be different if we change the stretching direction. To confirm our prediction, we had cut the sample along different orientations and repeated the PL measurements. Quite interestingly, as shown in Fig. 4.2 (d), under the same external force of the TLS (1.2 μN per NR), the amounts of red-shift in the PL spectra indeed reveal high dependence on the stretching orientations. We can clearly see that there exists a period of 60° in the shift amount as a function of the orientation angle. More precisely, the most and

least amount of red-shift occurs as the sample was stretched along a -axis ($[2 -1 -1 0]$) and m -axis ($[0 1 -1 0]$), respectively.

Let us now give an explanation for the sixfold anisotropic emission spectra as the NRs were bent along different orientations. There exist two main effects could change the excitonic recombination energy in our experiment. Firstly, the bending of NRs causes a red-shift of the emission peak position due to the piezoelectric potential associated with the QCSE as we discussed above. Secondly, according to the previous report,² the band structure in k -space of nitride semiconductors with C_6^v symmetry reveals a dependence on the crystal orientation. The result of the calculation by Hao et al. indicates that the transition energy between conduction band and heavy-hole band, which dominates the emission in nitride-based quantum wells, is larger in a -axis than that in m -axis. From the microscopic viewpoint, the number of ions per unit length in m -axis is greater than that along a -axis by a factor of 10:9. Therefore, the ground energy level in m -axis is lower than that in a -axis due to the larger energy levels splitting. The maximum and minimum peak energies have been observed in the a -axis and m -axis orientation.^{4,5} For our sample, the photo-excited carriers are confined in c -axis by the barriers of MQDs. Furthermore, when we bend the NRs toward m -axis, the carriers would also be confined in this axis by the potential arising from the piezoelectric effect. As a result, the carriers are relatively free to move along a -axis,

which have a higher recombination energy than that along m -axis. On the other hand, we would get a lower recombination energy if the NRs are bent toward a -axis, because the carriers are relatively free along m -axis. After summarizing the two effects, we can realize that without an external stress on the lattice, both effects are not revealed; once the NRs are bent toward m -axis, the higher transition energy due to the orientation-dependence could slightly cancel the red-shift caused by QCSE. By the same token, we can contrarily observe more red-shift in PL spectra as the NRs are bent toward a -axis due to the similar physical concept. Hence, the emission energy revealing a dependence of crystal orientation could be well explained.

To further investigate the influence of the external stress on the optical properties of NRs, we have performed micro-Raman (μ -Raman) scattering measurements and estimated the full width at half maximum (FWHM) of the spectra under different external force toward the a -axis as shown in Figs. 4.3 (a) and (b). The spectrum located near 732 cm^{-1} can be assigned to InGaN $A_1(\text{LO})$ mode.⁹ We can obviously see that the signal of Raman scattering spectrum is broadened and reveals a low-energy shift as the external force is applied. This intriguing behavior can be understood by the following explanation. In the bent NRs, compressive and tensile stresses of the lattice would shift the phonon peak to a higher and a lower wavenumber, respectively. Thus, for an ideal case, the NRs are expected to experience simultaneous compressive

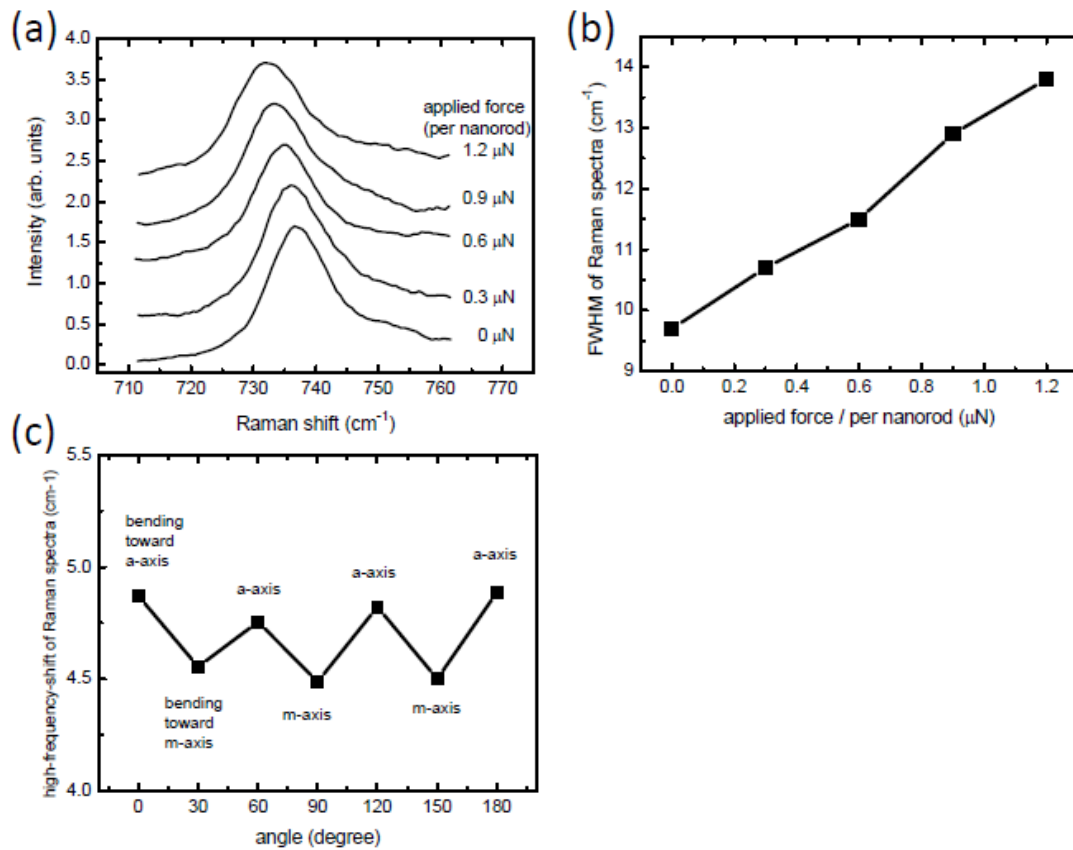


Fig. 4.3 (a) Raman scattering spectra of the multiple quantum disks with different external force applied by the tunable linear stage (TLS). (b) Full width at half maximum of the Raman scattering spectra as a function of the external force applied by the TLS. (c) The low-frequency-shift amount of the Raman scattering spectra as a function of the cutting angle of the sample.

strain on the concave side of the curvature and tensile strain on the convex side, while the central area is free of strain. So that the Raman scattering peak of the bent NRs should be symmetrically broadened with no shift of peak position.⁶ However, according to the previous reports,^{6,11,15} the convex part of the NRs would suffer more deformation than the concave part and result in tensile strain dominance. In our result, the $A_1(\text{LO})$ mode shifts toward lower wavenumbers, revealing the domination of tensile stress under the bending effect. The behaviors of peak shift and broadening in Raman scattering spectra are consistent with the results obtained from other nanostructures with wurtzite (C_6^v) symmetry, such as InP nanowires,¹⁵ ZnO nanowires,¹¹ and GaN plates.⁶

Similar to the PL spectra, it could be expected that the shift amount of Raman scattering spectra may also depend on the bending orientation. Indeed, the result meets our prediction as shown in Fig. 4.3 (c). We can see that when the NRs were bent toward m -axis, the amount of red-shift of Raman scattering spectra is less than that of m -axis. According to the discussion of microscopic viewpoint for PL spectra, the number of ions per unit length in the m -axis is greater than that along the a -axis by a factor of 10:9.⁴ Therefore, it is harder to bend the NRs toward m -axis than a -axis, and a lower strain would arise in the m -axis when the NRs suffer from a constant force. The net strain of MQDs can be estimated by the formula:¹⁰

$$\varepsilon = \frac{\Delta\omega}{2\left(a - b\frac{C_{13}}{C_{33}}\right)}, \quad (4.2)$$

where a and b are phonon deformation potentials, and C_{13} and C_{33} are elastic constants, respectively. According to Eq. (4.2), the average strains are estimated to be 0.78 % and 0.83 % when the force of 1.2 μN is applied by the TLS along m -axis and a -axis, respectively, where the deformation potentials a , b and the elastic constants C_{13} , C_{33} were estimated by the extrapolation of the data for GaN and InN.¹⁶ Thus, the Raman scattering anisotropy about the c -axis of the MQDs could be well understood.

Finally, it is worth emphasizing here that the changes of physical properties induced by an external stress are very attractive for many applications, such as stress detectors and optical modulators.^{6,7} Therefore, our study may also be useful to extend the applications of nitride based devices.

4.4 Conclusion

In conclusion, we have investigated the influences of an external stress on the optical properties of InGaN/GaN MQDs with wurtzite (C_6^v) symmetry. The PL spectrum of MQDs reveals a red-shift as they are bent by an external force. This can be explained by the QCSE due to the piezoelectric field caused by the strain. In addition, the $A_1(\text{LO})$ mode of Raman scattering spectrum is broadened and has a low-energy shift in the bent NRs. We point out that there exists a compressive strain on the concave side and a tensile strain on the convex side, and the convex part of the

MQW-NRs would suffer more deformation than the concave part. Quite interestingly, we have found that the amount of the red-shift in PL and Raman scattering spectra depends on the bending orientation. When the NRs are bent toward a -axis, the shift amounts of PL and Raman scattering spectra are more than those toward m -axis. This difference can be well interpreted by the nature of hexagonal lattice having a sixfold symmetry. Our results shown here could be quite useful for the understanding of the optical properties of nitride semiconductors and provide an alternative route to optimize and extend the application of nitride-based devices.

Reference

1. S. Nakamura, S. J. Pearton, and G. Fasol, *The blue laser diode* (Springer, Berlin, 2000).
2. G. -D. Hao, Y. H. Chen, and Y. F. Hao, *Appl. Phys. Lett.* **93**, 151111 (2008).
3. A. Niwa, T. Ohtoshi, and T. Kuroda, *Appl. Phys. Lett.* **70**, 2159 (1997).
4. T. N. Oder, J. Y. Lin, and H. X. Jiang, *Appl. Phys. Lett.* **79**, 12 (2001).
5. H. J. Chang, C. H. Chen, L. Y. Huang, Y. F. Chen, and T. Y. Lin, *Appl. Phys. Lett.* **86**, 011924 (2005).
6. J. Kim, K. Baik, C. Park, S. Cho, S. J. Pearton, and F. Ren, *phys. stat. sol. (a)* **203**, 2393 (2006).
7. P. D. Greene, U. S. Patent, 5017974 (1991).

8. J.E. Mark, *Polymer Data Handbook* (Oxford University Press, Oxford, 2009).
9. T. Y. Lin, *Appl. Phys. Lett.* **82**, 880 (2003).
10. H. J. Chang, Y. P. Hsieh, T. T. Chen, Y. F. Chen, C. -T. Liang, T. Y. Lin, S. C. Tseng, and L. C. Chen, *Opt. Exp.* **15**, 9357 (2007).
11. B. Yan, R. Chen, W. Zhou, J. Zhang, H. Sun, H. Gong, and T. Yu, *Nanotechnology* **21**, 445706 (2010).
12. X. Han, L. Kou, X. Lang, J. Xia, N. Wang, R. Qin, J. Lu, J. Xu, Z. Liao, X. Zhang, X. Shan, X. Song, J. Gao, W. Guo, and D. Yu, *Adv. Mater.* **21**, 4937 (2009).
13. Y. Gao and Z. L. Wang, *Nano Lett.* **7**, 2499 (2007).
14. Z. Z. Shao, L. Y. Wen, D. M. Wu, X. F. Wang, X. A. Zhang, and S. L. Chang, *J. Phys. D: Appl. Phys.* **43**, 245403 (2010).
15. J. Chen, G. Conache, M. -E. Pistol, S. M. Gray, M. T. Borgström, H. Xu, H. Q. Xu, L. Samuelson, and U. Håkanson, *Nano Lett.* **10**, 1280 (2010).
16. A. G. Kontos, Y. S. Raptis, N. T. Pelekanos, A. Georgakilas, E. Bellet-Amalric, D. Jalabert, *Phys. Rev. B*, **72**, 155336 (2005).

Chapter 5

Light-emitting Devices with Tunable Color from ZnO Nanorods Grown on InGaN/GaN Multiple Quantum Wells

5.1 Introduction

ZnO and III-nitrides have been widely investigated in the field of optoelectronics for several decades.¹⁻⁶ For example, InGaN/GaN multiple quantum wells (MQWs) have been generally adopted for commercial high-efficiency LEDs. By changing the relative composition of indium (In) and gallium (Ga), the MQWs can emit wavelengths covering from ultraviolet to infrared radiation. Also, ZnO nanostructures have been widely investigated and applied in several optoelectronic devices because of their wide bandgap and high exciton binding energy (60 meV).^{3,4} In addition, the fabrication of ZnO nanostructures has several flexible options in growth methods with low cost. Nowadays, low-dimensional materials have attracted great attention because of the quite different physical behaviors from their bulk structures. One of the unique properties in low-dimensional nanostructured materials is the strongly anisotropic physical properties. For instance, it has been found that the near-band-edge (NBE) emission from aligned ZnO nanorods (NRs) is strongly polarized with the electric field along the *c*-axis of ZnO crystal.⁵ On the other hand, the side emission from the InGaN/GaN MQWs grown on (0001) sapphire substrates is found to be highly polarized with the electric field in the plane of the MQWs.⁶ It is known that an

optoelectric device consisting of different materials with distinct properties can exhibit quite unusual behaviors through the coupling between the consistent elements.⁷ For instance, if a LED can be designed to have dual emissions with different polarizations, one can choose the emitted wavelength by rotating a polarizer or even by modulating the voltage of a liquid crystal cell.⁷ It would bring us advantages in many practical applications, such as optical modulators,⁸ color selectors,⁹ displays,⁷ and optical communications.¹⁰ Here, we introduced an intelligently designed LED based on the composite consisting of ZnO NRs and InGaN/GaN MQWs. In conventional MQW-based LEDs, carrier overflow is usually prohibited, because if it occurs the electrical energy may be converted into undesired emission. However, in this work, although the electron overflow is prohibited by an electron blocking layer, holes are intentionally led to overflow into the ZnO region to arise a second emission. One more point should be mentioned is that in conventional GaN-based LEDs, the n-GaN was grown before MQWs, because the n-GaN can be grown with higher crystallographic and morphological qualities than p-GaN. In this work, we adopted an inverted LED structure employing a n-ZnO NRs layer grown after the MQWs layer, because the growth temperature of n-ZnO is significantly lower than that required for GaN growth in metal-organic chemical vapor deposition (MOCVD), and this inverted structure is easier for us to grow the ZnO NRs layer,

which plays an important role in this device. The inverted structure of ZnO/GaN based LED has been demonstrated to perform quite well in the previous report.¹¹ According to our design, it is found that the composite consisting of ZnO NRs and InGaN/GaN MQWs becomes an intriguing LED with dual emissions, in which the relative intensity between the emissions can be manipulated by their polarizations. The underlying mechanism can be well interpreted by the optical anisotropy due to the inherent nature of geometric structures of nanomaterials.

5.2 Experiment

The studied InGaN/GaN MQWs were prepared by MOCVD. First, a 2.5 μm p-GaN layer and a 10 nm p-AlGaN electron-blocking layer were deposited on a (0001) sapphire substrate, and then an intrinsic series containing 5 periods of 2 nm $\text{In}_{0.22}\text{Ga}_{0.78}\text{N}$ wells and 5 nm GaN barriers were grown. ZnO NRs were grown on the top surface of MQWs via hydrothermal method as described in the previous report.¹² A small area of InGaN/GaN MQWs was etched to the p-GaN layer, and an indium (In) drop was deposited on p-GaN by a heated iron tip to serve as the p-electrode. The diameter of the indium drop is estimated to be 0.5 mm under an optical microscope (OM). Since indium drops are commonly used for quick-tests of commercial GaN-based LED wafers,¹³ we believe that the indium electrode performs well in this work. On the other hand, because gold (Au) can form a good ohmic contact with

ZnO,² an Au wire was directly used as the n-electrode. The Au wire with a diameter of 0.1 mm was placed onto the top of ZnO NRs and slightly pressed by a glass plate. Next, the sample was inserted into the rapidly thermal annealing (RTA) system, which was set at 400°C for 30 sec. According to our measurements (not shown here), it is found that under the same forward bias, the current could be enhanced by 100 times after the RTA treatment compared with that before RTA process. Therefore, it is expected that the Au electrode will serve as a good contact in our study. Both p- and n-contact areas were estimated to be about 0.2 mm². Scanning electron microscope (SEM) images were recorded using a JEOL JSM 6500 system. X-ray diffraction (XRD) spectra were obtained on a PANalytical X'Pert Pro diffractometer using Cu K_α radiation ($\lambda=1.5418 \text{ \AA}$) at 45 kV and 40 mA. Photoluminescence (PL) and electroluminescence (EL) measurements were performed by a Jobin Yvon SPEC-1403 spectral system working in the double-grating mode. For examining the polarization state of the emission, a polarizer was inserted before the entrance of the spectrometer, and then a depolarizer was used to exclude the influence of the response due to the orientation of the grating. The optical source was provided by a He-Cd laser with the wavelength of 325 nm, and the electric source was provided by a Keithley 236 unit.

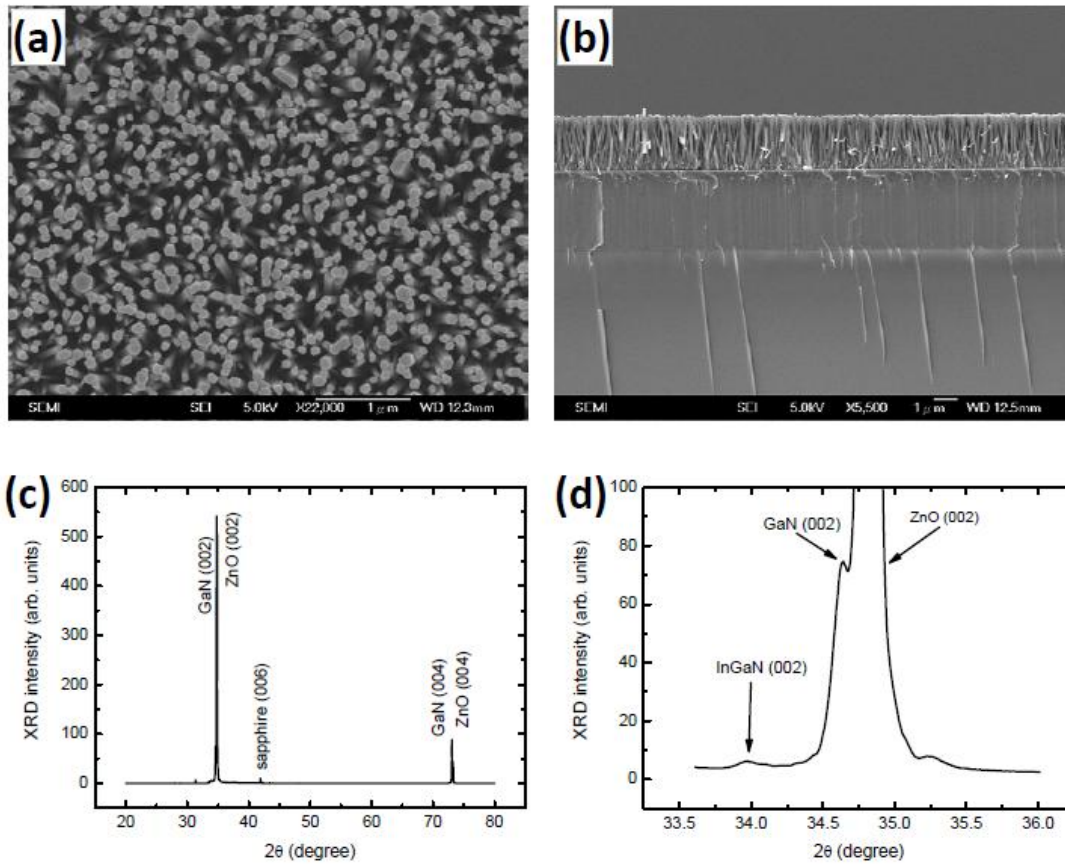


Fig. 5.1 (a) Top view and (b) side view of scanning electron microscope images of InGaN/GaN/ZnO nanocomposite material. (c) X-ray diffraction spectrum and (d) x-ray diffraction spectrum with enlarged scale of 33.6-36.0 degree in (c).

5.3 Results and Discussion

As shown in Figs. 5.1(a) and (b), ZnO NRs with around 2.2 μm in length and 100 nm in diameter were well grown on the top surface of InGaN/GaN MQWs. Figures 5.1(c) and (d) show the X-ray diffraction patterns, which reveal well organized lattice via the corresponding peaks of ZnO, GaN, and InGaN.^{1, 4, 14} Since ZnO and GaN have a close lattice constant and the same wurtzite structure, it is expected the growth of ZnO NRs will follow the orientation of GaN substrate.¹⁵ Indeed, the X-ray diffraction spectra in Figs. 5.1(c) and (d) reveal this prediction. It means that ZnO and GaN have the same crystalline phase and orientation.

Figure 5.2(a) illustrates the experimental configuration of electroluminescence (EL) measurements of the composite LED, where the arrow symbols denote the flowing direction of electric current under forward bias. Figure 5.2(b) shows the current through the LED as a function of the bias voltage, in which we can clearly see that the current-voltage characteristic curve of the device reveals a diode-like behavior. Figure 5.2(c) shows the current-dependent EL spectra of the LED under forward bias. There are two main EL peaks located at 380 nm and 440 nm in the EL spectra under different forward bias. The two peaks could be attributed to the emissions arising from ZnO NRs and InGaN/GaN MQWs, which could be supported by the evidences given below.

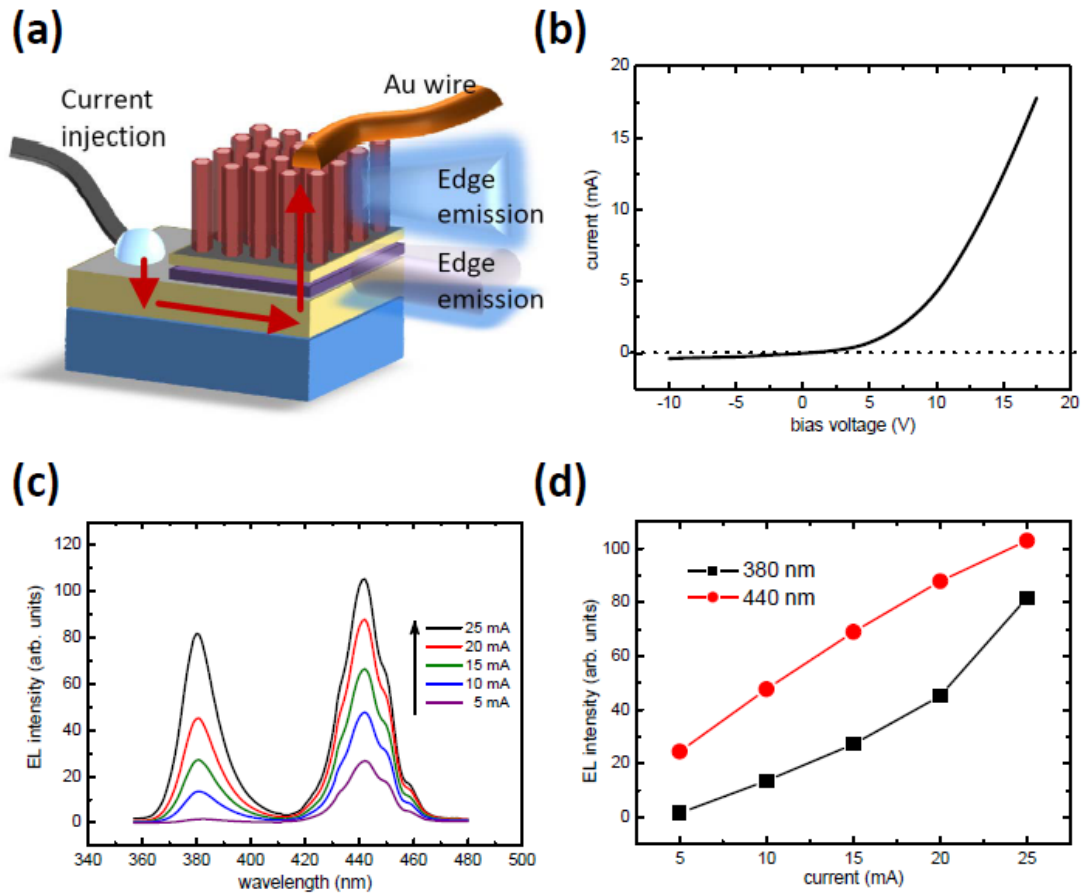


Fig. 5.2 (a) Illustration of experimental details of electroluminescence measurements for the composited light-emitting device. (b) The current through the light-emitting device as a function of bias voltage. (c) Current dependence of electroluminescence spectra of the composited light-emitting device. (d) Intensities of the 380 nm and 440 nm emissions as functions of the injection current.

Figure 5.3 illustrates the band diagram of the device under forward bias according to the previous reports.^{16, 17} Due to the quantum confined effect, the injected electrons from n-ZnO and the holes from p-GaN are easily confined in the intrinsic InGaN layers of MQWs, and the confined electron-hole pairs could recombine via radiative process by emitting 440 nm photons. According to the previous reports,^{18, 19} if the barriers of MQWs are not specially treated, such as effective doping, holes may readily overflow through intrinsic barriers into n-ZnO NRs under forward bias, especially under higher carrier injection.¹⁷ When the hole current overflows in, electron-hole pairs can also recombine in n-ZnO NRs accompanied by the emission of 380 nm photons as shown in our previous work,²⁰ which could be attributed to the NBE emission of ZnO NRs. As shown in Fig 5.2(c), it is worth noting that the intensities of both EL peaks were found to increase with increasing forward bias. In addition, we can also see that the intensity ratio between the two emissions changes with increasing bias voltage. Under lower bias, the emission intensity of 380 nm is weaker than that of 440 nm. However, with higher bias, the intensities of the two emissions become comparable. The intensities of both emissions were plotted in Fig. 5.2(d) as functions of the injection current. The emission intensity of 440 nm shows a trend of saturation, whereas the increasing rate of the intensity of 380 nm gets faster

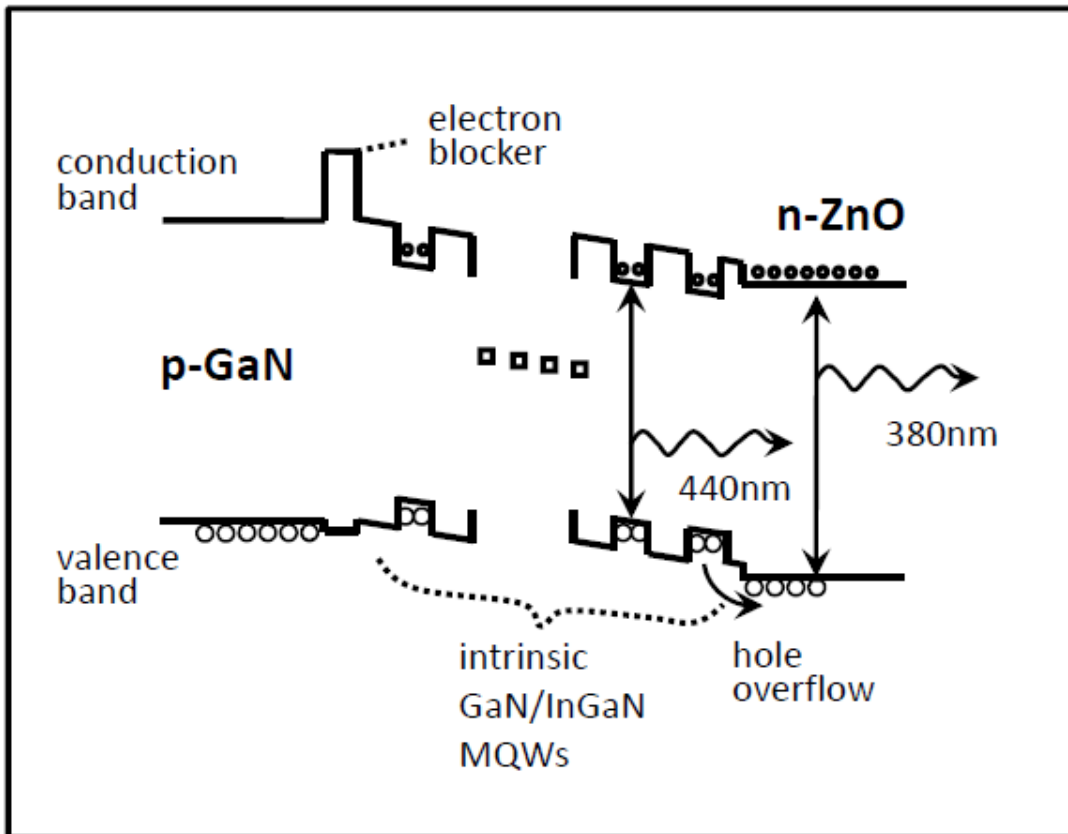
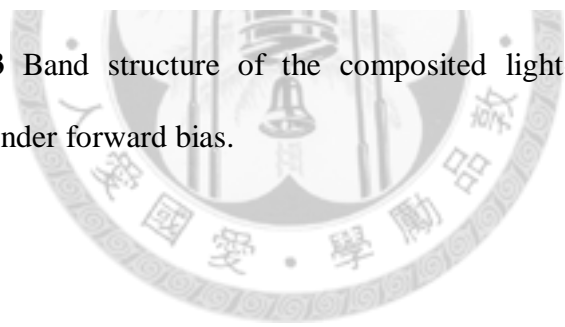


Fig. 5.3 Band structure of the composited light-emitting device under forward bias.



under higher injection current. This is a typical behavior of the hole overflow.¹⁹ As the injection current increases, the carrier concentration in the MQWs region increases and the Fermi energy rises, so that a higher overflow rate could be reasonably expected.¹⁹ As a result, the emission intensity arising from ZnO NRs can catch up with that from InGaN/GaN MQWs when the injection current increases.

Quite interestingly, when we examine the polarization state of the emission, it is found that the relative intensity between these two EL peaks strongly depends on the polarization as shown in Fig. 5.4(a). Here, 0° is defined as the polarization state parallel to the direction lying in the plane of the MQWs, and 90° is defined as the polarization state parallel to the direction along the growth direction of ZnO NRs (*c*-axis). In order to understand the polarization property of the LED device more precisely, we fixed the monochromator at 380 nm and 440 nm, respectively, and then recorded the intensity of each EL peak with an interval of 15° of the polarizer angle as shown in Figs. 5.4(b) and (c). Clearly, the intensities of the dual emissions are functions of the angle of polarizer. The result shows that we can obtain the maximum intensity of 380 nm when the polarization axis of the polarizer is parallel to the ZnO nanorod orientation (90°), and the minimum intensity at the perpendicular direction (0°). On the other hand, the emission intensity of 440 nm shows a complementary result that the maximum intensity is at 0° and the minimum intensity is at 90° .

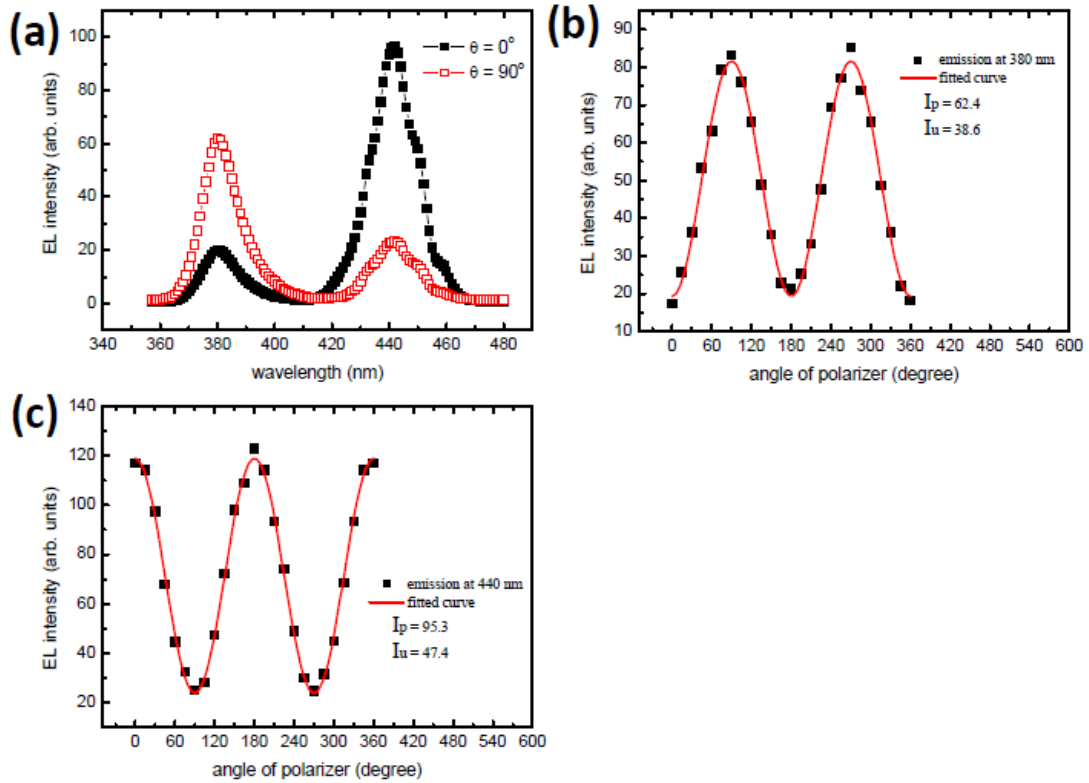


Fig. 5.4 (a) Electroluminescence (EL) spectra from the composited light-emitting device through a rotatable polarizer with the angle of 0° and 90° . (b) Polarizer-angle-dependent EL intensities with the monochromator fixed at 380 nm and (c) 440 nm, respectively. Malus's-law-fitted lines of 380 nm and 440 nm emissions by equation (2) are also shown in (b) and (c).

As shown in Figs. 5.4(b) and (c), both polarizations of the dual emissions can be described by the Malus's law quite well,²¹

$$I(\theta) = I_p \cos^2(\theta + \phi) + \frac{1}{2} I_u, \quad (5.1)$$

where $I(\theta)$ is the intensity, I_p is the polarized term, I_u is the unpolarized term, θ is the angle of the polarizer as we described before, and ϕ is the phase angle depending on the geometry of structure.

In order to provide more evidences to confirm that the origin of these two emissions arises from ZnO NRs and InGaN/GaN MQWs, we have performed PL measurements on these two materials individually as shown in Fig. 5.5. Both samples were grown on sapphire substrates under the same condition as we stated above. The edge emission from ZnO NRs shown in Fig. 5.5(a) has a narrow line located at 380 nm.³ The polarization state of the NBE emission is strongly polarized along the growth direction of ZnO NRs (c -axis). On the other hand, the emission spectrum from the edge of pure InGaN/GaN MQWs exhibits a narrow line located at 440 nm with Fabry-Perot interference patterns as shown in Fig. 5.5(b).²² The emission was found to be strongly linear-polarized lying on the epitaxial plane (0001). In other words, the polarization states of the emissions of ZnO NRs and InGaN/GaN MQWs are perpendicular to each other. The degrees of polarization for ZnO NRs and InGaN/GaN MQWs are about 56.3 % and 62.6 %, respectively, via the calculation by

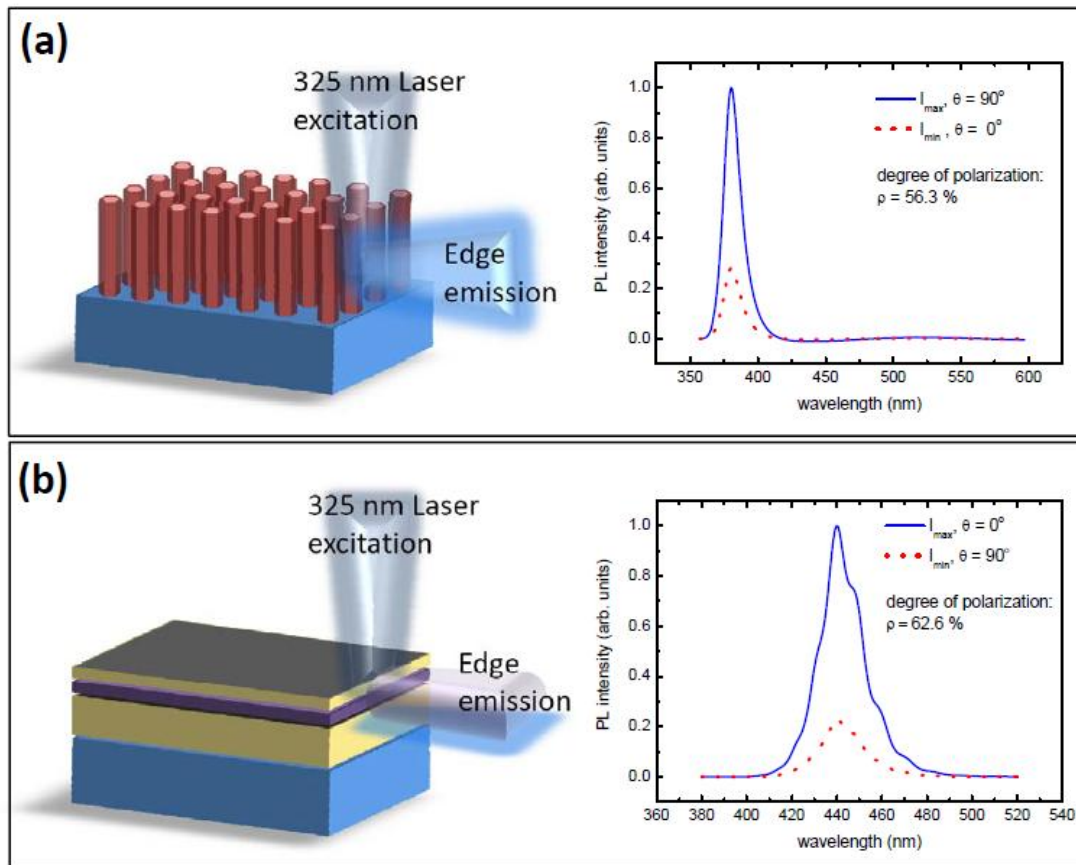


Fig. 5.5 Illustrations of the experimental details and measured spectra under different polarization for (a) InGaN/GaN quantum wells and (b) ZnO nanorods.

the following formula,²¹

$$\rho = \frac{I_{\max} - I_{\min}}{I_{\max} + I_{\min}}, \quad (5.2)$$

where ρ is the degree of polarization, I_{\max} is the maximum intensity, and I_{\min} is the minimum intensity. It has been reported that the emitted light from a highly orientational structure is usually linearly polarized due to their anisotropic geometry,^{5, 6, 23-25} therefore, the fact that both samples have their polarization states could be reasonably explained. Because the strongly linear-polarized emissions from these two materials are perpendicular to each other, it could be expected that the emission from the composite consisting of ZnO NRs and InGaN/GaN MQWs should retain the property of each constituent material. Thus, through the manipulation of the properties of the constituent elements, the underlying mechanism of the intriguing property of the dual emissions can be well understood.

5.4 Conclusion

In conclusion, we have demonstrated a novel LED based on the composite consisting of ZnO NRs and InGaN/GaN MQWs. The newly designed LED has the capability to emit dual beam radiations. Quite interestingly, the relative intensity between the dual emissions can be manipulated by a polarizer. The underlying mechanism can be well interpreted in terms of the anisotropic optical properties arising from the geometric structures of the constituent nanoscale materials. Our result

presented here can be extended to many other nanostructured composites, and it therefore may open a new pathway for the creation of optoelectronic devices with tunable properties.

Reference

1. J. H. Lim, C. K. Kang, K. K. Kim, I. K. Park, D. K. Hwang, and S. J. Park, "UV electroluminescence emission from ZnO light-emitting diodes grown by high-temperature radiofrequency sputtering," *Adv. Mater.* **18**, 2720-2724 (2006).
2. H. K. Fu, C. L. Cheng, C. H. Wang, T. Y. Lin, and Y. F. Chen, "Selective angle electroluminescence of light-emitting diodes based on nanostructured ZnO/GaN heterojunctions," *Adv. Funct. Mater.* **19**, 3471-3475 (2009).
3. Ü. Özgür, Ya. I. Alivov, C. Liu, A. Teke, M. A. Reshchikov, S. Doğan, V. Avrutin, S.-J. Cho, and H. Morkoç, "A comprehensive review of ZnO materials and devices," *J. Appl. Phys.* **98**, 041301 (2005).
4. M. H. Huang, S. Mao, H. Feick, H. Yan, Y. Wu, H. Kind, E. Weber, R. Russo, and P. Yang, "Room-temperature ultraviolet nanowire nanolasers," *Science* **292**, 1897-1899 (2001).
5. N. E. Hsu, W. K. Hung, and Y. F. Chen, "Origin of defect emission identified by polarized luminescence from aligned ZnO nanorods," *J. Appl. Phys.* **96**, 4671-4673 (2004).
6. M. F. Schubert, S. Chhajed, J. K. Kim, E. F. Schubert, and J. Cho, "Origin of defect emission identified by polarized luminescence from aligned ZnO nanorods," *Appl. Phys. Lett.* **91**, 051117 (2007).
7. H. S. Chen, C. W. Chen, C. H. Wang, F. C. Chu, C. Y. Chao, C. C. Kang, P. T. Chou, and Y. F. Chen, "Color-tunable light-emitting device based on the mixture

- of CdSe nanorods and dots embedded in liquid-crystal cells,” *J. Phys. Chem. C* **114**, 7995-7995 (2010).
8. N. Kikuchi, “Analysis of signal degree of polarization degradation used as control signal for optical polarization mode dispersion compensation,” *J. Lightwave Technol.* **19**, 480-486 (2001).
 9. J. R. Law, “Color selection polarizing beam splitter,” U. S. Patent 3497283 (1970).
 10. S. J. Savory, “Digital filters for coherent optical receivers,” *Opt. Express* **16**, 804-817 (2008).
 11. C. Bayram, F. H. Teherani, D. J. Rogers, and M. Razeghi, “A hybrid green light-emitting diode comprised of n -ZnO/(InGaN/GaN) multi-quantum-wells/ p -GaN,” *Appl. Phys. Lett.* **93**, 081111 (2008).
 12. M. Guo, P. Diao, and S. Cai, “Hydrothermal growth of well-aligned ZnO nanorod arrays: Dependence of morphology and alignment ordering upon preparing conditions,” *J. Sol. Sta. Chem.* **178**, 1864-1873 (2005).
 13. C. F. Huang, C. F. Lu, T. Y. Tang, J. J. Huang, and C. C. Yang, “Phosphor-free white-light light-emitting diode of weakly carrier-density-dependent spectrum with prestrained growth of InGaN/GaN quantum wells,” *Appl. Phys. Lett.* **90**, 151122 (2007).
 14. Y. T. Moon, D. J. Kim, K. M. Song, I. H. Lee, M. S. Yi, D. Y. Noh, C. J. Choi, T. Y. Seong, and S. J. Park, “Optical and structural studies of phase separation in InGaN film grown by MOCVD,” *Phys. Stat. Sol. (b)* **216**, 167-170 (1999).
 15. J. von Pezold and P. D. Bristowe, “Atomic structure and electronic properties of the GaN/ZnO (0001) interface,” *Journal of Materials Science* **40**, 3051-3057 (2004).

16. K. W. Jang, D. C. Oh, T. Minegishi, H. Suzuki, T. Hanada, H. Makino, M. W. Cho, T. Yao, and S. K. Hong, "ZnO/GaN heteroepitaxy," *Mater. Res. Soc. Symp. Proc.* **829**, B10.3.1-B10.3.12 (2005).
17. E. Fred Schubert, *Light-Emitting Diodes, 2nd edition*, (Cambridge University Press, 2006), Chap. 4.
18. E. H. Park, D. N. H. Kang, I. T. Ferguson, S. K. Jeon, J. S. Park, and T. K. Yoo, "The effect of silicon doping in the selected barrier on the electroluminescence of InGaN/GaN multiquantum well light emitting diode," *Appl. Phys. Lett.* **90**, 031102 (2006).
19. Z. Z. Bandic, P. M. Bridger, E. C. Piquette, and T. C. McGill, "Minority carrier diffusion length and lifetime in GaN," *Appl. Phys. Lett.* **72**, 3166-3168 (1998).
20. J. Y. Wang, C. Y. Lee, Y. T. Chen, C. T. Chen, Y. L. Chen, C. F. Lin, and Y. F. Chen, "Double side electroluminescence from p-NiO/n-ZnO nanowire heterojunctions," *Appl. Phys. Lett.* **95**, 131117 (2009).
21. E. Hecht, *Optics, 4th edition* (Addison Wesley, 2002), Chap. 8.
22. T. Y. Lin, "Converse piezoelectric effect and photoelastic effect in InGaN/GaN multiple quantum wells," *Appl. Phys. Lett.* **82**, 880-882 (2003).
23. K. J. Wu, K. C. Chu, C. Y. Chao, Y. F. Chen, C. W. Lai, C. C. Kang, C. Y. Chen, and P. T. Chou, "CdS nanorods imbedded in liquid crystal cells for smart optoelectronic devices," *Nano Lett.* **7**, 1908-1913 (2007).
24. H. K. Fu, C.W. Chen, C.H. Wang, T. T. Chen, and Y. F. Chen, "Creating optical anisotropy of CdSe/ZnS quantum dots by coupling to surface plasmon polariton resonance of a metal grating," *Opt. Express* **16**, 6361-6367 (2008).
25. N. F. Gardner, J. C. Kim, J. J. Wierer, Y. C. Shen, and M. R. Krames, "Polarization anisotropy in the electroluminescence of m-plane InGaN–GaN

multiple-quantum-well light-emitting diodes,” Appl. Phys. Lett. **86**, 111101 (2005).



Chapter 6

Optical Detection of Glucose Based on the Composite Consisting of Enzymatic ZnO Nanorods and InGaN/GaN Multiple Quantum Wells

6.1 Introduction

Since the first glucose enzyme electrode was developed by Clark and Lyons, Glucose biosensors have been widely studied and developed.¹ They were generally constructed based on electron transfer in the electrode through the mediator between oxygen and glucose oxidase (GOx),² and numerous studies were focused on the techniques of immobilization of glucose with carbon nanotubes and gold particles.²⁻⁴ Recently, one-dimensional ZnO nanostructures have been used as biocompatible materials including gas and pH sensors.⁵⁻⁸ In addition, electrostatic interaction between low dimensional ZnO and GOx is favorable due to their huge difference in isoelectric points and high surface-to-volume ratio,^{9,10} such that the nanostructures have been demonstrated to have unique advantages including ultrasensitivity and biocompatibility. In_xGa_{1-x}N/GaN MQWs have been generally used in commercial high-efficiency blue LEDs since the evolution from the first GaN based blue LED produced by Shuji Nakamura's group.¹¹ By changing the composition, the LEDs can emit wavelengths covering from ultraviolet to infrared radiation. Current III-nitride-based optoelectronic devices employing multiple quantum wells (MQWs) grown along the polar *c*-direction were characterized by the presence of polarization

induced electrostatic fields. The internal electric fields result in the spatial separation of the electron and hole wave functions within quantum wells and give rise to the quantum confined Stark effect (QCSE),^{12,13} which leads in the dependency between pumping intensity and the peak position of emission. With the increase of pumping power density, the screening of the internal electric field due to electron-hole pairs is more effective, and the tilting of the energy band structure becomes less pronounced. It thus leads to the increase in the transition energy and the blue-shift of the observed spectra. However, the internal electric field could be efficiently reduced via the prestrained growth method, thus the blue-shift behavior can be greatly reduced with the increasing pumping intensity.¹⁴

In this work, we introduced an intelligently designed composite consisting of prestrained InGaN/GaN MQWs and ZnO nanorods, which could serve as an intriguing glucose sensor with high sensitivity and convenience by optical detection. The underlying mechanism can be well understood by the fact that enzyme-immobilized ZnO nanorods have a strong ability to capture the target glucose molecules due to the large surface-to-volume ratio. The reduction-oxidation (REDOX) reaction has an influence on the MQWs, thus the change in emission and Raman spectra could be clearly observed. Previously, biologically modified field effect transistors (FETs) have been developed to directly detect biochemical interactions for

a variety of applications.^{7,15} However, in the FET related techniques, ones often consume much cost and time in constructing electronic structures such as ohmic contacts, junctions and electrodes, and in some cases it is not convenient to do the electric current measurements. Therefore, our result shown here may open a possibility for the generation of biosensors with optical detection methods.

6.2 Experiment

The studied InGaN/GaN MQWs were prepared by low-temperature metal-organic chemical vapor deposition. An undoped series of ten periods of 2-nm-thick In_{0.25}Ga_{0.75}N wells and 9-nm-thick GaN barriers were grown on *c*-plane (0001) sapphire. There is a 3 μm n-GaN layer between sapphire and MQWs. An extra InGaN/GaN QW of a lower indium content was deposited between the n-GaN layer and the ten high indium QWs as a prestrained layer. ZnO nanorods were grown on the top surface of MQWs via hydrothermal method as described in the previous reports.¹⁶ Scanning electron microscope (SEM) images were recorded using a JEOL JSM 6500 system. The GOx (100 U/mg, Sigma) solution was prepared with concentration of 10 mg/ml in 10 mM phosphate buffer saline (PBS) solution at the pH value of 7.4. Micro-photoluminescence (μ-PL) measurements were taken by a Jobin Yvon TRIAX-320 spectral system with an OLYMPUS microscope, and the optical source is provided by a solid state laser working at 374 nm. Micro-Raman (μ-Raman) spectra

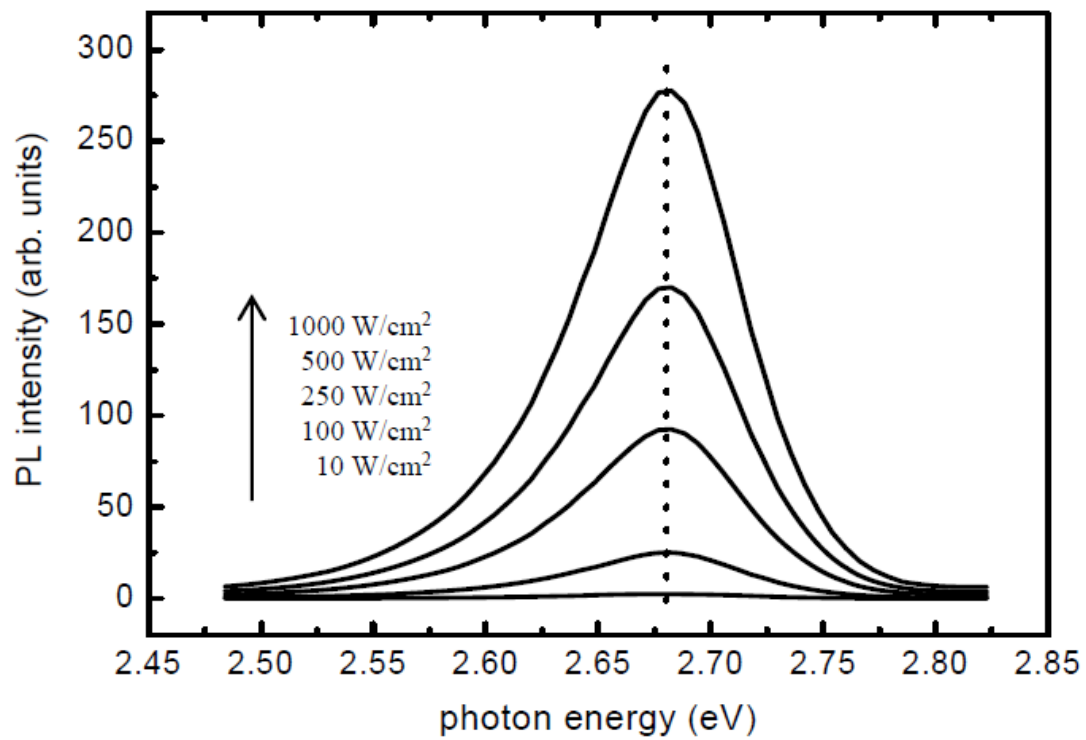


Fig. 6.1 Photoluminescence spectra of InGaN/GaN multiple quantum wells (MQWs) under different excitation power densities.

were performed by a Jobin Yvon SPEC-T64000 spectral system with an OLYMPUS microscope, and the optical source is provided by an Ar⁺ laser working at 514 nm.

6.3 Results and Discussion

In the beginning, to demonstrate the disappearance of build-in internal electric field in our studied InGaN/GaN MQWs, we have performed Micro-photoluminescence (μ -PL) spectra under different optical excitation power densities as shown in Fig. 6.1. The PL peak position of our MQWs remains unchanged with the increasing excitation power density. It reveals that the internal electric field is efficiently reduced due to the prestrained layer, otherwise, the peak position will cause a blue-shift because of QCSE and the screening effect by photoexcited electron-hole pairs.

As shown in Figs. 6.2 (a) and (b), ZnO nanorods with around 2.2 μ m in length and 100 nm in diameter were well grown on the top surface of InGaN/GaN MQWs. Figure 6.2 (c) displays the schematic diagram of the device consisting of InGaN/GaN MQWs and ZnO nanorods. After fabricating the device, it was immersed into the GOx solution and kept at 4 °C for 48 hours for GOx immobilization on the ZnO nanorods followed by an extensively washing with phosphate buffer saline (PBS) solution to remove the unimmobilized GOx. The device was kept in the incubator for 30 min to make the enzyme active around 37 °C. The target glucose (Sigma) was

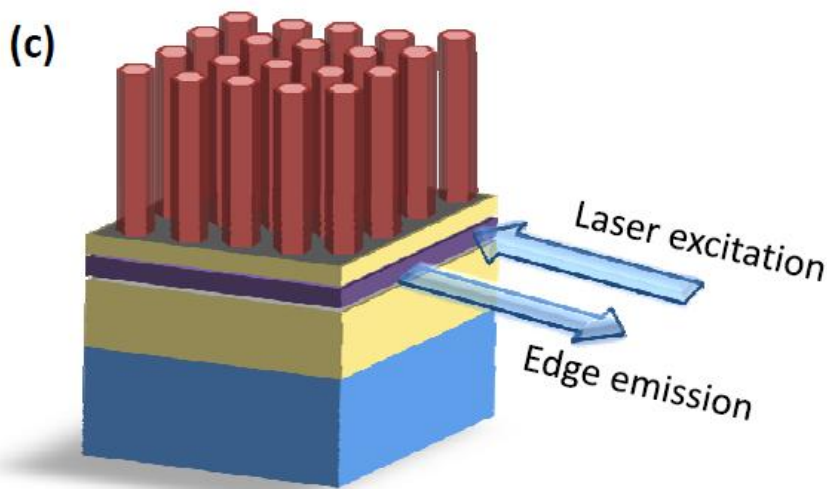
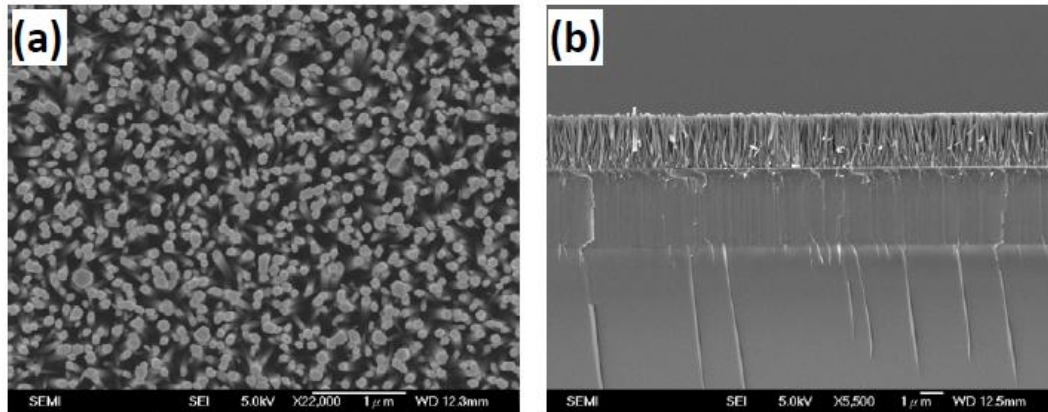


Fig. 6.2 (a) Top view and (b) side view of scanning electron microscope images ZnO nanorods grown on the top surface of InGaN/GaN multiple quantum wells. (c) The schematic diagram of the glucose sensing device. Both excitation and emission are taken at the edge side of the device.

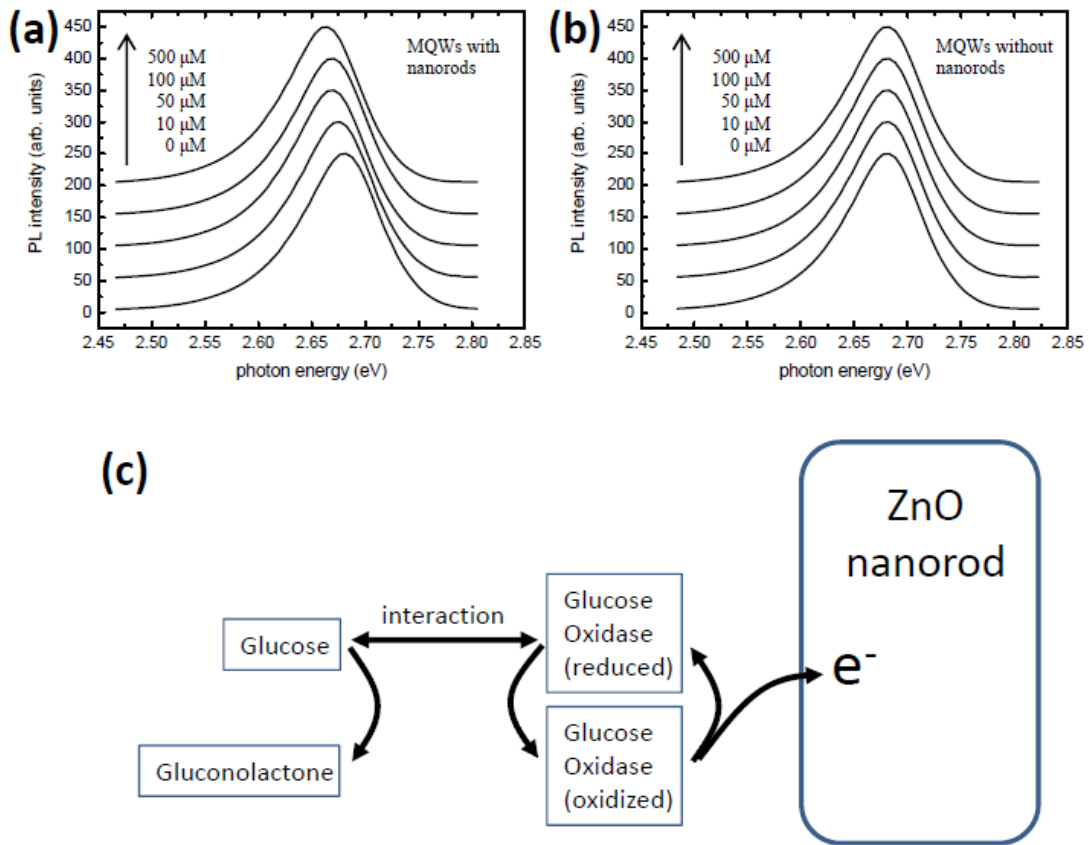


Fig. 6.3 Photoluminescence spectra of InGaN/GaN multiple quantum wells (a) with and (b) without enzymatic ZnO nanorods with increasing target glucose concentration. (c) Illustration diagram of the reduction-oxidation reaction between glucose oxidase and glucose molecules occurring on the surfaces of nanorods.

applied to the device through a micropipette, and then PL measurements were taken on the cross section of MQWs as shown in Fig. 6.2 (c) under different glucose concentration. Quite interestingly, we can see that the peak position of PL spectrum of InGaN/GaN MQWs in Fig. 6.3 (a) shows a red-shift from 2.683 eV to 2.665 eV with the increasing target glucose concentration from 0 μ M to 500 μ M. On the other hand, we further prepared a referenced sample of MQWs without ZnO nanorods. It was treated by the same process as the above description, however, we cannot see an obvious shift in PL spectrum with the increasing glucose concentration as shown in Fig. 6.3 (b). This result may be preliminarily attributed to the REDOX reaction between GOx on nanorods and target glucose molecules as illustrated in Fig. 6.3 (c).¹⁷ After the reaction between GOx(ox) and glucose molecules, they become GOx(red) and gluconolactone molecules, where GOx(ox) and GOx(red) represent GOx in oxidized and reduced states, respectively. A GOx(red) molecule could release an electron to ZnO and become a GOx(ox) again. Therefore, ZnO nanorods would carry negative charges, which will create an electric field and tilt the band structure and alter the emission spectrum of InGaN/GaN MQWs. Therefore, the result shown in Figs. 6.3 (a) and (b) can be well interpreted. Figures 6.4 (a) and (b) provide a clear picture to illustrate the influence on energy band structures of MQWs under different glucose conditions. Before target glucose injection, the energy band of MQWs is initially flat

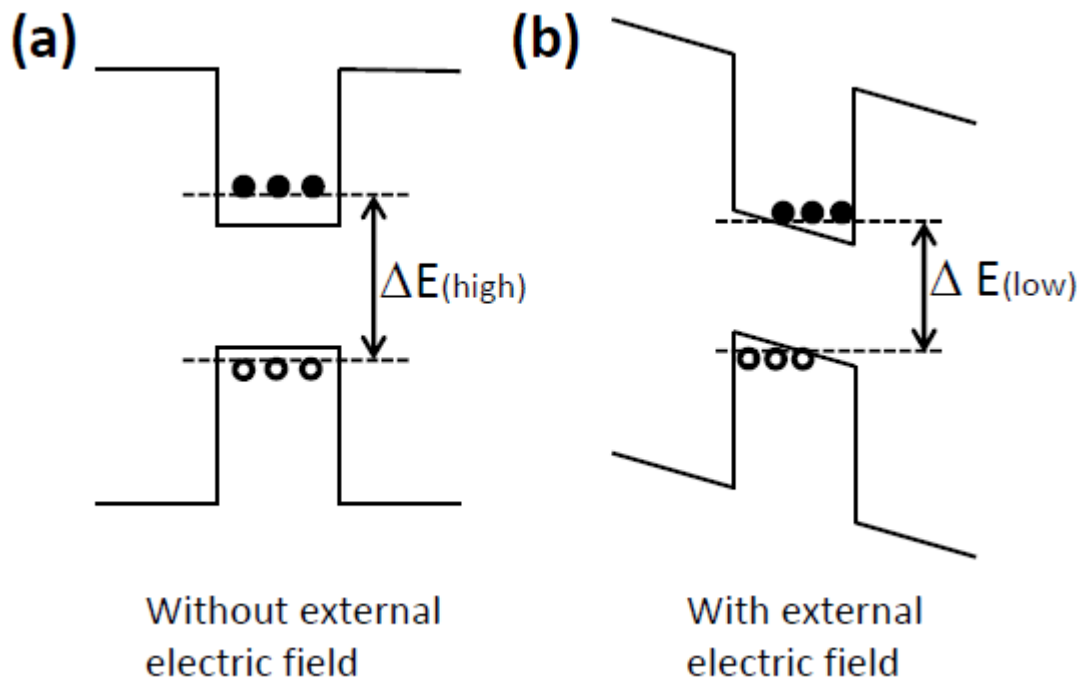
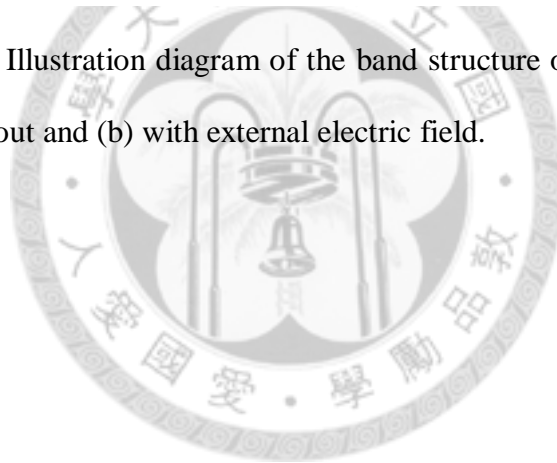


Fig. 6.4 Illustration diagram of the band structure of MQWs
 (a) without and (b) with external electric field.



as shown in Fig. 6.4 (a). Once the glucose is injected, the REDOX reaction occurs on ZnO nanorods of the device, such that the accumulated negative charges would create an external electric field and tilt the band structure of MQWs, as a result the recombination energy of electron-hole pairs is reduced due to QCSE, which causes a red-shift in PL spectra.^{18,19} According to our previous report,²⁰ the magnitude of the electric field in the MQWs could be estimated to be in the order of 10^5 - 10^6 V/cm because of the similar widths of MQWs (2 nm for quantum wells , 9 nm for barriers) as well as the change of peak position (~ 20 meV) compared with the results in Ref. 20.

To further confirm the above interpretation, we have performed Micro-Raman (μ -Raman) scattering measurements for InGaN/GaN MQWs with/without ZnO nanorods under different concentrations of target glucose solution as shown in Figs. 6.5 (a) and (b). The spectrum located near 732 cm^{-1} can be assigned to InGaN $A_1(\text{LO})$ mode.¹⁹ With nanorods, the Raman spectra of MQWs in Fig. 6.5 (a) show a clear high-energy shift in the peak position with respect to the increase of the target glucose concentration, while the spectra corresponding to that without nanorods in Fig. 6.5 (b) remain unchanged. This intriguing behavior can also be understood by the converse-piezoelectric effect, which means that an external electric field could induce a strain in piezoelectric materials.²⁰ Here, the modification of the external electric

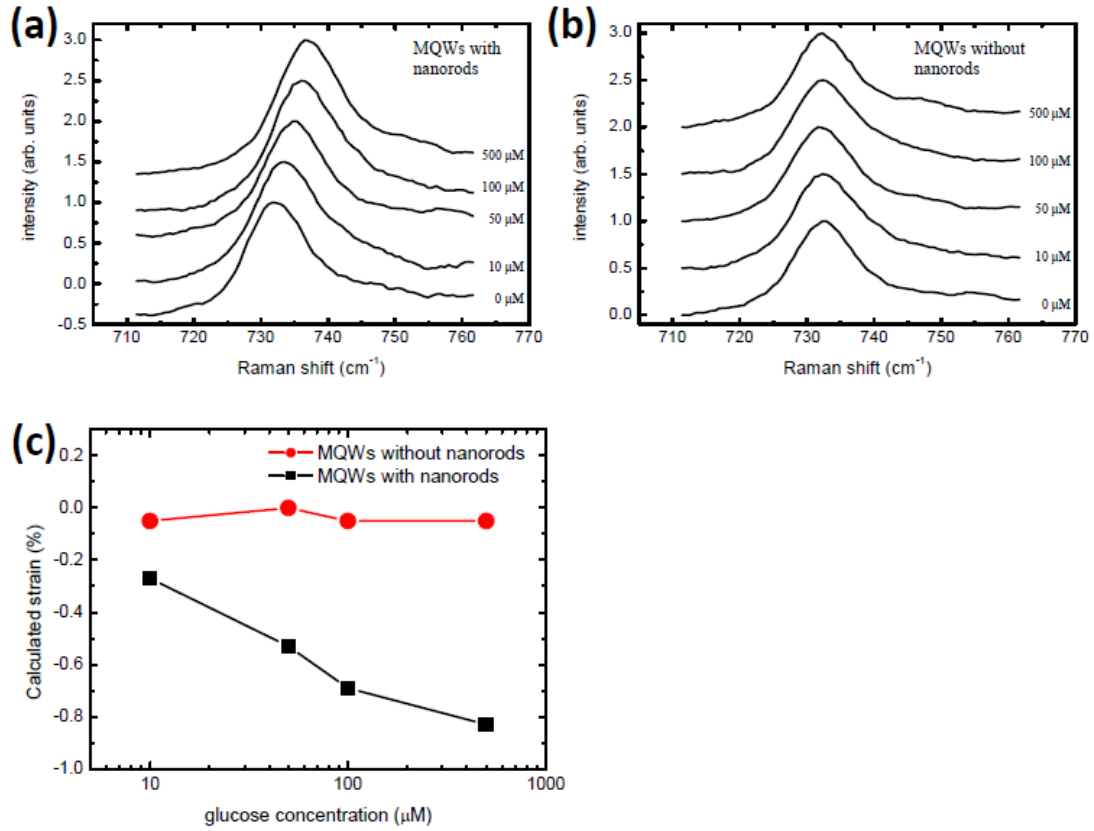


Fig. 6.5 Raman spectra of InGaN/GaN multiple quantum wells (a) with and (b) without enzymatic ZnO nanorods with increasing target glucose concentration. (c) Estimated lattice strain of InGaN/GaN multiple quantum wells as a function of the target glucose concentration via Eq. (6.1).

field arises from the REDOX reaction of GOx on nanorods and target glucose molecules as described above. Because nitride semiconductors are good piezoelectric materials, a change of electric field in the lattice can produce a strain and alter the lattice constant, which then leads to the change of the Raman scattering spectra.¹⁶ According to the PL spectra shown in Fig. 6.3 (a), the electric field in lattice is increased after REDOX reaction, and therefore a high-frequency shift of the LO phonon energy can be expected. This expectation is consistent with what has been observed as shown in Fig. 6.5 (a). On the other hand, the Raman spectra of the device without nanorods as shown in Fig. 6.5 (b) exhibit that pure InGaN/GaN MQWs are not sensitive to target glucose. Thus the result let us make the conclusion that the additional dimension provided by ZnO nanorods plays an important role in the detection ability.

Let us now examine the internal strain based on the Raman scattering measurements. The magnitude of the strain can be estimated by the high-energy shift of the A₁(LO) phonon mode according to the following equation:²¹

$$\varepsilon = \frac{\Delta\omega}{2\left(a - b\frac{C_{13}}{C_{33}}\right)}, \quad (6.1)$$

where a and b are phonon deformation potentials, and C_{13} and C_{33} are elastic constants, respectively. Figure 6.5 (c) shows the strain as a function of target glucose concentration calculated from Eq. (6.1), where the deformation potentials a , b and the

elastic constants C_{13} , C_{33} were estimated by the extrapolation of the data for GaN and InN.²² With ZnO nanorods, the strain of InGaN/GaN MQWs of the device in glucose solution increases with increasing glucose concentration as expected. We therefore can see that the shifts in both PL spectra and Raman scattering of the detection device can be well explained in a consistent way based on the piezoelectric alteration due to the REDOX reaction.

6.4 Conclusion

In conclusion, we have demonstrated that the optical properties of InGaN/GaN MQWs with enzymatic ZnO nanorods can be used to detect glucose molecules. The underlying mechanism is based on the highly sensitive nature of nanorods and piezoelectric property of nitride semiconductors under different ambient environment. Our working principle shown here can be readily extended by employing many other biomolecules for surface functionalization and by using different chemistries. In view of the wide application of LEDs and laser diodes based on nitride semiconductors, the study carried out along our guideline should be very useful for the creation of highly sensitive biosensors using optical detection.

References

1. Clark, L. C. Jr.; Lyons, C. *Ann. N.Y. Acad. Sci.* **1962**, *102*, 29.
2. Park, S.; Boo, H.; Chung, T. D. *Anal. Chim. Acta* **2006**, *556*, 46.

3. Kim, S. N.; Rusling, J. F.; Papadimitrakopoulos, F. *Adv. Mater.* **2007**, *19*, 3214.
4. Yan, Yi-Ming; Ran, Tel-Vered; Yehezkeli, O.; Cheglakov, Z.; Willner, I. *Adv. Mater.* **2008**, *20*, 2365.
5. Heo, Y. W.; Norton, D. P.; Tien, L. C.; Kwon, Y.; Kang, B. S.; Ren, F.; Pearton, J. S.; LaRoche, J. R. *Mater. Sci. Eng. R.* **2004**, *47*, 1.
6. Wang, H. T.; Kang, B. S.; Ren, F.; Tien, L. C.; Sadik, P. W.; Norton, D. P.; Pearton, S. J.; Lin, J. *Appl. Phys. Lett.* **2005**, *86*, 243503.
7. Kang, B. S.; Ren, F.; Heo, Y. W.; Tien, L. C.; Norton, D. P.; Pearton, S. J. *Appl. Phys. Lett.* **2005**, *86*, 112105.
8. Fan, Z. Y.; Lu, J. G. *J. Nanosci. Nanotechnol.* **2005**, *5*, 1561.
9. Wang, J. X.; Sun, X. W.; Wei, A.; Lei, Y.; Cai, X. P.; Li, C. M.; Dong, Z. L. *Appl. Phys. Lett.* **2006**, *88*, 233106.
10. Wei, A.; Sun, X. W.; Wang, J. X.; Lei, Y.; Cai, X. P.; Li, C. M.; Dong, Z. L.; Huang, W. *Appl. Phys. Lett.* **2006**, *89*, 123902.
11. Nakamura, S.; Pearton, S.; Fasol, G. *The blue laser diode: GaN based light emitters and lasers*, 2nd edition; Springer: New York, 1997; pp1–5.
12. Takeuchi, T.; Sota, S.; Katsuragawa, M.; Komori, M.; Takeuchi, H.; Amano, H.; Akasaki, I. *Jpn. J. Appl. Phys., Part 2* **1997**, *36*, L382.
13. Bernardini, F.; Fiorentini, V.; Vanderbilt, D. *Phys. Rev. B* **1997**, *56*, R10024.

14. Huang, C. F.; Chen, C. Y.; Lu, C. F.; Yang, C. C. *Appl. Phys. Lett.* **2007**, *91*, 051121.
15. Kang, B. S.; Wang, H. T.; Ren, F.; Pearton, S. J.; Morey, T. E.; Dennis, D. M.; Johnson, J. W.; Rajagopal, P.; Roberts, J. C.; Piner, E. L.; Linthicum, K. J. *Appl. Phys. Lett.* **2007**, *91*, 252103.
16. Guo, M.; Diao, P.; Cai, S.; *J. Sol. Sta. Chem.* **2005**, *178*, 1864.
17. Chiu, J. Y.; Yua, C. M.; Yena, M. J.; Chen, L. C. *Biosensors and Bioelectronics* **2009**, *24*, 2015.
18. Lin, T. Y. *Appl. Phys. Lett.* **2003**, *82*, 880.
19. Shih, H. Y.; Chen, T. T.; Wang, C. H.; Chen, K. Y.; Chen, Y. F. *Appl. Phys. Lett.* **2008**, *92*, 261910.
20. Chen, C. H.; Chen, W. H.; Chen, Y. F.; Lin, T. Y. *Appl. Phys. Lett.* **2003**, *83*, 1770.
21. Wang, F. C.; Cheng, C. L.; Chen, Y. F.; Huang, C. F.; Yang, C. C. *Semicond. Sci. Technol.* **2007**, *22*, 896.
22. Kontos, A. G.; Raptis, Y. S.; Pelekanos, N. T.; Georgakilas, A.; Bellet-Amalric, E.; Jalabert, D. *Phys. Rev. B* **2005**, *72*, 155336.



Chapter 7

Optical Detection of Hydrogen Gas Using Pt-catalyzed ZnO Nanorods and InGaN/GaN Multiple Quantum Wells

7.1 Introduction

ZnO is an interesting semiconductor with a direct band gap energy of 3.37 eV at room temperature and a large binding energy of 60 meV.¹ It is a promising material for optoelectronics devices, such as light-emitting devices (LEDs),² solar cells,^{3,4} and gas sensors.⁵⁻⁸ For example, in gas sensor application, the devices composed of ZnO have been studied as chemoresistive materials to detect gases such as CO, NH₃, ethanol, and H₂.⁵⁻⁸ On the other hand, In_xGa_{1-x}N/GaN multiple quantum wells (MQWs) have been generally used in high-efficiency LEDs, laser diodes, and solar cells.⁹ By changing the composition of In and Ga, it can emit wavelengths covering from ultraviolet to infrared radiation. At present, the optoelectronic devices based on In_xGa_{1-x}N/GaN MQWs grown along the polar *c*-direction usually possess a strong spontaneous polarization and built-in electric field due to the excellent piezoelectricity of nitride semiconductors. The internal electric field will result in the spatial separation of the electron and hole wave functions within quantum wells and give rise to the quantum confined Stark effect (QCSE). This unique feature will cause the entanglement among stress, surface change, electronic conduction, as well as optical transition, etc., and rise several interesting behaviors.^{10,11} For instance, with the

increase of pumping power density, the screening of the internal electric field due to electron-hole pairs is more effective, and the tilting of the energy band structure becomes less pronounced. It thus leads to the increase in the transition energy and the blue-shift of the observed emission spectra.¹⁰ The internal electric field could be efficiently reduced via the prestrained growth method, thus the blue-shift behavior can be greatly reduced with the increasing pumping intensity.¹¹

In this work, we introduced an intelligently designed composite consisting of prestrained InGaN/GaN MQWs and ZnO nanorods (NRs), which could serve as an novel gas sensor by optical detection with high sensitivity. Moreover, with catalyzing by platinum (Pt) nanoparticles (NPs), it is found that the sensitivity could be greatly enhanced. The underlying mechanism can be well understood by the fact that ZnO NRs provide oxygen ions and have a strong ability to capture the target gas due to a large surface-to-volume ratio. The reduction-oxidation (REDOX) reaction has a great influence on the internal electric field of MQWs, thus the change in emission and Raman scattering spectra could be clearly observed. Previously, sensors based on field effect transistors (FETs) have been developed to directly detect chemical interactions for a variety of applications.⁵ However, in the FET related techniques, ones often consume much cost and time in constructing electronic structures such as ohmic contacts, junctions and electrodes, and in some cases it is not convenient to do

the electric current measurements. Therefore, our result shown here can open a possibility for the creation of sensitive sensors with optical detection methods.

7.2 Experiment

The studied InGaN/GaN MQWs were prepared by low-temperature metal-organic chemical vapor deposition. An undoped series of 10 periods of 2-nm-thick $\text{In}_{0.15}\text{Ga}_{0.85}\text{N}$ wells and 9-nm-thick GaN barriers were grown on *c*-plane (0001) sapphire. There is a 3 μm n-GaN layer between sapphire and MQWs. An extra InGaN/GaN QW with a lower indium content was deposited between the n-GaN layer and the 10 high indium QWs as a prestrained layer. To demonstrate the disappearance of the built-in internal electric field in our studied InGaN/GaN MQWs, we have performed micro-photoluminescence ($\mu\text{-PL}$) spectra under different optical excitation power densities. The PL peak position of the MQWs remains unchanged with the increasing excitation power density (not shown here).¹⁶ It reveals that the internal electric field is efficiently reduced due to the prestrained layer, otherwise, the peak position will cause a blue-shift because of QCSE and the screening effect by photoexcited electron-hole pairs. ZnO NRs were grown on the *c*-plane (0001) sapphire via hydrothermal method as described in the previous report.¹² As shown in Figs. 7.1 (a) and (b), ZnO NRs with around 2.2 μm in length and 100 nm in diameter were well grown on the sapphire substrate. Next, the sample of ZnO NRs was

immersed into ethanol solution and dispersed by an ultrasonic bath for 10 minutes. After ultrasonication, the suspended ZnO NRs in ethanol solution was dripped onto the MQWs by a micropipette and dried at 85 °C for 5 minutes using a hot plate. The sample was then decorated with platinum (Pt) nanoparticles (NPs) by a DC sputtering system (JEOL JFC-1600) working at 40 mA for 60 seconds. Figures 7.1 (c) and (d) display the sample before and after the decoration of Pt NPs, respectively. We can clearly see that Pt NPs have been successfully deposited on the surface of ZnO NRs. Finally, the sample was mounted in a chamber to serve as a hydrogen gas detector through observing its optical properties. Before the detection process, the chamber was filled with nitrogen, which served as the background gas, and then the target hydrogen with different concentrations was injected. The optical detections were measured at room temperature. Scanning electron microscope (SEM) images were recorded using a JEOL JSM 6500 system. Micro-photoluminescence (μ -PL) measurements were taken by a Jobin Yvon TRIAX-320 spectral system with an OLYMPUS microscope, and the optical source is provided by a solid state laser working at 374 nm. Micro-Raman (μ -Raman) scattering spectra were performed by a Jobin Yvon SPEC-T64000 spectral system with an OLYMPUS microscope, and the optical source is provided by an Ar⁺ laser working at 514 nm.

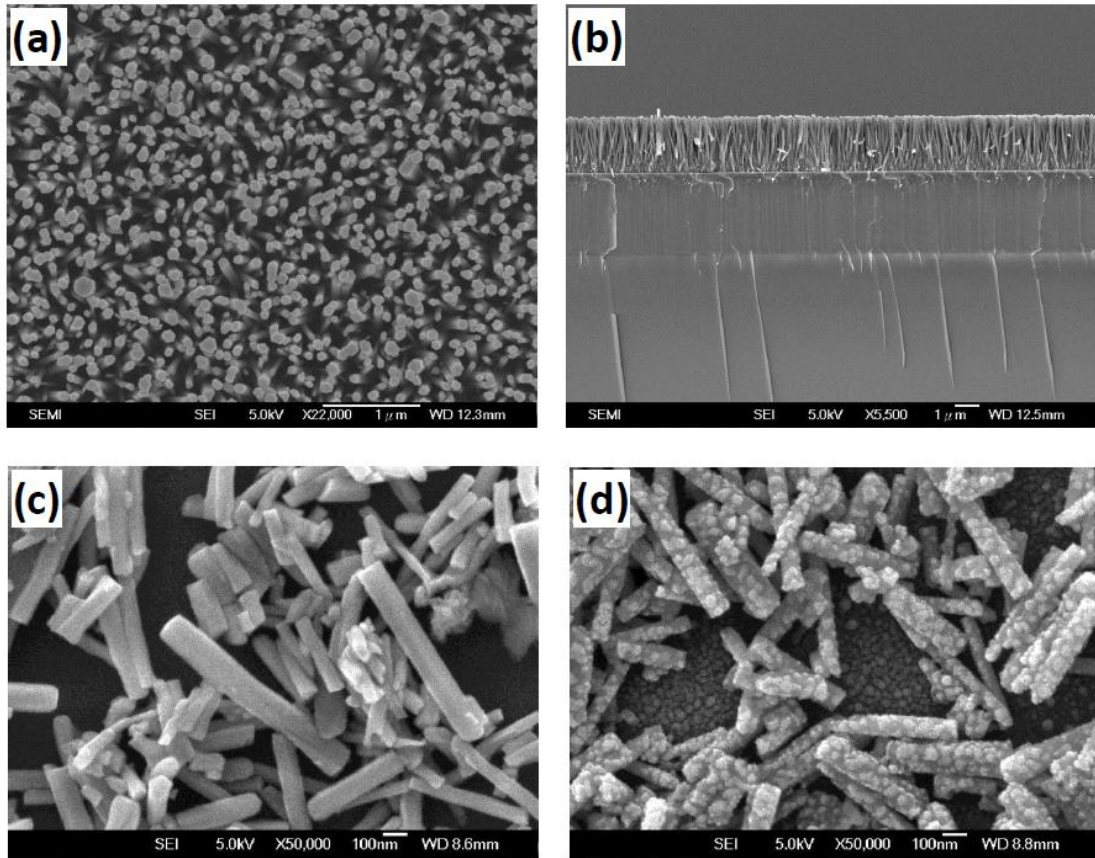


Fig. 7.1 (a) Top view and (b) side view of scanning electron microscope images of ZnO nanorods grown on sapphire substrate.

7.3 Results and Discussion

As shown in Fig. 7.2 (a), we can see that the PL peak position for the sample containing InGaN/GaN MQWs, ZnO NRs, and Pt NPs reveals a red-shift from 12 meV to 30 meV with the increasing concentration of target hydrogen gas from 100 to 3000 ppm. The peak located near 2.73 eV can be referred to the excitonic emission of InGaN/GaN MQWs.^{10,16} Additionally, we have further prepared two reference samples. The first one is denoted as R1, which contains MQWs and ZnO NRs but without Pt NPs. The second one is denoted as R2, which purely contains MQWs without ZnO NRs and Pt NPs. They were treated by the same detection process as the above description, and the obtained spectra are shown in Figs. 7.2 (b) and (c). The peak positions of PL spectra from these three samples are graphed as functions of the concentration of the target hydrogen gas as shown in Fig. 7.2 (d). Obviously, we can see that the sensitivity of R1 sample is lower than the sample with InGaN/GaN MQWs, ZnO NRs, and Pt NPs, and R2 sample reveals almost no sensitivity. This means that both ZnO NRs and Pt NPs play important roles in the sensing process.

The underlying mechanism of the detection may be preliminarily attributed to the REDOX reaction between the oxygen ions on ZnO NRs and the target hydrogen molecules. It is well accepted that the abilities of semiconductor gas sensors can be attributed to the chemisorptions of oxygen on the oxide surface and the subsequent

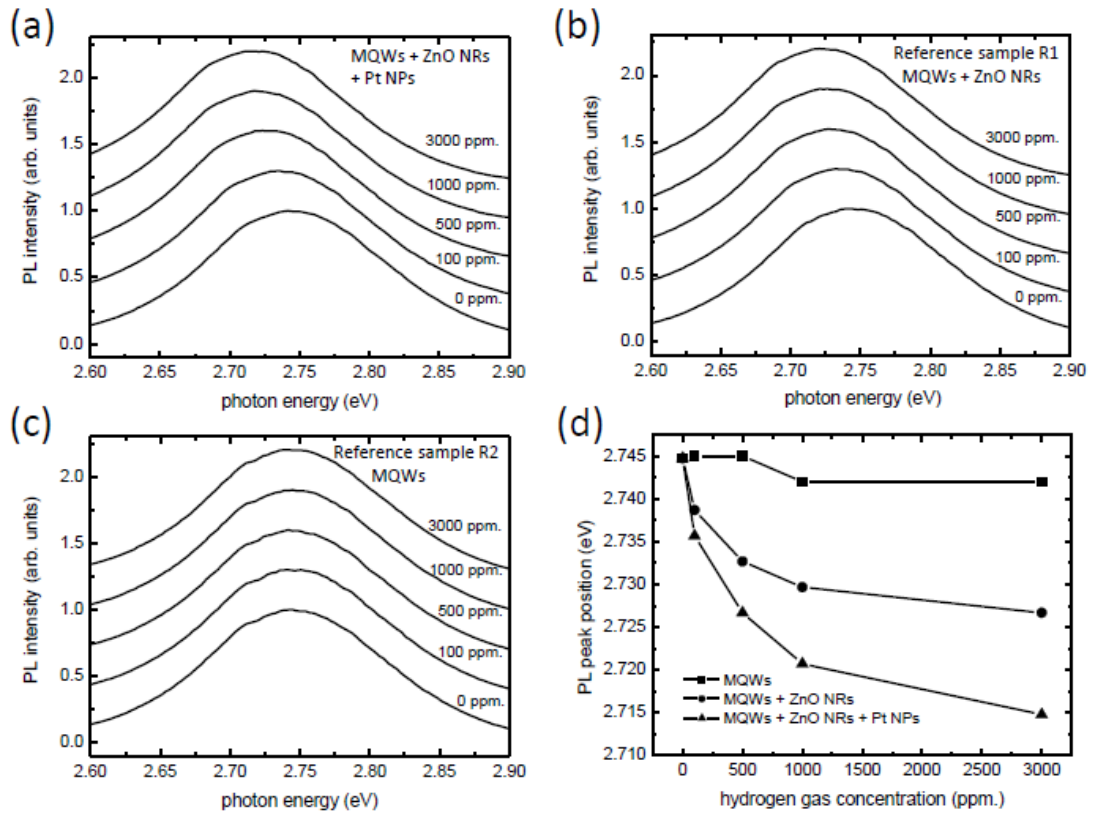


Fig. 7.2 (a) Photoluminescence spectra of InGaN/GaN multiple quantum wells with Pt-catalyzed ZnO nanorods, (b) uncatalyzed ZnO nanorods, and (c) without ZnO nanorods as under the increasing concentration of target hydrogen gas. (d) Peak positions of the spectra in (a), (b), and (c) as functions of the concentration of target hydrogen gas.

reaction between the adsorbed oxygen and the target gas.⁵ It has been reported that the stable oxygen ion states are O_2^- below 100 °C, O^- between 100 and 300 °C, and O^{2-} above 300 °C.¹³ The corresponding reactions on the surface area could be described as follows:



No matter what route the reaction goes, electrons are released due to the REDOX reaction, which will alter the charge state of the active zone on the MQWs. These electrons consequently change the electric field nearby and then tilt the energy band structure of the MQWs. Figures 7.3 (a) and (b) provide a clear picture to illustrate the influence on energy band structures of MQWs under different hydrogen concentrations. Before hydrogen gas injection, the energy band of MQWs is initially flat as shown in Fig. 7.3 (a). Once the hydrogen gas is injected, the REDOX reaction occurs on ZnO NRs of the device, such that the released electrons would create an external electric field and tilt the band structure of MQWs, as a result the recombination energy of electron-hole pairs is reduced due to QCSE, which causes a red-shift in PL spectra.^{18,19} Therefore, we could realize that ZnO NRs provide oxygen ions to react with the target gas, and they also provide a high surface to volume ratio

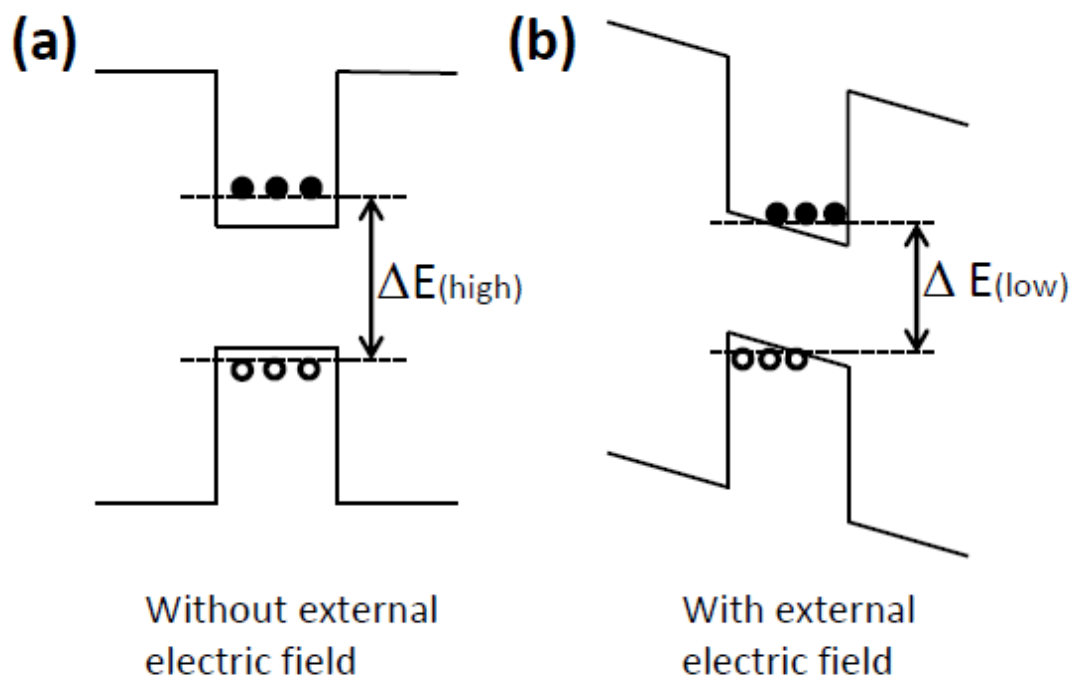
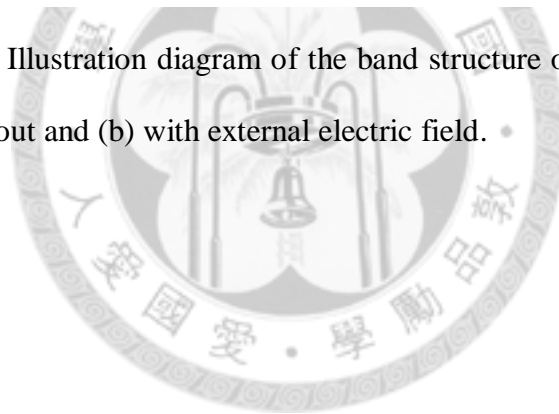


Fig. 7.3 Illustration diagram of the band structure of MQWs
 (a) without and (b) with external electric field.



to enhance the detection sensitivity. On the other hand, Pt NPs play the role of catalyst to accelerate the reaction rate, which have been widely used in hydrogen sensing.^{14,15} Thus the sensitivity of the sample with Pt NPs is higher than that without Pt NPs. The results shown in Fig. 7.2 therefore can be reasonably explained.

To further confirm the above interpretation, we have performed μ -Raman scattering measurements for all of the three samples under different concentrations of target hydrogen gas as shown in Figs. 7.4 (a), (b) and (c). The spectrum located near 732 cm^{-1} can be assigned to InGaN $A_1(\text{LO})$ mode.¹⁰ With ZnO NRs and Pt NPS, the Raman scattering spectra of MQWs in Fig. 7.4 (a) show a much more pronounced high-energy shift in the peak position with respect to the increase of the target gas concentration compared with the spectra shown in Figs. 7.4 (b) and (c). This intriguing behavior can be understood by the converse-piezoelectric effect, which means that an external electric field could induce a strain in a piezoelectric material.^{10,16} Here, the modification of the external electric field arises from the REDOX reaction between the oxygen ions on ZnO NRs and the target hydrogen gas as described above. Because nitride semiconductors are good piezoelectric materials, a change of electric field in the lattice can produce a strain and alter the lattice constant, which then leads to the change of the Raman scattering spectra. According to the PL spectra shown in Fig. 7.2 (a), the electric field in MQWs lattice is increased

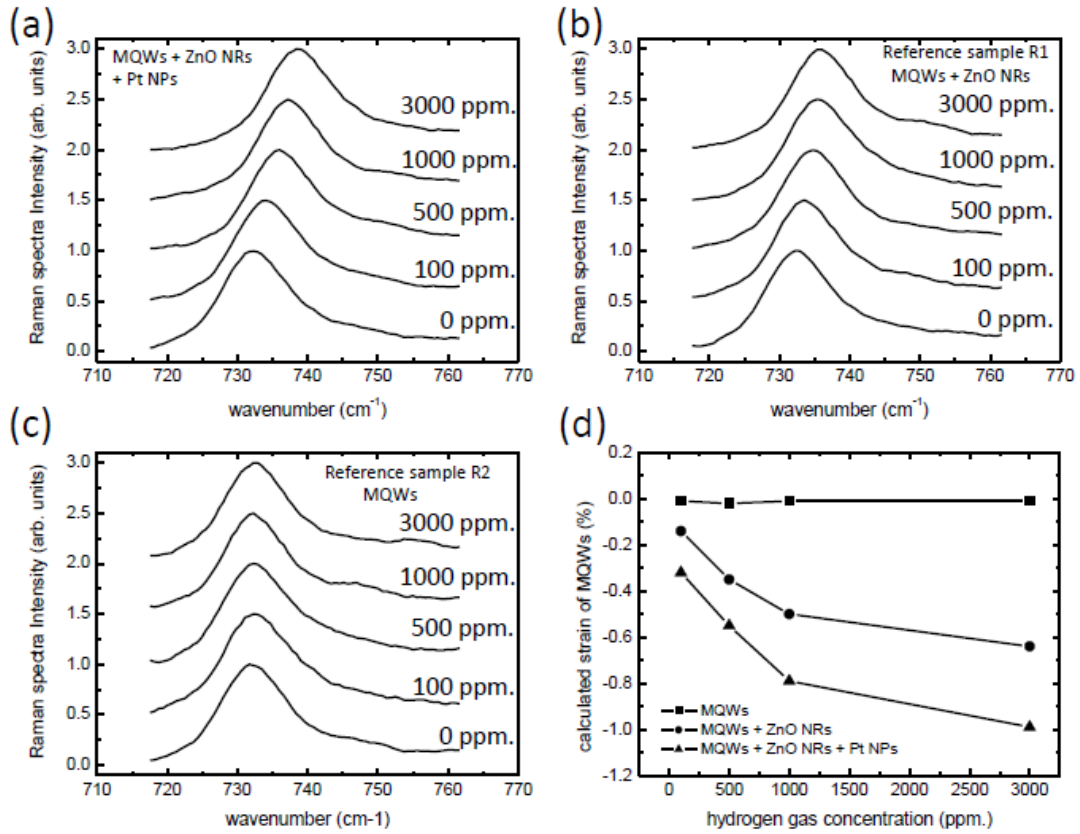


Fig. 7.4 (a) Raman scattering spectra of InGaN/GaN multiple quantum wells with Pt-catalyzed ZnO nanorods, (b) uncatalyzed ZnO nanorods, and (c) without ZnO nanorods as under the increasing concentration of target hydrogen gas. (d) Estimated lattice strain of InGaN/GaN multiple quantum wells as functions of the concentration of target hydrogen gas.

after REDOX reaction, and therefore a high-frequency shift of the LO phonon energy can be expected.^{10,16} This expectation is consistent with what has been observed as shown in Fig. 7.4 (a). On the other hand, the Raman scattering spectra of the reference samples as shown in Figs. 7.4 (b) and (c) exhibit that they are not so sensitive to the target gas as the sample with InGaN/GaN MQWs, ZnO NRs, and Pt NRs. Thus, this result lets us make the conclusion that ZnO NRs and Pt NPs are indeed important components in the enhanced detection ability.

Let us now examine the internal strain based on the Raman scattering measurements. The magnitude of the strain can be estimated by the high-energy shift of the $A_1(\text{LO})$ phonon mode according to the following equation:¹⁶

$$\varepsilon = \frac{\Delta\omega}{2\left(a - b\frac{C_{13}}{C_{33}}\right)}, \quad (7.4)$$

where a and b are phonon deformation potentials, and C_{13} and C_{33} are elastic constants, respectively. Figure 7.4 (d) shows the strain as a function of target gas concentration calculated from Eq. (7.4), where the deformation potentials a , b and the elastic constants C_{13} , C_{33} were estimated by the extrapolation of the data for GaN and InN.¹⁷ With ZnO NRs and Pt NPs, the strain of InGaN/GaN MQWs of the device increases more than those of the two reference samples as expected. We therefore can see that the shifts in both PL spectra and Raman scattering of the sensing device can

be well explained in a consistent way based on the piezoelectric alteration due to the REDOX reaction.

7.4 Conclusion

In conclusion, we have demonstrated that the optical properties of InGaN/GaN MQWs with ZnO NRs and Pt NPs can be used to detect hydrogen gas. The underlying mechanism is based on the highly sensitive nature of NRs and piezoelectric property of nitride semiconductors under different ambient environment. In addition, the Pt NPs play the role as catalyst, which can accelerate the REDOX reaction rate. Our working principle shown here can be readily extended to many other applications by using different chemistries. In view of the wide utilization of LEDs and laser diodes based on nitride semiconductors, the study carried out along our guideline shown here should be very useful for the creation of highly sensitive sensors using optical detection.

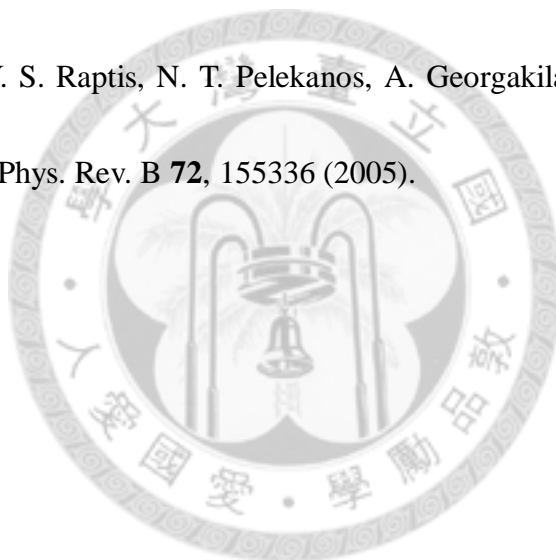
Reference

1. H. Y. Shih, Y. T. Chen, N. H. Huang, C. M. Wei, and Y. F. Chen, *J. Appl. Phys.* **109**, 103523 (2011).
2. C. Bayram, F. Hosseini Teherani, D. J. Rogers, and M. Razeghi, *Appl. Phys. Lett.* **93**, 081111 (2008).
3. C. Y. Huang, Y. J. Yang, J. Y. Chen, C. H. Wang, Y. F. Chen, L. S. Hong, C. S. Liu,

- and C. Y. Wu, Appl. Phys. Lett. **97**, 013503 (2010).
4. C. T. Chen, F. C. Hsu, S. W. Kuan, and Y. F. Chen, Solar Energy Materials and Solar Cells **95**, 740 (2011).
 5. S. C. Hung, C. W. Chen, C. Y. Shieh, G. C. Chi, R. Fan, and S. J. Pearton, Appl. Phys. Lett. **98**, 223504 (2011).
 6. O. Lupan, V. V. Ursaki, G. Chai, L. Chow, G. A. Emelchenko, I. M. Tiginyanu, A. N. Gruzintsev, and A. N. Redkin, Sensors and Actuators B **144**, 56 (2010).
 7. Q. Wan, Q. H. Li, Y. J. Chen, T. H. Wang, X. L. He, J. P. Li, and C. L. Lin, Appl. Phys. Lett. **84**, 3654 (2004).
 8. J. X. Wang, X. W. Sun, Y. Yang, H. Huang, Y. C. Lee, O. K. Tan, and L. Vayssieres, Nanotechnology **17**, 4995 (2006).
 9. R. Dahal, B. Pantha, J. Li, J. Y. Lin, and H. X. Jiang, Appl. Phys. Lett. **94**, 063505 (2009).
 10. T. Y. Lin, Appl. Phys. Lett. **82**, 880 (2003).
 11. C. F. Huang, C. Y. Chen, C. F. Lu, and C. C. Yang, Appl. Phys. Lett. **91**, 051121 (2007).
 12. M. Guo, P. Diao, and S. M. Cai, Journal of Solid State Chemistry **178**, 1864 (2005).
 13. M. Takata, D. Tsubone, and H. Yanagida, Journal of the American Ceramic

Society **59**, 4 (1976).

14. M. K. Kumar and S. Ramaprabhu, Journal of Physical Chemistry B **110**, 11291 (2006).
15. G. Papoian, J. K. Norskov, and R. Hoffmann, Journal of the American Chemical Society **122**, 4129 (2000).
16. H. Y. Shih, Y. T. Chen, C. M. Wei, M. H. Chan, J. K. Lian, Y. F. Chen, and T. Y. Lin, J. Phys. Chem. C **115**, 14664 (2011).
17. A. G. Kontos, Y. S. Raptis, N. T. Pelekanos, A. Georgakilas, E. Bellet-Amalric, and D. Jalabert, Phys. Rev. B **72**, 155336 (2005).





Chapter 8

Summary of this Dissertation

In summary, we have demonstrated five works involved semiconductor nanostructures, especially ZnO nanorods (NRs) and InGaN/GaN multiple quantum wells (MQWs). In chapters 1 and 2, we have firstly introduced the basic physical concepts of semiconductors and necessary techniques adopted in our works. Next, we have thoroughly described the main portions of our works.

In chapter 3, dual beams excitation of PL and PC have been used to investigate the influence of defects on the optical properties of ZnO nanostructures. It is found that the second below-gap excitation can significantly quench the NBE emission and photocurrent. By varying the photon energy of below-gap excitation, the important information for the understanding of defect characteristics can be revealed, which is difficult to achieve for most available techniques. In chapter 4, we have investigated the influences of an external stress on the optical properties of InGaN/GaN MQDs with wurtzite (C_6^v) symmetry. The PL spectrum of MQDs reveals a red-shift as they are bent by an external force. This can be explained by the QCSE due to the piezoelectric field caused by the strain. In addition, the $A_1(\text{LO})$ mode of Raman scattering spectrum is broadened and has a low-energy shift in the bent NRs. We point out that there exists a compressive strain on the concave side and a tensile strain on

the convex side, and the convex part of the MQW-NRs would suffer more deformation than the concave part. Quite interestingly, we have found that the amount of the red-shift in PL and Raman scattering spectra depends on the bending orientation. When the NRs are bent toward a -axis, the shift amounts of PL and Raman scattering spectra are more than those toward m -axis. This difference can be well interpreted by the nature of hexagonal lattice having a sixfold symmetry. In chapter 5, we have demonstrated a novel LED based on the composite consisting of ZnO NRs and InGaN/GaN MQWs. The newly designed LED has the capability to emit dual beam radiations. Quite interestingly, the relative intensity between the dual emissions can be manipulated by a polarizer. The underlying mechanism can be well interpreted in terms of the anisotropic optical properties arising from the geometric structures of the constituent nanoscale materials. In chapters 6 and 7, we have demonstrated that the optical properties of InGaN/GaN MQWs with functionalized ZnO nanorods can be used to detect glucose and hydrogen molecules, respectively. The underlying mechanism is based on the highly sensitive nature of nanorods and piezoelectric property of nitride semiconductors under different ambient environment. Our working principle shown here can be readily extended by employing many other molecules for surface functionalization and by using different chemistries

In view of the wide utilization of optoelectronic devices based on ZnO and

nitride semiconductors, the study carried out along our guideline shown in this dissertation should be very useful for the creation of advanced technologies which are able to save energy, protect the environment, and bring more conveniences for our daily life.

